

**Optically detected magnetic resonance
of Arsenic-antisite-related defects in semi-insulating bulk
and low temperature MBE-grown GaAs**

Vom Fachbereich Physik der Universität Paderborn
zur Erlangung des akademischen Grades eines
Doktors der Naturwissenschaften
(Dr.rer.nat.)
genehmigte Dissertation

von

Igor Tkach

1.Gutachter:
2.Gutachter:

Prof. Dr. J.-M.Spaeth
Prof. Dr. H.Overhof

Tag der Einreichung:
Tag der mündlichen Prüfung:

10. 05. 2002.
14. 06. 2002.

Table of contents

	Introduction	1
1	Theoretical and experimental fundamentals	5
1.1	Magneto-optical techniques.....	5
1.1.1	Magnetic Circular Dichroism of the optical Absorption (MCDA).....	5
1.1.1.1	MCDA-detected Electron Paramagnetic Resonance (MCDA-EPR) and Electron Nuclear Double Resonance (MCDA-ENDOR)	10
1.2	The spin–Hamiltonian for the analysis of EPR and ENDOR spectra	13
1.2.1	EPR spectra	13
1.2.2	ENDOR spectra.....	17
2	Experimental aspects of high-field/high-frequency MCDA-EPE/ENDOR: new developments	21
2.1	Introduction	21
2.2	W-band (95GHz) MCDA-EPR spectrometer.....	23
2.3	W-band EPR/ENDOR multimode Fabry-Pérot cavity.....	26
2.4	Tilt corrector	34
2.5	W-band TE ₀₁₁ -mode cylindrical cavity	36
3	The EL2 defect in semi-insulating GaAs : W-band MCDA-EPR/ENDOR investigation of the microscopic structure.....	41
3.1	Introduction	41
3.2	Fingerprints of the EL2 defect in GaAs.....	44

3.2.1	Optical absorption.....	45
3.2.2	MCDA	46
3.2.3	MCDA-EPR.....	47
3.3	Advantage of high-field EPR and ENDOR of the EL2 defect	50
3.4	W-band MCDA-ENDOR of the EL2 defect in GaAs	56
3.4.1	The first neighbour shell of the As-antisite	56
3.4.2	Tilt of the crystal and its correction.....	67
3.4.3	As _{Ga} -As _i pair model: high field revision MCDA-ENDOR	72
3.4.4	The higher As shell of the EL2 defect.....	74
3.5	MCDA-EPR: line width analysis of the EL2 defect.....	81
3.6	Conclusions.....	86
4	Arsenic-antisite-related defects in high resistive LT-MBE-GaAs and their relation to the EL2	89
4.1	Introduction.....	89
4.2	Sample preparation	92
4.2.1	Growth and annealing.....	92
4.2.2	Epitaxial lift-off technique.....	93
4.2.3	Overview over the samples.....	95
4.3	MCDA-EPR of MBE-grown LT-GaAs.....	96
4.4	MCDA and MCDA “tagged” by EPR spectra.....	105
4.5	Bleaching efficiency	111
4.6	Conclusions.....	115
	Summary.....	117
	References	121

Introduction

Gallium arsenide (GaAs) is an important material for modern electronics. The high mobility of charge carriers and the direct band gap enable its important high frequency applications where other semiconductors can not be used.

It is well known that most properties of semiconductors important for applications are influenced by the point defects contained within the crystalline lattice. These defects can be created artificially by doping or ion implantation, and this is used when the material is deliberately treated to make it either n-or p-conducting or semi-insulating. However, there is a kind of the defects which arises in the material naturally during its growth not involving impurities. They are referred to as native (intrinsic) defects to distinguish them from dopant atoms. These defects are often electrically and optically active. They play also an important role in semiconductor technology.

In GaAs it has been known for a long time that within a certain stoichiometry range as-grown GaAs becomes semi-insulating due to the formation of an intrinsic defect during crystal growth. The semi-insulating GaAs is of great technological importance because it is used as a substrate material for high-speed digital and microwave monolithic integrated circuits. The semi-insulating property of undoped GaAs results from the pinning of the Fermi level by a midgap donor level. The defect responsible for that is the famous EL2 defect, which plays the role of a double donor compensating unwanted shallow acceptors. The name EL2, electron level number 2, was given to a deep trap having characteristic electron emission parameters (activation energy and emission cross section) determined by deep level transient spectroscopy (DLTS) by Martin and collaborators in 1977 [Martin 1977].

For almost two decades the structure model of the EL2 defect has been controversially discussed. Neither the isolated As_{Ga} with T_d symmetry, nor the $\text{As}_{\text{Ga}}\text{-As}_i$ pair model nor any other As_{Ga} -related defect model could be unambiguously established. Most experimental information on the structure of the EL2 defect comes from electron paramagnetic resonance (EPR) and Electron Nuclear Double Resonance (ENDOR) of the

defect in the paramagnetic charge state, which is the singly ionised state $EL2^+$. But the analysis of previously MCDA-detected ENDOR (MCDA-ENDOR) and MCDA-detected EPR (MCDA-EPR) spectra measured at 24 GHz [Meyer 1988] was not unambiguous. The spectra were measured in K-band (~ 24 GHz) at “low magnetic fields” compared to the hyperfine interactions and were thus complicated by higher order effects such as pseudo-dipolar nuclear couplings and forbidden transitions. The only way to get the clearer and more reliable information about the symmetry of the defect would be high field ENDOR. At high fields, where the electron Zeeman interaction is much stronger compared to the hyperfine and superhyperfine interactions, higher order effects in the ENDOR and EPR spectra should be less apparent.

To make the high field EPR and ENDOR investigation possible a new equipment needed to be developed for such measurements. A microwave cavity for MCDA-EPR and ENDOR operating at high frequencies had to be constructed. This task was not trivial, therefore several different designs of high frequency resonators have been built and tested. In this thesis the designs of successfully working cavities (Fabry-Perot and cylindrical) are presented in detail. Also technical aspects of the high-field/high-frequency MCDA-EPR/ENDOR are discussed.

The first high-frequency MCDA-EPR and ENDOR measurements of the $EL2$ justified the expectations from high field spectroscopy. W-band MCDA-EPR and particularly MCDA-ENDOR spectra are much simpler and clearer with respect to their analysis. In this work the results of such measurements and their analysis are presented and discussed. An alternative model of the $EL2$ defect which is consistent with the new experiment and older experiments and a theoretical analysis [Overhof 2002] is suggested.

Recently, new GaAs material appeared with particular technological interest. It is GaAs grown by molecular beam epitaxy (MBE) at low ($\sim 200^\circ\text{C}$) substrate temperature (LT-GaAs). This material exhibits unique properties opening the frontiers of the new applications of GaAs. Because of its high resistivity and extremely short life times of photo-generated carriers (and many other more or less useful properties) GaAs grown in such a way can be used as main material in ultrafast photoswitchers, generators, antennas, and other devices working in THz region. Those properties of the material may be due to its large non-stoichiometry. Native defects appear in LT-GaAs in very large

concentrations (up to 10^{20} cm^{-3}). These defects are mainly As-antisite related defects, which are believed to be EL2-like defects, only modified by the lattice strain. The last chapter of the thesis deals with those defects in as-grown and annealed LT-GaAs. The main goal of the work presented in that chapter is to specify the relation of the As-antisite-related defects in LT-GaAs to that “classical” EL2 defect which appears in semi-insulating as-grown LEC GaAs. Therefore, a magneto-optical investigation with the MCDA and MCDA-EPR technique was performed on as-grown and annealed LT-GaAs. The results are presented and discussed.

$I_r = I_0 \exp(-\alpha_r d)$ intensity passed through the sample for right polarized light
(I_0 - intensity of light incident on the sample)

$I_l = I_0 \exp(-\alpha_l d)$ intensity passed through the sample for left polarized light
(I_0 - intensity of light incident on the sample)

The modulation of the light polarization is performed with an optical phase modulator consisting of a linear polarizer and an acousto-optical modulator. The acousto-optical modulator is an oscillating quartz slab acting as an oscillating $\lambda/4$ plate. The angle between its axes and that of the linear polariser is 45° . In such a way the polarization of the light is modulated between right and left-circular polarization. The quotient of the zeroth and first Fourier coefficients of the detected time-dependent signal is proportional to the hyperbolic tangent of the MCDA [Jasperson and Schnatterly 1969, Baldacchini and Mollenauer 1972].

The total MCDA consists of two parts, a diamagnetic and a paramagnetic one:

$$MCDA(B, T) = MCDA_d(B) + MCDA_p(B, T) \quad (1.3)$$

The diamagnetic part $MCDA_d$ is temperature independent and proportional to the external magnetic field, while the paramagnetic part $MCDA_p$ depends on the temperature as well as on the external magnetic field. The diamagnetic part is caused by unresolved Zeeman splittings of the excited states [Mollenauer and Pan 1972].

The paramagnetic part of MCDA is proportional to a spin polarization (P) of the ground state of the defect. For a paramagnetic system with $S=1/2$ this polarization is determined

by $P = \left(\frac{n_- - n_+}{n_- + n_+} \right)$, with n_- and n_+ being the occupations of the *Kramers* doublet levels.

In general the ground state spin polarization (P) in thermal equilibrium is given by the *Brillouin* function and can be determined as :

$$P = \langle S_z \rangle = SB_s(\mu) \quad (1.4)$$

with

$$B_s(\mu) = \frac{1}{S} \left[\left(S + \frac{1}{2} \right) \coth \left[\left(S + \frac{1}{2} \right) \mu \right] - \frac{1}{2} \coth \left(\frac{\mu}{2} \right) \right] \quad (1.5)$$

$$\mu = \frac{g\mu_B B}{kT}, \quad (1.6)$$

where S -spin, g – g-factor of the center, μ_B – Bohr Magneton and k - Boltzmann's constant.

For a system with $S=1/2$ the ground state spin polarization is:

$$P = \tanh \left(\frac{\Delta E}{2kT} \right) \quad (1.7)$$

Here ΔE is the energy difference of the Zeeman split paramagnetic levels.

In figure 1.1 the method of MCDA is illustrated in detail for the example of a simple $s \rightarrow p$ transition of the “alkali atom model”. In a magnetic field the ground state Kramers doublet is split into Zeeman levels $m_S = \pm 1/2$, the excited p states are split by the spin-orbit interaction into $j = 1/2$ and $j=3/2$ states with the magnetic substates m_j .

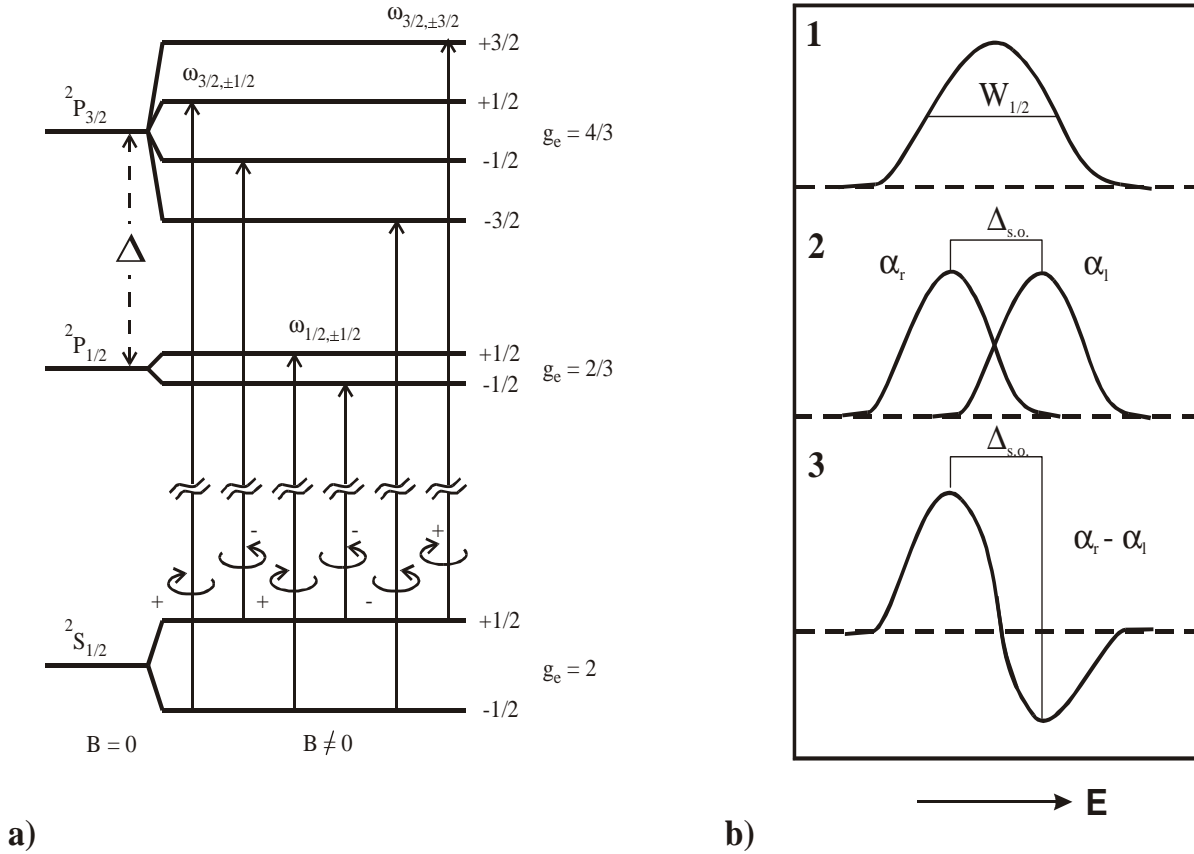


Fig. 1.1. (a) Level scheme and circularly polarized optical absorption transitions for a simple alkali atom model after Lüty and Mort [Lüty and Mort 1964]; (b) representation of the optical absorption and MCDA spectra resulting from such transitions: (1) absorption with unpolarized light; (2) absorption with right and left polarized light; (3) MCDA.

Six atomic transitions with $\Delta m_j = \pm 1$ are possible. The transition probabilities ω_{j,m_j} of the transitions from the two Zeeman-split levels of the ground state to a certain j -multiplet of the excited states are equal for $\pm m_j$ (time reversal symmetry). The paramagnetic part of the MCDA is proportional to the difference of the rates of the $\Delta m_j = \pm 1$ transitions to a certain j -multiplet. The rates of the transitions are products of the occupation numbers and corresponding transition probabilities. It can be shown that the paramagnetic MCDA is proportional to a difference of occupations of the Kramer doublet states (MCDA_p \propto $[\omega_{1/2, \pm 1/2} + \omega_{3/2, \pm 1/2} - \omega_{3/2, \pm 3/2}] \times [n_{-1/2} - n_{+1/2}]$) [Lüty and Mort 1964].

The dichroism $MCDA$ is the difference of two absorption bands (α_r and α_l). The peaks of the bands are separated by the energy of the spin-orbit splitting $\Delta_{s.o.}$ [Henry and Slichter 1968], and can be approximated by a derivative

$$MCDA(\omega) \approx \frac{Ed}{2\hbar c} \frac{dk(E)}{dE} \Delta E \quad (1.8)$$

with E being the photon energy ($E = \hbar\omega$) and $k(E)$ being the energy dependent absorption coefficient.

With the assumption that the optical band shape is a *Gaussian*, one obtains for the extrema of $MCDA(\omega)$ the following relation:

$$MCDA_{extr} = \pm \sqrt{\frac{\ln(2)}{2e}} \frac{2\alpha_0 d}{W_{1/2}} \left[\frac{\mu_B B_0 (g_2 + 5g_3)}{3} - \frac{\Delta_{s.o.}}{3} \tanh\left(\frac{g_e \mu_B B_0}{2kT}\right) \right] \quad (1.9)$$

g_2 and g_3 are g factors of the excited state, α_0 is the absorption coefficient in the peak of the band, $W_{1/2}$ its half width, $\Delta_{s.o.}$ is the spin-orbit splitting of the excited states. The first term in (1.9) is the diamagnetic part, the second term the paramagnetic part of the MCDA. For $\Delta_{s.o.} \gg W_{1/2}$ there are two separate bands for MCDA, one with positive, the other with negative sign.

The MCDA is normally measured at high magnetic fields (1 - 3 Tesla) and at low temperatures (1.5 - 4.2 K), where the spin polarization of the ground state is large enough. The expressions (1.8) and (1.9) hold in the so called “right-shift approximation” ([Henry 1965]), i.e. the phonon influence is neglected except for Gaussian line shape.

1.1.2 MCDA detected Electron Paramagnetic Resonance (MCDA-EPR) and Electron-Nuclear Double Resonance (MCDA-ENDOR)

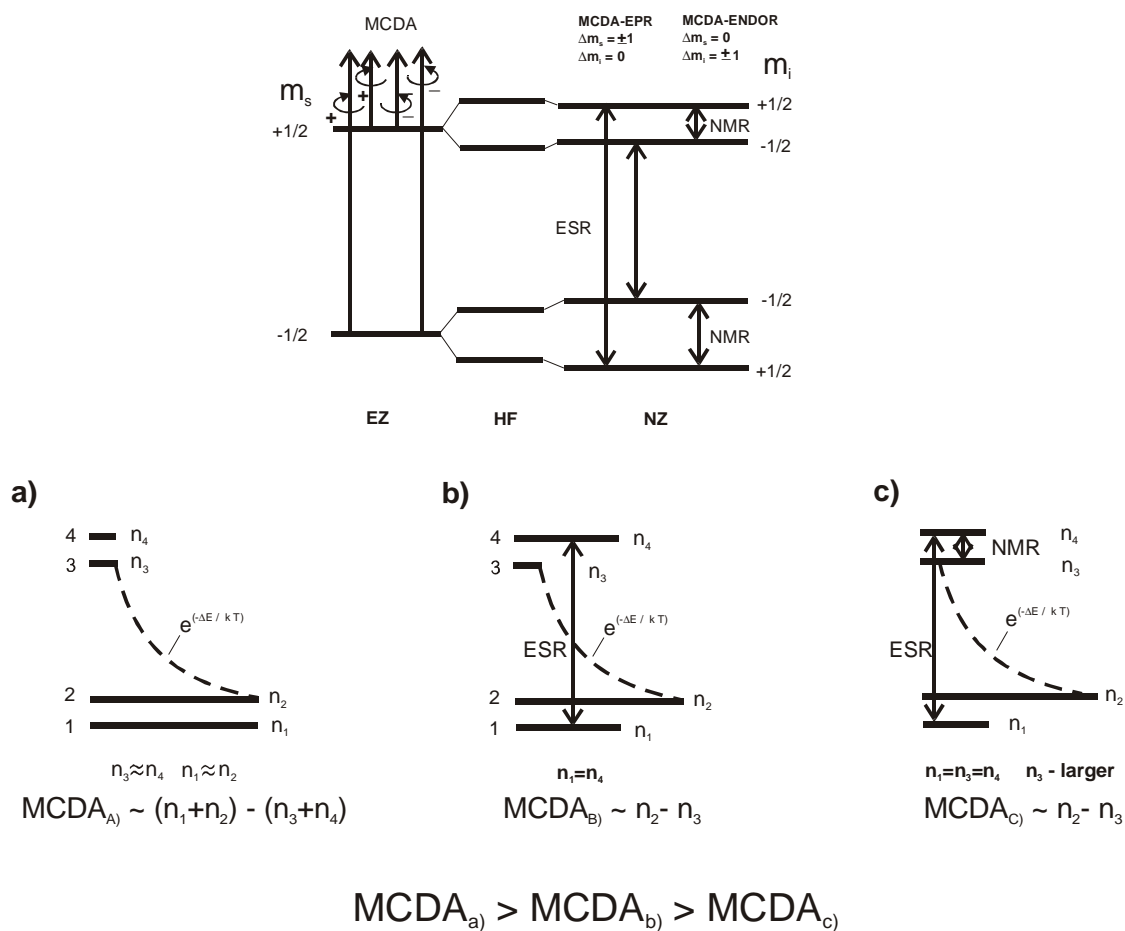


Fig.1.2 Schematic diagram explaining the MCDA-EPR and MCDA-ENDOR effects of a simple system having $S=1/2$ and $I=1/2$. The relative occupations if the magnetic levels are symbolised by the length of the horizontal sticks; (a) stationary level occupations in thermodynamic equilibrium, (b) stationary population during a saturating EPR transition and (c) stationary population during a simultaneously induced saturating EPR and NMR transitions.

It was mentioned above that paramagnetic part of the MCDA is proportional to the ground state spin polarization. In thermodynamic equilibrium the spin polarization is field and temperature dependent and is determined by a *Brillouin* function. There is a way to change this polarization by inducing magnetic dipole transitions between the paramagnetic levels by applying a resonant microwave field with respect to the Zeeman splitting of the ground state. Saturating microwave transitions reduce the spin-polarisation, thus they reduce the MCDA. This reduction is monitored to detect EPR (see fig.1.2).

In the experiment such a change of the MCDA is measured at a fixed optical wavelength and a fixed microwave field upon sweeping the external magnetic field. This technique is only one of the possibilities to detect the Electron Paramagnetic Resonance optically. In this case it is called MCDA detected EPR (MCDA-EPR).

In addition to the EPR transitions the ground state spin polarization can be affected by a resonant radio frequency (RF) field applied simultaneously with the microwave. This is monitored as an additional decrease of the MCDA and is called MCDA-Electron Nuclear Double Resonance (MCDA-ENDOR) [Spaeth 1992].

EPR and NMR transitions are indicated in figure 1.2 where a simple spin system consisting of an electron spin with $S = 1/2$ and of the nuclear spin with $I = 1/2$ is illustrated schematically.

Figure 1.2 shows also the stationary occupation of the levels of this system before (a) and occupations during a saturating EPR and NMR transition (b,c). In the case (a) all the levels are occupied according to the Boltzmann distribution. Applying the microwave field one can theoretically reach a condition when the levels 1 and 4 have the same occupations, while the levels 2 and 3 are in thermal equilibrium (case b). The paramagnetic MCDA is proportional to $(n_1 + n_2 - n_3 - n_4)$. The EPR transition diminishes the spin polarization because the occupation of level 4 is increased at the expense of level 1. An additional saturating NMR transition between the levels 3 and 4 (case c) equalizes their occupations, therefore the occupations of the three levels 1, 3, and 4 are the same. The occupation of level 1 is further decreased and the sum of the occupations of

levels 3 and 4 is increased. This leads to a further decrease of the spin polarization of the ground state, which is measured as the MCDA-ENDOR signal [Spaeth 1992].

A very large advantage of the MCDA technique of the EPR/ENDOR detection is that its sensitivity can be increased considerably in comparison with conventional detection. For example, the signal-to-noise ratio of the MCDA-EPR spectra of the EL2 defect in semi-insulating GaAs is two orders of magnitude higher as that of conventional EPR. One of the reasons of such a gain is increased energy of the quanta under detection.

Furthermore, it is very difficult to correlate unambiguously the optical absorption and the EPR spectra of a defect, if both spectra are measured separately. This problem is severe in solid state physics where the presence of several different centers is a usual case. With the MCDA a direct correlation of the optical and paramagnetic properties of the defect under investigation is possible. In other words, the coupling of the MCDA and EPR allows the assignment of optical transitions to a specific center. Taking into account that the ground state polarization is the same for all optical transitions of a certain defect one can separate superimposed MCDA bands of different point defects present in a solid measuring a kind of excitation spectrum of the MCDA-EPR/ENDOR lines. Thus, one can set the EPR(ENDOR) resonance conditions to a particular EPR(ENDOR) line, vary the optical wavelength and monitor the EPR(ENDOR) signal as a microwave-induced (radio frequency-induced) change of the MCDA. By such a procedure one gets only that part from the total MCDA of a sample which belongs to the particular defect or defect orientation, if the EPR spectra are anisotropic. The signal detected in this way is called MCDA “tagged by EPR(ENDOR)”.

It is always important to know the spin state (and connected with it the charge state) of the defect in solids. One can derive the information about it from the EPR if fine structure or crystal field splitting are large enough to be resolved or from the ENDOR spectrum if its detection is possible. But in many cases the mentioned methods are not realizable. The MCDA technique can be used as an alternative method. Remembering that paramagnetic MCDA contains information on the spin state S of the defect, that the diamagnetic MCDA is linear in B one can separate the $MCDA_p$ from the total MCDA. One needs to measure the total MCDA for several magnetic fields and temperatures and form the following ratio:

$$R_{\text{exp}} = \frac{MCDA_p(B_1, T_1) - MCDA_p(B_1, T_2)}{MCDA_p(B_2, T_1) - MCDA_p(B_2, T_2)} \quad (1.10)$$

In (1.10) the diamagnetic term $MCDA_d$ is canceled out.

As a next step the experimental value R_{exp} has to be compared with the calculated one R_{theor} (see (1.11) ratio below) varying S .

$$R_{\text{theor}} = \frac{B_S(S, B_1 / T_1) - B_S(S, B_1 / T_2)}{B_S(S, B_2 / T_1) - B_S(S, B_2 / T_2)} \quad (1.11)$$

Both values R_{exp} and R_{theor} must be equal for the correct value of effective spin S [Görger 1988].

1.2 The spin-Hamiltonian for the analysis of EPR and ENDOR spectra

1.2.1 EPR Spectra

In the previous sections the physical principles of the MCDA-EPR/ENDOR technique have been described without the explanation of the nature of the interactions involved in the energy level splittings of the ground state of the paramagnetic defect. Only the Zeeman splitting of the Kramers doublet in a static magnetic field and the result of the microwave influence on the level occupations were considered for simplicity. However, in order to understand how to obtain the structural information from the EPR/ENDOR spectra of a defect, as for example its local symmetry, one needs to know the origin of the various microscopic interactions. The goal of this section is to review these terms which are relevant for the defects investigated in this work.

For the description of the EPR spectra the spin Hamiltonian is used in order to calculate the energy levels of the spin system and their EPR transitions. The spin-Hamiltonian (H) is the quantum mechanical operator related to the different eigenstates and eigenvalues of a spin system, i.e. a system with an effective spin different from zero. A typical example

of such a spin system is a point defect in a semiconductor crystal which causes the de-pairing of the electron spins. Such a spin-Hamiltonian can be determined as [Abragam and Bleaney 1986, Stevens 1952]:

$$H_{EPR} = H_{EZ} + H_{SHF} + H_Q + H_{FS} \quad (1.12)$$

where

$H_{EZ} = \mu_B \vec{B}_0 \tilde{g}_e \vec{S}$ is the electron Zeeman interaction, the interaction between the electron spin \vec{S} and the magnetic field \vec{B}_0 ;

$H_{SHF} = \sum_i \vec{I}_i \tilde{A}_i \vec{S}$ the superhyperfine (SHF) term describes the magnetic interaction of the electron spin \vec{S} with the nuclear spin \vec{I} of a neighbour nucleus. This term also includes the interaction with a central nucleus (hyperfine (HF) interaction);

$H_Q = \sum_i \vec{I}_i \tilde{Q}_i \vec{I}_i$ The quadrupole interaction (Q) takes into account the interaction of the quadrupole moment with an electrical field gradient at the site of the nucleus in the crystal;

$H_{FS} = \sum_{k=2}^{2S} \sum_{n=-k}^k B_k^n O_k^n(\vec{S})$ The fine structure interaction (FS) describes the spin-spin interaction for a spin system with $S > 1/2$

The symbols signify:

\tilde{g}_e	g_e -tensor
\tilde{A}_i	superhyperfine tensor of the nucleus i
\tilde{Q}_i	quadrupole tensor of the nucleus i
\vec{S}	electron spin operator
\vec{I}_i	nuclear spin operator of nucleus i
B_k^n	spin operator coefficient (Stevens parameter)

$O_k^n(\vec{S})$ spin operator (Stevens operator)

The superhyperfine interaction tensor \tilde{A}_i (second term of the spin-Hamiltonian (eqn. 1.12) is represented by a 3x3 matrix and in its diagonal form can be written as a sum of two contributions :

$$\tilde{A} = a \tilde{1} + \tilde{B} \quad (1.13)$$

where a is an isotropic and \tilde{B} is the traceless anisotropic part of the tensor. $\tilde{1}$ is the identity matrix.

The isotropic constant a , the so-called Fermi contact interaction, is proportional to the unpaired spin density at the nuclear site $\left(|\psi(0)|^2 \right)$ in a one-particle approximation [Slichter 1980]:

$$a = \frac{2}{3} \mu_0 g_e \mu_B g_I \mu_n |\psi(0)|^2 \quad (1.14)$$

g_I nuclear g-factor
 μ_n nuclear magneton
 g_e electronic g-factor

$\psi(\vec{r})$ is the wave function of the unpaired electron of the defect in one particle approximation.

The elements of the anisotropic part \tilde{B} can be written as [Slichter 1980]:

$$B_{ik} = \frac{1}{4\pi} \mu_0 g_e \mu_B g_I \mu_n \int \left(\frac{3x_i x_k}{r^5} - \frac{\delta_{ik}}{r^3} \right) |\psi(\vec{r})|^2 dV \quad (1.15)$$

In the principal axis system the traceless anisotropic shf tensor can be represented by two independent interaction parameters:

$$b = \frac{B_{zz}}{2},$$

$$b' = \frac{B_{xx} - B_{yy}}{2} \quad (1.16)$$

If $b'=0$, the symmetry is axial with respect to the Z-axis. $b' \neq 0$ gives the deviation from the axial symmetry. The anisotropic hyperfine constants, as can be seen in eqn. 1.15, describe the average over $(1/r^3)$ calculated with the defect wavefunction and show how this wavefunction decreases radially.

For the analysis of the EPR spectra the spin Hamiltonian is diagonalised, and the energy differences between the levels for the EPR transition condition $\Delta m_S = \pm 1$ and $\Delta m_I = 0$ are determined. In an EPR measurement the microwave frequency is fixed, that is the energy difference for the EPR transitions is fixed. The EPR spectrum is measured as a function of the variable magnetic field. The resonance magnetic fields must be determined using numerical procedures [Belford 1973; McGregor 1975].

In most cases, the hf interactions with the neighbour nuclei (shf) can be neglected in the diagonalisation of the spin Hamiltonian. These terms enter only in the calculation of the width of the EPR lines. A hf interaction of the central nucleus, if present, must be considered in the diagonalisation. The hf interaction is often too large to be dealt within the frame of an effective spin approximation in first order. This is particularly true for the As antisite defects in GaAs. The quadrupole term (H_Q) can be neglected for the description of EPR spectra, since it has only an indirect influence on the EPR transition energies. It can be responsible for the so-called “forbidden” EPR transitions, in which both the electron spin and the nuclear spin are flipped simultaneously (see [Koschnick and Spaeth 1999]).

1.2.2 ENDOR spectra

ENDOR measurements enable the determination of the interactions between the neighbour nuclei and the electron spin of the defect, which are usually not resolved in the inhomogeneously broadened EPR lines. To analyse the ENDOR spectrum of the i -th neighbour nucleus the following Hamiltonian is needed:

$$H_{ENDOR} = H_{NZ} + H_{SHF} + H_Q \quad (1.17)$$

where:

$$H_{NZ} = -\mu_n g_I \vec{B}_0 \cdot \vec{I} \quad \text{nuclear Zeeman interaction}$$

$$H_{SHF} = \vec{I} \tilde{A} \vec{S}_{eff} \quad \text{superhyperfine (SHF) interaction}$$

$$H_Q = \vec{I} \tilde{Q} \vec{I} \quad \text{quadrupole interaction}$$

In comparison to H_{EPR} , the nuclear Zeeman term (H_{NZ}) must be taken into account describing the interaction between the nuclear spin and the external magnetic field. \vec{S}_{eff} is the effective spin. The effective spin approximation is used in which the spin operator is replaced by the effective spin. The effective spin is the expectation value of the electron spin calculated with the eigenstates of H_{EPR} without the shf and quadrupole interactions. Therefore, in H_{ENDOR} neither the fine structure term nor the electron Zeeman term must be taken into account. Besides the decoupling of the electron spin operator and the nuclear spin operators, a further advantage of the effective spin approximation is that all nuclear spins can be treated separately. With this, the dimension of the Hamiltonian is reduced considerably. It corresponds to the perturbation calculation with degeneracy of first order. H_{ENDOR} describes the considered system adequately as long as significant change of the quantisation of the electron spin does not occur by a large interaction with the central nucleus or neighbour nuclei. In that case, the spin Hamiltonian (H_{ENDOR}) must be diagonalised, whereby the sum is formed only over the nuclei with large interactions. From this diagonalisation the effective spin can be calculated with which the neighbour shells with smaller shf interactions can then be analysed.

For nuclei with $I > \frac{1}{2}$ one must also consider the quadrupole term, Q , in the ENDOR spin Hamiltonian. The quadrupole tensor \tilde{Q}_i is defined as follows:

$$Q_{ik} = \frac{eQ}{2I(2I-1)} \left. \frac{\partial^2 V}{\partial x_i \partial x_k} \right|_{r=0} \quad (1.18)$$

Q Quadrupole moment of the nucleus,

V electrical potential at the site of the nucleus.

The quadrupole tensor is also traceless and can be reduced in analogy to the anisotropic shf tensor to

$$q = \frac{Q_{z'z'}}{2},$$

$$q' = \frac{Q_{x'x'} - Q_{y'y'}}{2}, \quad (1.19)$$

where q and q' are the quadrupole interaction parameters.

By definition, the z axes of the principal axes of the tensors are in the directions of the largest interactions, such that b and q are the axially symmetric parts of both tensors and b' and q' the deviations from axial symmetry, respectively. In many cases the tensors \tilde{A} and \tilde{Q} are symmetrical. Nuclei belonging to a so-called shell have the same interaction parameters. All nuclei within the shell have the same distance from the centre of the defect and can be made coincident by symmetry operations compatible with the defect symmetry. The angles describing the transformation of the principal axis system of an interaction tensor to the chosen crystal axis system are, as a rule, only given for one single nucleus within the shell in the form of three Euler angles. For a symmetrical hf/shf tensor there are consequently six parameters, the three interaction parameters a, b, b' and three Euler angles α, β, γ . For the quadrupole tensor there are five parameters. The number of free parameters can be reduced further by the symmetry of the considered shell (e.g.

mirror planes in which the connection lines between the neighbour nuclei of a shell to the defect centre are situated). If, e.g., the connection line of a neighbour nucleus to the defect centre is a three-fold axis, then all Euler angles are fixed and the shf and quadrupole tensors must be axially symmetric about this axis. Therefore, only a , b and q are free parameters.

ENDOR transitions obey the selection rules $\Delta m_S = 0$ and $\Delta m_I = \pm 1$. In a simple first order solution one obtains for the ENDOR frequency f_{ENDOR} for $b' = 0$ and $q' = 0$:

$$f_{ENDOR} = \frac{1}{h} \left| m_S \{ a + b[3 \cos^2(\theta_A) - 1] \} - g_n \mu_n B_0 + m_q 3q[3 \cos^2(\theta_Q) - 1] \right| \quad (1.20)$$

where m_q is the average value of the two nuclear quantum states m_I , m_I' , between which the nuclear transition take place. The angles θ_A and θ_Q are the angles between the direction of the static magnetic field B_0 and the z-axis of the correspondent (A and Q) tensors. By the measurement of an ENDOR angular dependence the parameters of the ENDOR Hamiltonian can be determined. For this the Hamiltonian is diagonalised in the frame of the effective spin approximation and the orientations of the principal axes of the interaction tensors are determined by a fitting procedure.

Chapter 2

Experimental aspects of the high-field/high-frequency MCDA-EPR/ENDOR: new developments

2.1 Introduction

Many properties of solids are controlled by point defects which play a key role in semiconductor physics with applications in micro- and opto-electronics. Therefore determination of their precise microscopic structure is an important task in applied science. There are many experimental methods to investigate the point defects in semiconductors, but not many deliver direct information about their local symmetry and distribution of spin density. Electron paramagnetic (EPR) and electron-nuclear double resonance (ENDOR) methods have proved to be powerful tools in such applications. EPR/ENDOR spectrometers have become standard tools in solid state spectroscopy.

Usual custom built EPR/ENDOR spectrometers are mainly designed for frequencies for which the microwave technology is sufficiently developed. X- and K- band spectrometers are widely used in physics, chemistry, and biology. Such spectrometers are commercially available. However, very often the advantages of the high-field/high-frequency EPR and ENDOR are decisive for the solution of a scientific problem. The choice of the higher frequencies is mainly governed by specific properties of the sample, the spin-Hamiltonian parameters as well as the aim of the study. High-frequency EPR and ENDOR has emerged in recent years as the method of choice to achieve a higher g-factor resolution, a gain in sensitivity, and to extend the range of accessible zero-field splittings, etc.

High-frequency EPR was started in the 1970s. In the pioneering work by Lebedev and co-workers the 2mm (140GHz) microwave range was used for the systematic EPR study of nitroxide spin labels [Grinberg 1976; Poluektov 1988]. In 1974 it was reported by Lukin et al. [Lukin 1974] about new high-field/high-frequency spectrometer (140GHz). Another pioneering work was initiated by Haindl, Burghaus, Möbius et al. with the construction of

a 94GHz EPR spectrometer using a Fabry-Pérot resonator [Haindl 1985; Burghaus 1992]. Since then in quite a number of laboratories high-frequency spectrometers have been constructed. Their frequencies range from about 75GHz, referred to as V-band, to the quasi-optical domain of up to 600GHz with infrared lasers as radiation sources. These home-built spectrometers are capable of either CW and/or pulsed EPR as well as electron nuclear double resonance (ENDOR). Since 1996, Bruker offers the first commercially available high frequency spectrometer for W-band with conventional detection of EPR and ENDOR. Their system can operate in either CW or pulsed mode at frequencies close to 94GHz.

However, the high frequency EPR/ENDOR systems still remain exotic and very specific. Such spectrometers are usually built on the basis of existent low frequency spectrometers (if the reachable magnetic field strength allows) to solve a certain problem, mainly in chemistry or biology. Very few laboratories in the world apply high frequency to the solid state [Weber et al.1998; Kalabukhova 1992; A. van Duijn-Arnold et al.1999]. All these spectrometers are built for the conventional detection of EPR and ENDOR.

In our laboratory of optically detected EPR and ENDOR of point defects in solids high-frequency/high-field investigations proved necessary. The problem was the microscopic structure of the EL2 defect in semi-insulating GaAs. Despite of more than two decades of research activities the question remained still a matter of discussion. The reason is that earlier EPR and ENDOR investigations of the EL2 defect were performed at relatively low magnetic fields (0.6-0.8T corresponding to K-band (24GHz) microwave frequencies). At such fields higher order effects such as pseudo-nuclear coupling and forbidden transitions complicated the K-band EPR and ENDOR spectra, therefore their analysis was not unambiguous [Hofmann 1984; Meyer 1987]. The conclusions could be incorrect. An increase of the magnetic field for the EPR and ENDOR investigations seemed the only way to reduce the influence of the higher order effects on the measured spectra (see Chapter 3). Therefore there was a need to introduce high-frequency instrumentation in order to get more reliable information about the symmetry and structure of the EL2 defect.

For that goal the open Fabry-Perot (TEM_{00q}) and cylindrical TE_{011} resonators for W-band EPR and ENDOR of single crystals were constructed and developed. Cavities are tunable

in wide frequency range ($\sim 500\text{MHz}$) and enabled us to detect the high field EPR and ENDOR spectra of the EL2 defect in semi-insulating GaAs optically via change of the magnetic circular dichroism of the optical absorption (MCDA-EPR/ ENDOR). Cavities operate at the pumped helium temperatures ($\sim 1.5\text{K}$). Under critical coupling the Q of the empty cavities at 1.5K was estimated to be ~ 5000 (2500 in ENDOR arrangement) and ~ 2000 , for Fabry-Pérot and cylindrical cavity respectively. In this chapter the cavities designs as well as arrangement of the high frequency part of the custom built MCDA-EPR/ENDOR spectrometer are presented and discussed. The advantages of high field spectroscopy of native defects in single crystals are demonstrated in Chapter 4.

2.2 W-band MCDA-EPR/ENDOR spectrometer

The block diagram of the high-frequency/high-field MCDA-EPR/ENDOR spectrometer is shown in fig.2.1. The computer controlled spectrometer operates at EPR transition frequencies around 94GHz (W-band, 3.2mm wavelength). The RF frequencies up to 500MHz can be delivered to the sample for ENDOR measurements. The optical detection of the EPR/ENDOR requires no microwave bridge, therefore the spectrometer is basically an optical spectrometer in which the light propagates parallel to the magnetic field.

For the detection of the MCDA signal low temperatures are favorable. Of course, for the high frequency MCDA-EPR/ENDOR high magnetic fields are required. Therefore the core of the spectrometer consists of an Oxford Instruments bath cryostat with a superconducting magnet in Helmholtz configuration. The maximum of the magnetic field available is 4T. Between the coils a sample chamber with light access windows is situated. The helium supply of the chamber is regulated by a needle valve. Temperatures between 4.2K and 1.5K can be reached by vapor pressure reduction of the helium in it. The temperatures above 4.2K can be produced by a heating. The heating system is composed of an electrical resistor mounted on the bottom of the microwave cavity, a carbon-glass temperature sensor and an automatic temperature controller (ITC4, Oxford) allowing to stabilize the temperature at any value between 4.2K and room temperature.

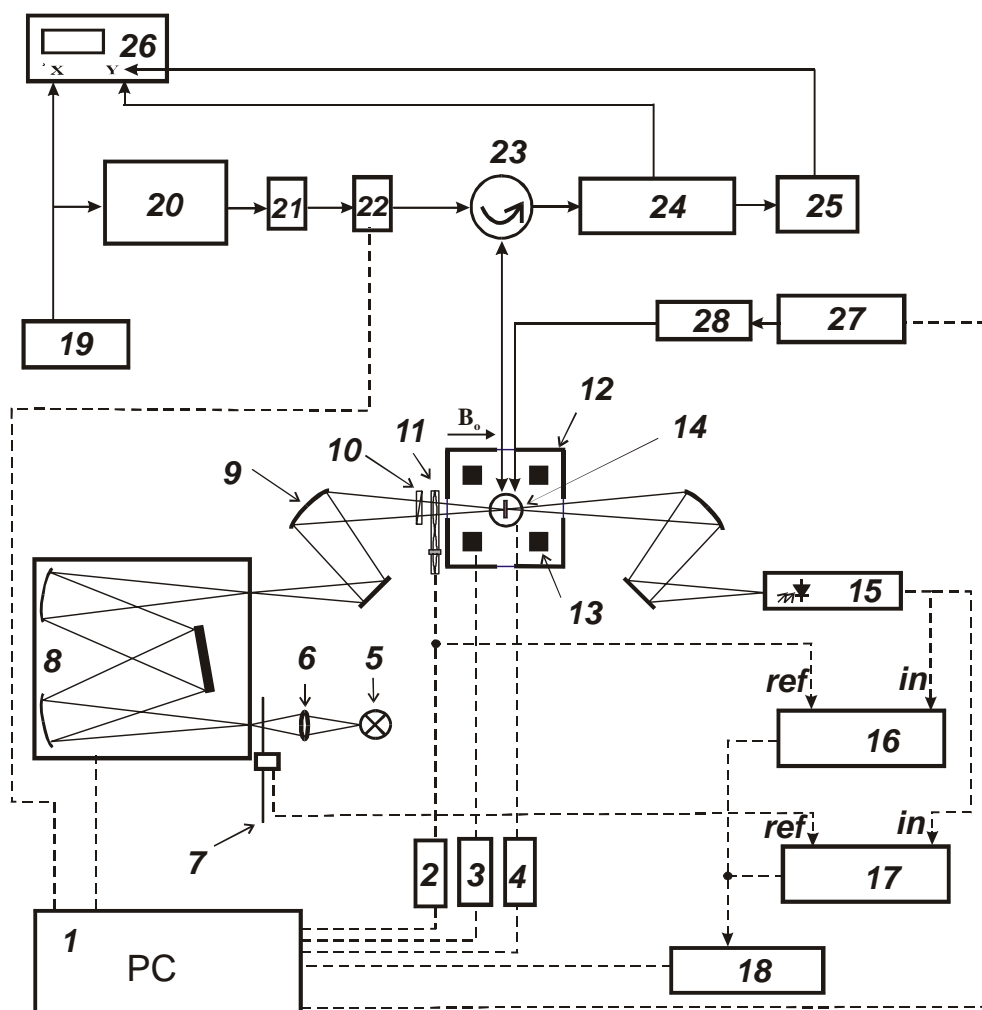


Fig.2.1 Block diagram of the W-band MCDA-EPR/ENDOR spectrometer. The

essential features of the spectrometer are:

(1) - PC; (2) - modulator controller; (3) - magnetic field controller; (4) - temperature regulation; (5) - halogen lamp; (6) - lens; (7) - chopper; (8) - monochromator (400-2500nm); (9) - concave mirrors; (10) - linear polarizer; (11) - acousto-optical modulator; (12) - bath cryostat; (13) - superconducting magnet; (14) - cavity with sample; (15) - Ge-detector; (16),(17) - lock-in amplifier; (18) - analogue/digital converter; (19) - low frequency modulator; (20) - microwave source; (21) - attenuator; (22) - pin-diode switcher; (23) - circulator; (24) - frequency meter; (25) - microwave detector; (26) - oscilloscope; (27) - RF source; (28) - RF amplifier.

The microwave tract consists of the following main parts: the microwave source (20); attenuator (21), pin-diode microwave switcher (22), circulator (23), microwave cavity (14), frequency meter (24), and the microwave detector (25). The optically accessible resonator cavities (cylindrical or Fabry-Pérot) with a sample inside can be placed into the liquid Helium chamber. The cavities are tunable to adjust their resonance frequency to the output frequency of the microwave source. Different sources can be switched depending on the aim of the measurements, two low noise Gun-diode oscillators delivering up to 110mW (Queen Star-Parzich GmbH) and the high-power CW IMPATT oscillator with the output power near 600mW (MicrowaveTechnologies). The cavities are coupled to the microwave source via a rectangular WR10 waveguide.

The main optical part of the custom built MCDA spectrometer consists of the following components (see figure):

- halogen lamp (5);
- lens and concave mirrors of the image forming system (6,9);
- monochromator (SPEX) (8);
- photo-elastic modulator (~30KHz) in combination with a linear polarizer (at 45°) for polarization modulation (11,10);
- the light detectors: liquid nitrogen cooled Germanium detector (North Coast) for the near IR spectral range (800-1700nm) and a GaAs-cathode photo-multiplier or Si-diode cell for the visible range (15).

The demodulation of the transmitted light through the sample is possible by means of a lock-in amplifier (16,17) (ITHACO). A chopper (7) can be used for the optical density measurements. The resulting voltage signal, proportional to MCDA, is delivered to a two-channel analogue/digital converter (18) (ITHACO). The data are stored in a PC.

Additional illumination can be applied from the side of the spectrometer. Various light sources combined with light pipes and a second monochromator can be used. With some modifications the MCDA-EPR/ENDOR spectrometer can be used for measurements of the optical density, absorption, photoluminescence, etc. More detailed information about the different components of the spectrometer can be found in the Ref. [Spaeth 1992].

2.3 W-band (94GHz) EPR/ENDOR multimode Fabry-Pérot cavity.

The microwave cavity is a very critical part of the EPR/ENDOR spectrometer. It influences the performance of the spectrometer to a very large extent. This is particularly true for a cavity operating at high microwave frequencies. The construction of such a cavity is not a trivial task. There are not many design approaches to the microwave resonators working at high frequencies and the number of the successfully working ones is even less [Lukin 1974; Burghaus 1992; Schmalbein 1999]. The constraints for the high frequency EPR cavity are very large. If one wants to construct the cavity for ENDOR measurements the problem is even more complex since in addition to the strong microwave field, B_1 , a sufficiently high RF magnetic field, B_2 , orthogonally orientated to B_0 and B_1 must be produced at the sample. The cavity coupling must be adjusted with extremely high precision, and rf interference effects as well as eddy currents in the cavity must be avoided. The capability of varying of the resonance frequency in a broad frequency range is desired. Another problem encountered in designing the ENDOR cavity is usually a need for a low sample temperature with almost no generation of microphonic noise. For MCDA-EPR/ENDOR measurements, for instance, the samples must be cooled to below liquid helium temperatures (1.5K). These low temperatures must be kept during the measurements while the high RF currents flow through the ENDOR rods and add to the thermal load of the superfluid helium bath. Finally, the Q-factor of the cavity must be high enough (even if the RF rods are incorporated inside) to allow the partial saturation of the EPR transitions in order to observe ENDOR.

The optical detection of the paramagnetic resonance leads to additional complications in the cavity construction because of the requirements of constant light access during the measurements. Furthermore, for the MCDA-EPR/ENDOR measurements on the solid state relatively large dimensions of the samples are required to avoid the problems with the optical image system. Such requirements are not easily satisfied in cylindrical or rectangular cavities where the closed configuration and extremely small sizes of the high frequency cavities cause a dramatic sensitivity loss when there are additional openings and when the sample size increases. The useful features of the Fabry-Pérot microwave resonators, such as high Q-factor and relatively large dimensions, were decisive in the choice of the cavity type for the W-band MCDA-EPR and ENDOR. The open scheme of

such a resonator allows convenient sample and light access. This was the motivation to construct the W-band EPR/ENDOR probe head with a Fabry-Pérot cavity.

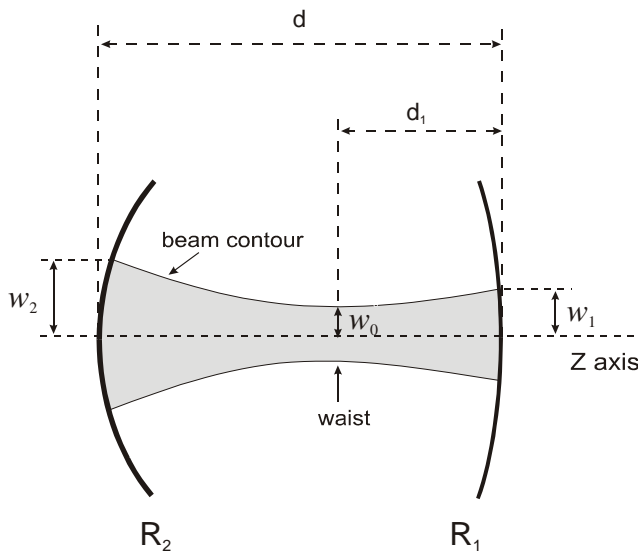


Fig.2.2 Open Fabry-Pérot resonance scheme with mirrors of unequal curvature.

The basic architecture of Fabry-Pérot resonators is composed of a pair of spherical mirrors, facing each other and separated by distance d . The sizes and the curvatures of the mirrors may vary but the circular form is the most common. Analytical solutions for the modes in such a cavity are presented in papers by Boyd and Gordon [Boyd and Gordon 1961], Fox and Tingye Li [Fox and Tingye Li 1961] and Kogelnik and Li [Kogelnik and Li 1966]. These modes (or a self-consistent field configurations) are essentially transverse electromagnetic and thus have negligible axial electric and magnetic field components. They are called TEM_{plq} modes where p is the radial, l the angular and q is the axial mode number which correspond not only to different frequencies but also to different field distributions. For $p=l=0$ the modes are particularly simple, consisting of $q+1$ sinusoidal variations of the microwave magnetic field ($\pi/2$ out of phase with the electric field variations) along the resonator axis. The radial field profile in the $p=l=0$ modes is Gaussian, so the diffraction losses in this open resonator can remain small.

When the concave mirrors have the radii of curvature R_1 and R_2 and are separated by a distance d (see fig.2.2) the stable resonance conditions for such a system require that

$$0 < \left(1 - \frac{d}{R_1}\right)\left(1 - \frac{d}{R_2}\right) < 1 \quad (2.1)$$

At such condition the spectrum of the Fabry-Perot resonator depends principally on the distance between the mirrors and the resonance equation for a certain mode is given by

$$2\frac{d}{\lambda} = q + 1 + \pi^{-1}(2p + l + 1) \cos^{-1} \sqrt{\left(1 - \frac{d}{R_1}\right)\left(1 - \frac{d}{R_2}\right)} \quad (2.2)$$

where λ is the wavelength of the microwave [Kogelnik and Li 1966].

The mirrors cause a focusing action on the microwave beam giving an hourglass shape. The minimum, or waist, of this profile at the distance d_1 from the mirror 1 is given by

$$w_0^4 = \left(\frac{\lambda}{\pi}\right)^2 \frac{d_1(R_1 - d)(R_1 + R_2 - d)}{(R_1 + R_2 - d)} \quad (2.3)$$

where

$$d_1 = \frac{d(R_2 - d)}{R_1 + R_2 - 2d} \quad (2.4)$$

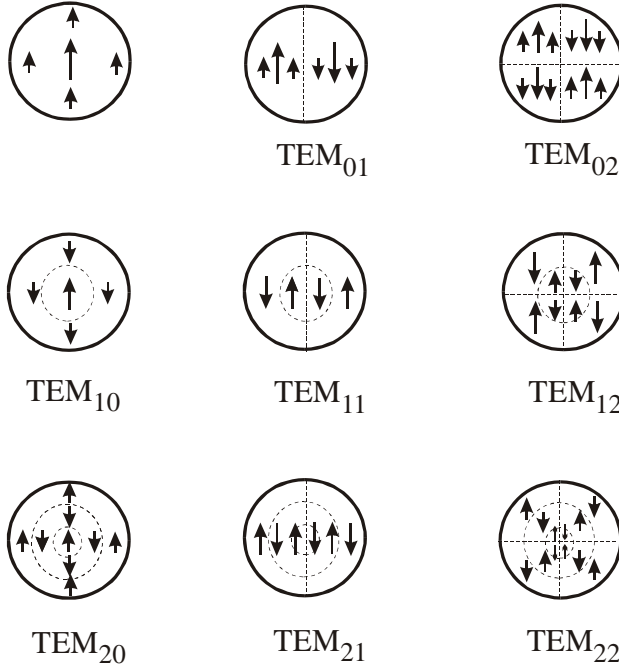
The diameter of the beam at the mirrors of a stable resonator, $2w_1$ and $2w_2$ (see fig.2.2) are given by:

$$w_1^4 = \left(\frac{\lambda R_1}{\pi}\right)^2 \frac{R_2 - d}{R_1 - d} \frac{d}{R_1 + R_2 - d} \quad (2.5)$$

$$w_2^4 = \left(\frac{\lambda R_2}{\pi}\right)^2 \frac{R_1 - d}{R_2 - d} \frac{d}{R_1 + R_2 - d} \quad (2.6)$$

For nonfundamental modes ($p \neq 0$ and $l \neq 0$) the Gaussian shape of the fundamental mode radial profile is multiplied by the Laguerre polynomial $L_p^l(2r^2/\omega(z))$, where r is a radial coordinate and $\omega(z)$ - axially dependent beam waist. These modes are distinguished from the fundamental ones by their higher field density at the large values of r , and lower field densities at the sample with increasing l and p (see fig.2.3).

TEM₀₀ - mode



densities at the sample with increasing l and p (see fig.2.3).

Fig.2.3 Linearly polarised resonator mode configurations for circular mirrors (after Kogelnik and Li [Kogelnik and Li 1966])

Such modes are clearly unfavorable for EPR/ENDOR. Choosing the TEM_{00q} mode as a main operation mode of the

resonator one has to couple the cavity with the waveguide properly to have, at least, the desired (microwave) magnetic field orientation. Then the higher modes shown in the figure 2.3 can be suppressed by choosing an appropriate aperture size. The figure of merit in this regard is the Fresnel number, $N=D^2/4\lambda d$ (D is the diameter of the mirrors). With the Fresnel number of one ($N=1$) there is support of the fundamental mode but and the suppression of nonfundamental modes.

In case where the radii of the curvatures of the two mirrors are equal ($R_1=R_2=R$), the confocal arrangement of the mirrors ($R=d$) leads to a considerable degeneracy of the higher modes in the resonator. The various modes occur in small groups in the close neighbourhood of the resonance frequency [Boyd and Gordon 1960].

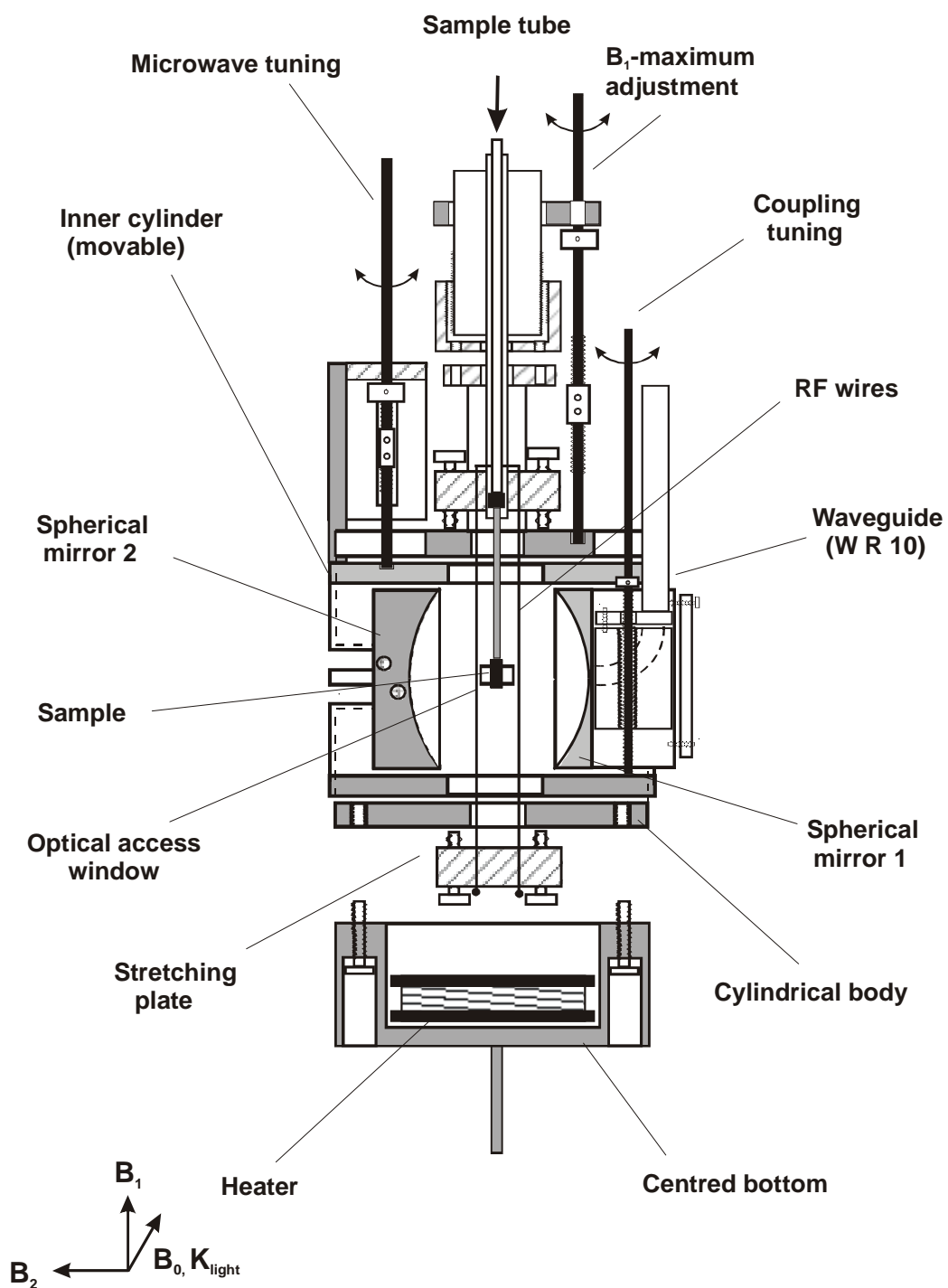
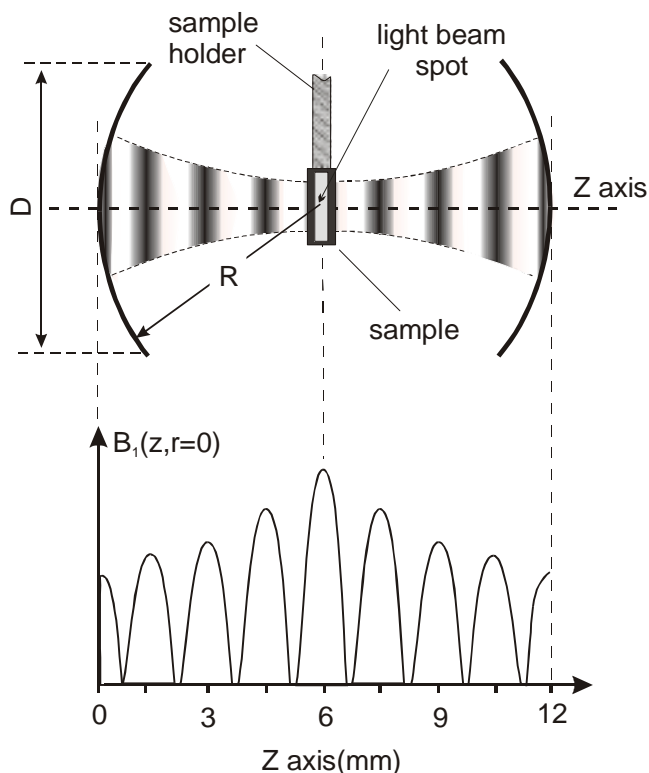


Fig.2.4 W-band Fabry-Perot cavity for MCDA-EPR/ENDOR (whole assembly)

The successful design of the Fabry-Perot cavity for W-band MCDA-EPR/ENDOR is shown in figure 2.4. The cavity was designed for low temperature operation (down to 1.5K). The axis of the cavity is placed perpendicular to the axis of the external B_0 magnetic field and the light propagation direction. The resonator consists of two concave spherical mirrors with equal diameters ($D=17\text{mm}$) and radii of curvature ($R=14\text{mm}$). The



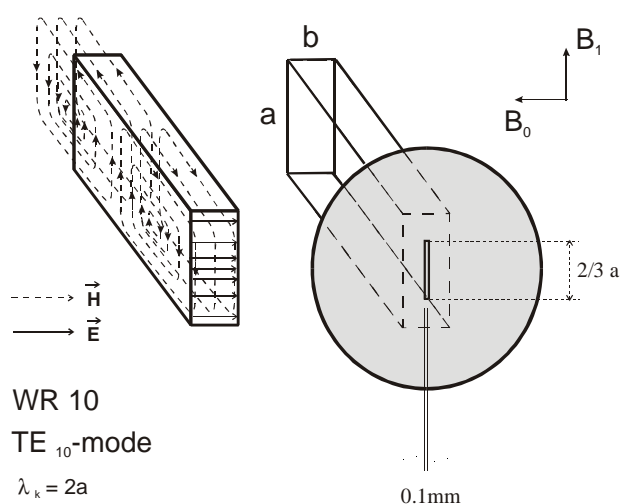
mirrors milled from the brass and polished to quasi-optical standards are silver coated to increase the conductivity of the skin layer and, therefore, the Q-value of the resonator. The thickness of the electroplated silver layer equals a few times the penetration depth of the microwaves at frequencies near 94GHz.

Fig.2.5 The sample position and axial magnetic field strength distribution within the Fabry-Pérot resonator for TEM_{00q} ($q=8$) mode.

The mirror distance can be tuned by a fine thread to adjust the resonator frequency to the microwave source frequency. Furthermore, the simultaneous movement of both mirrors (which are already in resonant arrangement) along the axis of the resonator is provided. This enables us to bring the maximum of the microwave magnetic field to the spot where the sample is exposed to the light (see fig.2.5). It is important for the MCDA detection of EPR/ENDOR where the requirement of the persistent optical adjustment during the measurements does not permit to move the sample along the resonance axis. It allows also to keep the constant position of the sample in the RF (B_2) magnetic field maximum. The sample can be inserted into the cavity from the top of the cryostat without taking out and warming up the whole probe-head. This enables a quick change of samples during the experiment. The investigated samples can be rotated around the vertical axis (see fig.2.5).

The cavity is coupled to the rectangular waveguide WR10 ($a=2.54$ mm, $b=1.27$ mm) via an extremely small slit in the wall of one of the mirrors (fig.2.6). The waveguide is oriented with the H-plane perpendicular to the static magnetic field, B_0 . The slit was made by electro-erosion and works as an electromagnetic polarizer enabling the coupling mostly with the dominant TE_{10} mode and suppressing the coupling with the modes having other field orientations. Designs of different schemes for tuning of the coupling to its critical value were not successful. Therefore, in the last version, the waveguide was simply soldered to the mirror. The optimum slit size for the matching of the cavity to the source was determined by trial and error. The coupling slit width is $W=0.1$ mm while its length is equal to $L=1.7$ mm ($2/3$ of the “a” dimension length (2.54mm) of the used WR10 waveguide). The thickness of the mirror wall around the iris (slit) (which should be as small as possible to avoid undesirable losses of the microwave power) does not exceed the value of 0.1mm.

Fig.2.6 Coupling configuration with the dominant TE_{10} transverse electric mode ($E_z=0$, $H_z \neq 0$).



In practice the cavity is used near the confocal arrangement in the region of the stable resonance condition (see eqn.3.1). But the frequency of operation is chosen in such a way that the high mode degeneracy, which occurs at exact confocal mirror arrangement ($d=R$), is avoided. The basic modes TEM_{00q} occur with spacing $\Delta d = \frac{1}{2} \lambda$ while higher modes with $l \neq 0$ may also occur with spacing $\Delta d = \frac{1}{4} \lambda$. The choice of the mode most appropriate for the experiment was performed by measuring the intensity of the MCDA-EPR signal as a function of d and the distance between the sample and the center of the cavity. In the ENDOR experiments the fundamental TEM_{00q} mode with $q=8$ was used, giving the highest EPR signal intensity.

The construction of the ENDOR coils around the sample is determined by the fact that the wires must be parallel to the magnetic field direction of the TEM_{00q} mode. We used four parallel wires forming a pair of Helmholtz coils (see fig.2.7), with one loop per coil for optimum RF field homogeneity. The B_2 field oriented horizontally (i.e. along the axial

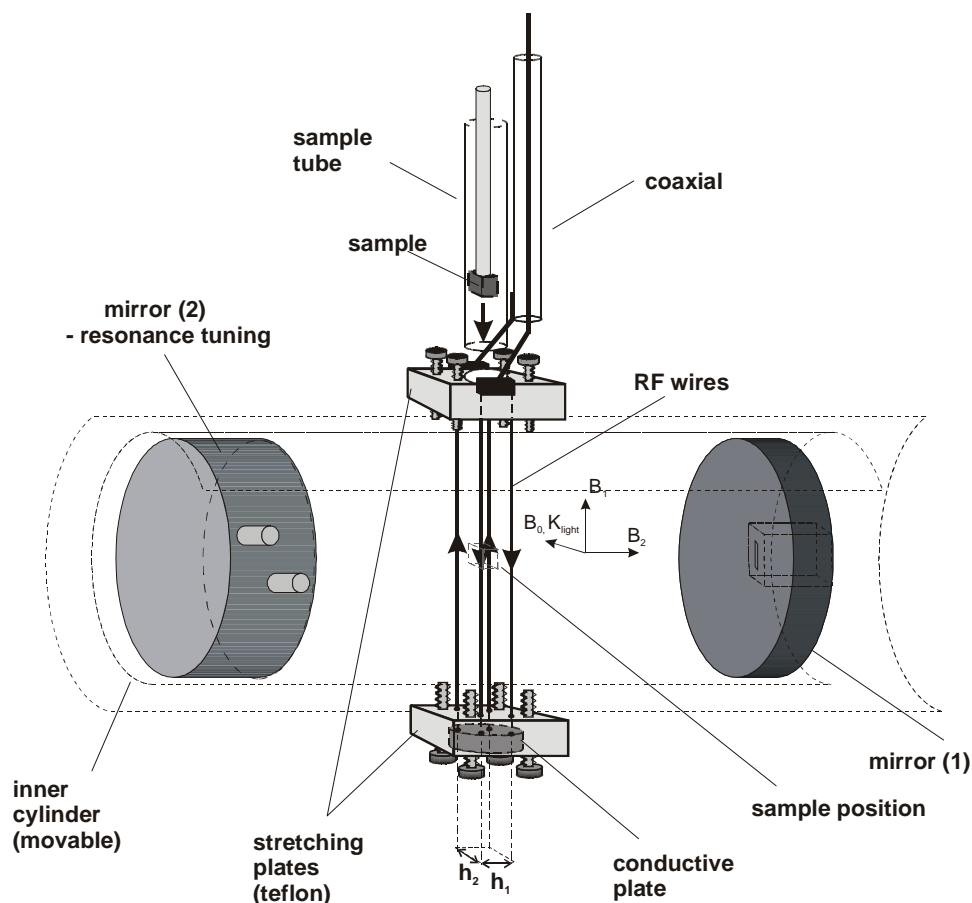


Fig.2.7 ENDOR coil configuration

direction of the cavity) is generated by an RF current flow through the wires. It can be calculated that in this arrangement the RF field homogeneity is best when the ratio of the distances h_1/h_2 is equal to $\sqrt{3}$. To increase the strength of the RF field the wires are positioned very close to the sample site, h_1 and h_2 were chosen to be 2.5mm and 4.3mm, respectively. The RF wires are in fact hair-pin (diameter $D=0.3$ mm) silver wires stretched

across the cavity. The wire length is 25mm. The insertion of such wires reduced the Q-factor of the cavity approximately by factor 2. The wires are firmly anchored in the upper plate, passed freely through the cavity close to the sample and then attached to the fixed plate below the cavity that served to stretch the wires. Stretching the wires prevent them from vibrating in the external (B_0) magnetic field. A vibration of the RF wires would otherwise change the cavity parameters. Teflon isolation prevents unwanted shorting of the wires within the upper and lower plates. The RF power from the source is transferred with a semirigid coaxial cable (OD 1mm). The characteristic impedance of the coaxial cable and the wires is close to 50Ω at 150MHz matching the output impedance of the RF high-power amplifier(50Ω). RF frequencies of up to 300MHz could be applied without noticeable fluctuations of the hf-currents in the wires. A partial (simplified) cross-sectional view of the ENDOR arrangement is shown in fig.2.7

The loaded Q_L -factor of the cavity is strongly determined by the diffraction losses due to the incorporation of the sample. With the optimum shape of the sample and at some orientations of it the diffraction losses can be minimized. By doing so the value of Q_L of about 400 can be achieved while the Q-factor of the empty cavity is about 2500.

2.4 Tilt corrector

As a component of the Fabry-Perot cavity a special sample holder was designed in order to ensure a correct sample orientation. One has problems when the sample under investigation is not exactly oriented with its crystallographic axes relative to the external magnetic field. In general, such a deviation, which is not noticeable for the “naked” eye, is very small and lies in the experimental error bar. However, there are the scientific problems where even such a small error in the experiment can result in incorrect conclusions about the symmetry of a paramagnetic center and, therefore, is not acceptable. Such a case was found when analyzing the EL2 defect. The splitting of the equivalent ENDOR lines was observed in the W-band MCDA-ENDOR spectra of the first neighbour shell of the EL2 (see Chapter 3). The question arose, whether the splitting is caused by the tilt of the crystal or by the physical non-equivalency of the nearest neighbours.

Therefore, there was a need to control the tilt of the crystal more precisely and, if it exists, to eliminate it.

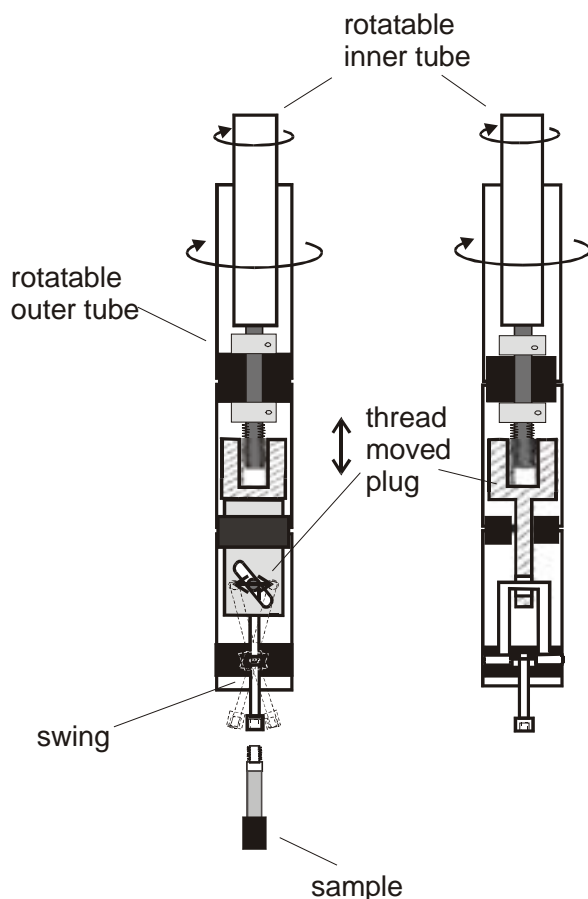


Fig.2.8 Sample holder (tilt-corrector) allowing to eliminate the deviation of the measured crystal orientation from the expected one.

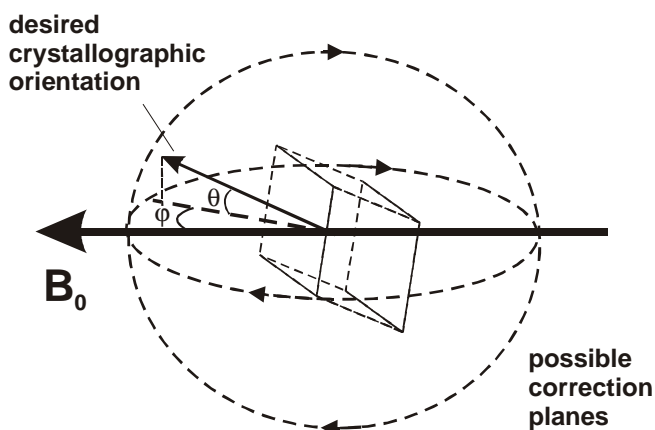
The control of the tilt was performed with the beam of He-Ne laser reflected from the sample, the deviation of which from the etalon direction indicated the tilt of the crystal (see fig.3.14, Chapter 3). It should be noticed that such a control is efficient only if the surface of the crystal coincides with the crystallographic plane. For this the precise preparation of the sample with

the X-ray control is necessary. The correction of the tilt of a few degrees was accomplished with the sample holder (tilt corrector) sketched in the figure 2.8

The sample holder (corrector) allows to eliminate the tilt of the sample in the head of the cryostat already prepared for measurements at pumped liquid He temperatures. After insertion into the resonator the sample can be rotated in two perpendicular planes (see figure 2.9) what is enough to meet exactly the main crystallographic orientations of the sample. That enables one to get immaculate ENDOR spectra (not influenced by the tilt) at least for the main crystallographic directions. The whole assembly (outer tube) is only 6mm in diameter, therefore the parts of the device have watch-gear-like sizes and the preparation of such a mechanism is work for a fine mechanic. It consists of two tubes (see fig.2.8). An outer one for rotation of the whole device in the horizontal plane and an inner

tube for the movement of the small inserted plug. The thread moved plug (the rotation of it is prevented) pushes one of the ends of the swing and as a result the second end with the sample is tilted.

Fig.2.9 The possible rotation planes for the tilt correction provided by the sample holder.



This contra-tilt enables us to correct the possible deviation of the crystallographic axis in the range $\pm 3^\circ$ in the vertical plane without dramatic displacement of the sample from the radial centre of the microwave beam in the Fabry-Pérot resonator (up to 1mm). In the horizontal plane the correction can be made without any restrictions.

2.5 W-band TE_{011} -mode cylindrical cavity

The advantages of the Fabry-Pérot resonator for optically detected EPR in W-band are accompanied by some disadvantages, such as a low power-to-field conversion factor and high diffraction losses of microwaves on the samples. That is why we decided besides the construction of the Fabry-Pérot cavity to design a cylindrical cavity for W-band EPR/ENDOR as well.

In general, cylindrical cavities can support TE_{mnp} modes (as well as TM_{mnp}) where the subscripts m , n , and p indicate the number of half-cycle variations in the angular (ϕ), radial (r), and the longitudinal (z) directions, respectively. These modes can be derived from the TE_{mn} cylindrical waveguide modes or equivalent TE_{mn} modes propagating in the rectangular waveguide (here the m and n indexes mean the number half-wavelength variations in x and y directions).

The resonance frequency of the cylindrical cavity for a certain mode is related to its dimensions by the following equation:

$$f = \frac{\sqrt{\left(\frac{c(k_c a)_{mn}}{\pi}\right)^2 + \left(\frac{cp}{2}\right)^2 \left(\frac{2a}{d}\right)^2}}{a\sqrt{2}} \quad (2.7)$$

where a is the radius of the cavity while d is its length; c is the velocity of light in vacuum and $(k_c a)_{mn}$ is a Bessel function root, since cylindrical modes have Besseloid radial variations. The quantity $(k_c a)_{mn}$ is the n^{th} root of the m^{th} -order Bessel function $J_m(k_c r)$. The dominant mode of the cylindrical cavity is the TE_{111} mode. But for the EPR/ENDOR cavity this mode is inconvenient. Normally the cavities of the TE_{011} mode are used for such applications because of the high Q of the mode. For the TE_{011} mode the Bessel function root is equal to 3.832 [Poole 1996]. For the design of a resonant cavity it is desired to select values of a and d such that there are no extraneous modes that have resonant frequencies near the designed ones. Here one should take into account that the highest Q-factor for the TE_{011} mode is reached when the length d of cavity is equal to its diameter $2a$. The strong magnetic field along the cavity axis makes the TE_{011} mode particularly useful for a sample cavity. In such a cavity there is no hf current flow between the cylinder walls and its top and bottom. In fact there is no electric current flow in either the radial (r) or longitudinal (z) direction, but only in the angular (ϕ) direction. This property enables one to tune the cavity using the plunger on the end of the cylinder as shown in fig.2.10. The resonance frequency of the cavity may be varied moving the plunger axially. The current flow renders it unnecessary to achieve good electrical contact between the plunger and the cylinder. If some gap between the walls and the plunger edges is left then other modes will be suppressed because they require the current to flow across this gap. Particularly the TM_{111} mode, which is degenerate with the TE_{011} mode, will be suppressed. Very useful is that it is possible to have a large hole in the top and bottom of the resonator without a noticeable decrease of the Q-factor. Such a feature enables one to insert reasonably large samples into the cavity axially (see fig.2.10).

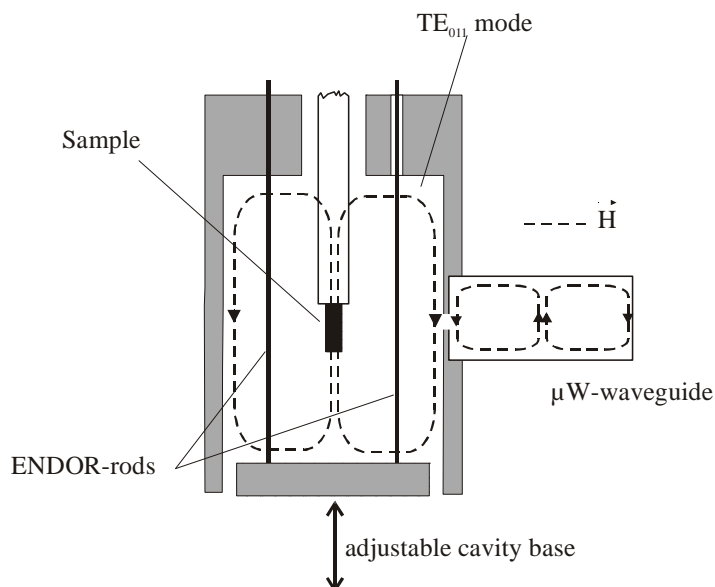


Fig.2.10 Tunable TE_{011} mode cylindrical resonant cavity

The main advantage of the TE_{011} cavity is its small and compact volume that results in high energy density and the high magnetic field strength B_1 in the center of the resonator. But the same feature (small volume) causes serious problems if one designs such a cavity for the high frequency (95GHz) optically detected EPR and, particularly, ENDOR measurements. As was mentioned already, in contrast to conventional EPR, there is a need for a good optical access to the sample. An RF field B_2 amplitude must also be provided for ENDOR. Furthermore, one must solve the problem of the coupling of such a cavity. These conditions must be fulfilled in the cavity working volume of which is in the range of several mm^3 only.

One of the design approaches to the TE_{011} cylindrical cavity for W-band MCDA detected EPR/ENDOR is sketched in the fig.2.11. The cavity can be described as a two top hats held opposite to each other with the 0.5mm separation. These hats form the cylindrical body of the cavity. The distance between hats and width of their brims (0.75mm) were chosen such that the cut off wavelength condition is fulfilled, i.e., no microwave can escape. This configuration of the hats actually repeats the idea of optical access to the sample realized previously in our laboratory for K-band (24GHz) a TE_{011} cavity for MCDA-EPR/ENDOR [Spaeth 1992].

The diameter, D , of the cavity is equal to 4.2 mm. The bottom of the cavity traditionally is a plunger and can be moved, therefore the cavity length can be changed from 4 mm to 15 mm, which enables us to tune the cavity in a broad frequency range. That is particularly important in the W-band range where even a small change of the sample parameters (dimensions, dielectric constant, etc.) causes a dramatic shift of the resonance frequency. But the commercially available microwave sources for such frequencies (Gunn, IMPATT) have usually a narrow range of the frequency generation ($\sim 500\text{MHz}$). Because of the small sizes of the cavity the usual way of the sample incorporation from the top of the cryostat (more than 1m length) is problematic. Therefore the sample is inserted together with the top of the resonator having the role of the sample holder. For the same reason (small sizes of the cavity) the incorporation of the ENDOR rods into the cavity leads to an unacceptable decrease of its quality factor Q . Therefore, the RF coils, which are in the

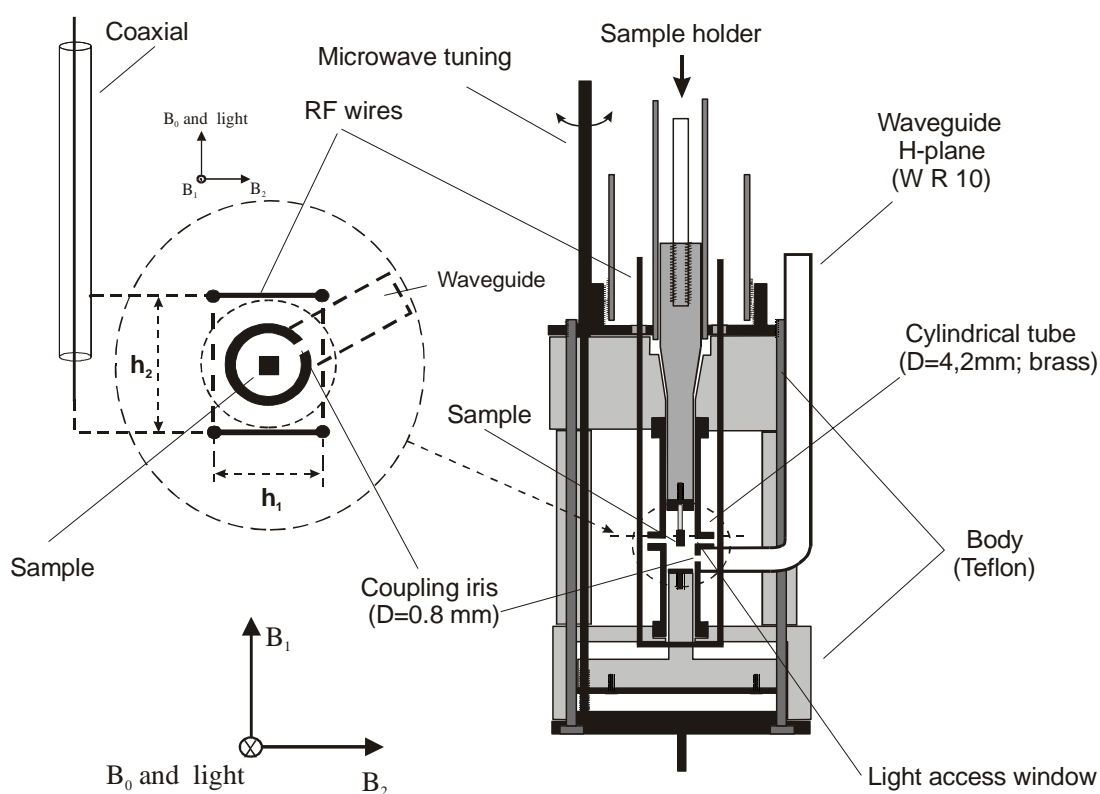


Fig.2.11 W-band cylindrical MCDA-EPR cavity

same configuration as described in the previous section (Fabry-Pérot resonator, fig.2.7) and depicted in fig.2.11, were placed outside of the working volume of the cavity. Here the h_1 and h_2 separation values are equal to 5 mm and 8.7 mm, respectively. Such a decision requires almost all parts of the cavity, which are in the close vicinity to the rods, to be made of teflon to avoid the eddy currents induced in conductive materials while the RF electromagnetic field is applied. Only the working parts (cylinder, top and plunger) and the parts which require the mechanical stability are made of brass. To minimize the losses of RF power because of the eddy currents in the cylinder and to reach a B_2 magnetic field large enough, the metallic walls of the cylindrical body (hats) have a thickness ~ 0.2 mm which is enough for a skin depth penetration of the W-band microwave frequencies. In such a way the losses caused by the eddy currents are strongly diminished and the B_2 magnetic field strength inside the cavity is reduced only by factor 4 in comparison with the “free way” operation.

Coupling with the WR10 rectangular waveguide is performed with a small coupling iris from the back side of the cylinder. The coupling is made in such a way that the magnetic field orientation of the dominant TE_{10} mode propagating in the waveguide is parallel to the axis of the resonator. The diameter of the coupling iris equals to 0.8 mm. The iris is located at the point in the cavity where the B_1 magnetic field is strong and has the same orientation as the magnetic field in the waveguide. The diameter of the coupling hole was determined by trial and error. The incorporation of the different coupling mechanisms (plunger, Smith chart, needles, etc.) was complicated because of the small sizes of the cavity and the lack of space in the helium filled sample chamber which requires a drastic (but reasonable with regard to the attenuation) bending of the waveguide on the end.

Chapter 3

The EL2 defect in semi-insulating GaAs:

W-band MCDA-EPR/ENDOR investigation of the microscopic structure

3.1 Introduction

The EL2 defect is probably the most discussed native point defect in semiconductors. It occurs in non-stoichiometric GaAs grown by both liquid-encapsulated Czochralski (LEC) and horizontal Bridgman (HB) technique. It is a dominant deep donor, commonly observed in concentrations of about 10^{16} cm^{-3} , which compensates residual acceptors and causes the semi-insulating (SI) property of the material.

The interest in EL2 comes from its technical importance and fundamental properties. SI GaAs is widely used as a substrate material in the technology of high-speed devices and integrated circuits. The scientific interest in EL2 comes mainly from its metastability. The EL2 defect can be transferred (bleached) into a metastable state at low temperature ($< 140 \text{ K}$) by light illumination in the photon energy range of 1.0 to 1.3 eV. In the metastable configuration the EL2 defect is electrically and optically inactive, at least at very low temperatures. The metastable properties of the EL2 defect are seen in the optical absorption, the EPR, MCDA and in photo-capacitance measurements. The ground state of the defect can be recovered from the metastable state by heating above 130 K. The thermal barrier of the recovery transition is 0.34 eV.

For almost two decades the structure model of the EL2 defect has been controversially discussed. In spite of intensive investigations there is no consensus about this question. It is clear that the EL2 structure contains an As atom on a Ga site, As_{Ga} , however neither the isolated As_{Ga} with T_d symmetry, nor the $\text{As}_{\text{Ga}}\text{-As}_i$ pair model (C_{3v} symmetry) nor any other As_{Ga} -related defect model could be unambiguously established.

The reason of the controversies is related to independent experimental and theoretical investigations. The interpretation of the EL2 as the isolated As-antisite was based mainly on the results of piezo-spectroscopic experiments performed by Kaminska et al. [Kaminska 1985], where the uniaxial stress splitting of the so-called zero-phonon line (ZPL) of the optical absorption in various crystal orientations was studied. The underlying assumption of the experiments was that the observed characteristic absorption band at about 1.18 eV which begins with the ZPL at 1.039 eV and phonon replica separated by 11 meV results from the $A_1 \rightarrow T_2$ intradefect transition. In the frame of this model the absorption with its ZPL must be sensitive to the structure of the EL2. This view has been widely accepted, however it can be challenged. The experiments done by Baj and Dreszer [Baj and Dreszer 1989] showed that the ZPL and the 1.18eV absorption bands shift in opposite sense under hydrostatic pressure. Another interpretation was made in which the sharp line is connected with a transition to the L-point of the conduction band. The observed splitting could be the result of the symmetry of this conduction band minimum [Skowronski 1987; Bardeleben 1989; Lannoo 1991]. However, the photo-luminescence investigations of the EL2 ZPL under uniaxial stress have yielded further arguments for the model of the isolated As_{Ga} defect [Nissen 1991].

The isolated As_{Ga} model of the EL2 was favoured by the theory to explain its metastability. The transition to the metastable state was predicted theoretically as a flip of the isolated As_{Ga} atom through one of the walls of the surrounding tetrahedron into an interstitial position leaving a $V_{Ga} - As_i$ configuration [Chadi and Chang 1988; Dabrowski and Scheffler 1988]. The question arises, however, whether a complex defect which involves an As antisite can also have such a transfer. Three different As antisite defects, which were identified and investigated in electron-irradiated GaAs [Spaeth and Krambrock 1994; Wietzke 1997], show also metastable properties. The optical process and the transition probabilities differ between the different As antisite species, while the thermal recovery temperature is with about 140 K always nearly the same. It must be an indication of the same fundamental process.

In the first MCDA-ODENDOR spectra of the EL2 defect performed in K-band [Hofmann 1984; Meyer 1987] splittings of the ENDOR lines in the first and higher As neighbour shells were observed in addition to ENDOR lines interpreted as stemming from an As

atom in an interstitial neighbour position. All these observations were explained with a C_{3v} symmetry of the EL2 defect, lower than T_d . Later MCDA-ODENDOR of electron irradiation-induced As_{Ga} -related defects at low temperature revealed an As antisite defect which was attributed to the isolated As_{Ga} defect with higher symmetry (T_d) compared to the EL2 defect [Krambrock 1992]. It was found that the new As antisite exhibits a single derivative like MCDA and is not stable at room temperature. This view was confirmed with MCDA-ODENDOR measurements which showed that the splitting of the higher neighbour shell resulting from the symmetry lowering is characteristic only for the EL2 defect while for the new isolated antisite no such splitting was observed [Krambrock and Spaeth 1992].

The lower symmetry of the EL2 defect was also supported by time-resolved phonon transmission experiments with pulsed phonons of different polarizations and different propagation directions before and after the metastable transition [Culbertson 1987]. The same conclusion that the EL2 defect has C_{3v} symmetry was made after the observation of the strong anisotropy effects in the electron emission processes under electrical fields [Dobaczewski 1988].

From all low symmetry models proposed for the EL2 the main attention was attracted by the complex where the As antisite and an interstitial As atoms are paired making up the $As_{Ga}-As_i$ defect with C_{3v} symmetry. This model was first postulated from a combined study of electron paramagnetic resonance (EPR) and deep level transient spectroscopy (DLTS) [Bardeleben 1986]. Later the model was supported by Meyer et al. [Meyer 1987] with MCDA-ODENDOR experiments in K-band which showed the lower symmetry of the EL2. The C_{3v} symmetry of the defect was deduced from the splitting of the ENDOR lines of the first As shell as well as the splitting of the higher As neighbour shell into two subshells. Furthermore, additional As ENDOR lines were observed which were attributed to an As_i atom [Meyer 1987]. However, the main problem with the $As_{Ga} - As_i$ pair defect comes from theory which calculated only a very weak binding of the As_i atom to the As-antisite and electronic levels close to the conduction band [Dabrowski and Scheffler 1988; Dabrowski and Scheffler 1989]. Later the model was questioned by simulations of the EL2 EPR line width which revealed a strong contradiction of the simulated EPR lines

(if the $As_{Ga}-As_i$ model was assumed) in comparison with the experimental ones measured in X- and K-band [Wirbeleit 1997].

The ENDOR spectra of a paramagnetic point defect in a crystal can be regarded as the most direct source of information about its microscopic structure, therefore, the $As_{Ga}-As_i$ model has been accepted as one of the main models amongst those confirming the lower symmetry of the EL2 defect. However, many more experiments of the MCDA-ENDOR spectra of the EL2 defect have led to doubts on the right interpretation of the results of the EL2 defect. One of the reasons is that the MCDA-ODENDOR was measured at relatively low magnetic fields (700 - 900 mT, K-band microwave frequencies). At those fields the large hyperfine interaction (hf) with central ^{75}As nucleus (~2660 MHz) and with the nearest neighbours (~200 MHz), which is characteristic for the EL2, is responsible for higher order effects in the ENDOR spectra such as pseudo-dipolar nuclear coupling and forbidden transitions. The additional splitting of the ENDOR lines because of the nuclear-nuclear interaction and the occurrence of “forbidden” lines complicate the experimental K-band ENDOR spectra. Their unambiguous analysis is difficult and for some orientations even impossible.

Clearly, up to now no experiment has been performed which would solve the problem definitely. Therefore, to get more precise and reliable information about the EL2 structure high-field EPR and ENDOR investigations were necessary. At high magnetic fields it was expected to simplify the spectra, eliminating the undesirable influence of higher order effects.

3.2 Fingerprints of the EL2 defect in GaAs

Before the MCDA-ENDOR experiments using different GaAs samples are described, the signatures of the EL2 defect from the experimental spectra must be reliably identified. There are some features which are characteristic for the EL2. They should be mentioned here because we used them to recognize the defect with magneto-optical methods. These features are:

3.2.1 Optical absorption: Figure 3.1 shows the near infrared absorption spectrum of the EL2 which is commonly observed in n-type and semi-insulating GaAs. The absorption begins at 0.8eV with photoionization transitions from the midgap donor level to the Γ valley of the conduction band. At 1.1 eV there is the onset of transitions to a higher conduction band resulting in the rapid increase of the slope (see fig.3.1 (a)). The prominent feature is the absorption band which begins at 1.039 eV with the ZPL followed by phonon replicas and is superimposed on the photoionization background (fig.3.1 (c)). This band was interpreted as the intracentre transition from the ground state of the defect into its excited T_2 states ($A_1 \rightarrow T_2$ intracentre absorption).

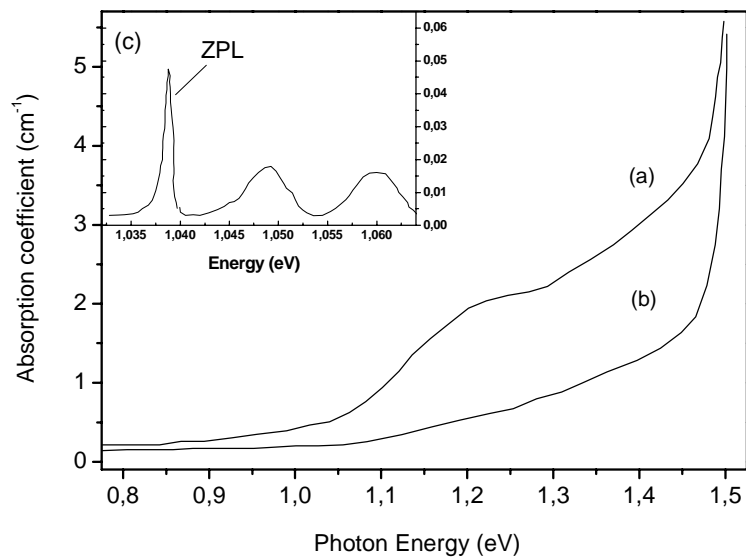


Fig. 3.1 Near infrared absorption spectra of the EL2 defect in SI GaAs recorded at low temperature ($T=1.5$ K) before (a) and after (b) bleaching of the defect with light illumination (photon energies $h\nu < 1.2$ eV). Line (c) is the so-called Zero Phonon Line (ZPL) of the NIR absorption with the phonon replicas.

It is important that the optical absorption can be quenched by light illumination at low temperatures. After exposure of the samples with light in the photon energy range of 1.0 to

1.3 eV the EL2 defect becomes optically inactive (line b). The near infrared absorption shown in the figure was attributed to the neutral charge state of the EL2. When EL2 is partially quenched, the whole absorption band is quenched by the same factor. The magnitude of the ZPL is proportional to the entire band which is proportional to the concentration of the EL2 determined by DLTS in n-type GaAs [Martin 1981; Skowronski 1986].

3.2.2 MCDA: The prominent fingerprint of the EL2 defect is its MCDA spectrum. In figure 3.2 the typical MCDA spectrum of GaAs containing $EL2^+$ and $EL2^0$ is shown. It was measured at $T=1.5$ K where the well-known paramagnetic MCDA bands of the $EL2^+$ centred at about 0.95, 1.1 and 1.32 eV dominate the spectrum. The intensities of the bands depend on the temperature as well as the externally applied magnetic field. The lower the temperature of the sample the higher intensity of the MCDA bands due to the higher spin polarization of the Zeeman levels of the defect ground state. With increase of the magnetic field the MCDA intensity is higher. At high temperatures the paramagnetic bands vanish. At $T > 140$ K only two weak temperature-independent diamagnetic ($EL2^0$) bands around 0.93 and 1.19 eV can be observed [Wietzke 1997]. After light exposure ($1.0 \text{ eV} < h\nu < 1.3 \text{ eV}$) the paramagnetic as well as the diamagnetic MCDA bands disappear completely.

According to Meyer et al. [Meyer 1984] the EL2 MCDA arises from intracentre transitions from the A_1 ground state to two T_2^a and T_2^b excited states, which result from the splitting of the T_2 state by the low defect symmetry. (fig.3.2 (right)). The A_1 ground state lies at 0.52 eV above the valence band and the two T_2 states are 1.05 and 1.29 eV above the A_1 state resonant with the conduction band. The MCDA is then the superposition of two derivative-like bands finding their origin in the Zeeman splitting of the ground state and spin-orbit splitting of the p-like excited states.

Previous MCDA and MCDA-ENDOR investigations of different As_{Ga} -related defects in electron-irradiated GaAs revealed the high sensitivity of the MCDA to small changes in the defect microscopic structure [Spaeth and Krambrock 1994]. Therefore, the MCDA spectra can serve as fingerprints of the different defects. The EL2 defect which is one of the As-antisite defects can be reliably recognized with its characteristic MCDA as well.

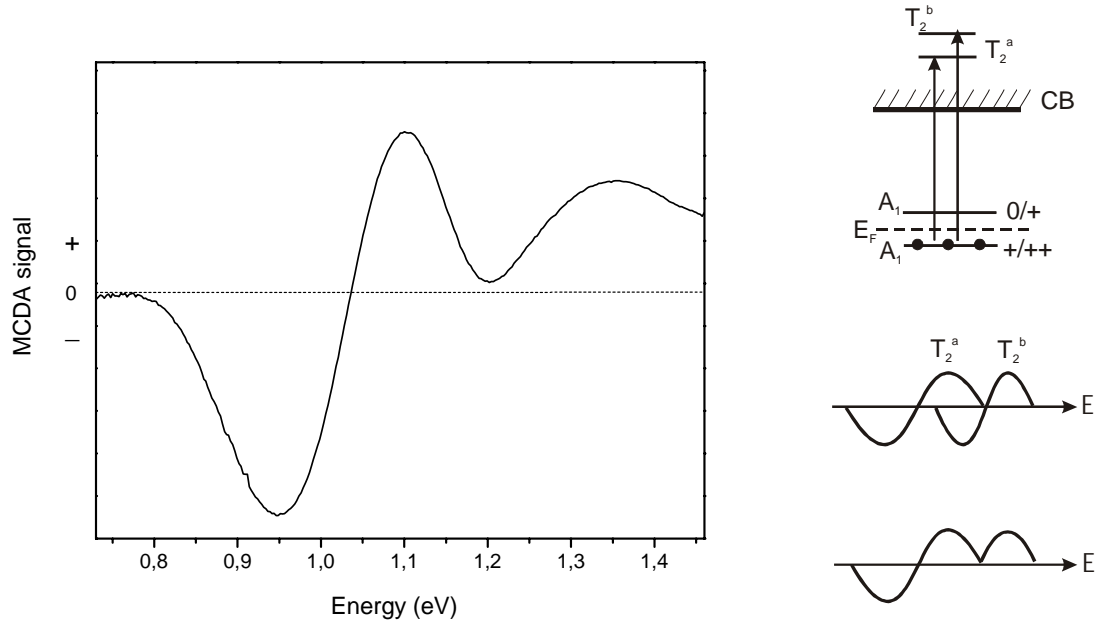


Fig. 3.2 Characteristic MCDA spectrum of the EL2 defect in semi-insulating GaAs measured at low temperature (1.5K) and the internal excited state model of the correspondent optical transitions. The measurements of the EL2-MCDA was performed at $B_0=2000\text{mT}$.

3.2.3 MCDA-EPR: The EL2 defect is formally a double donor which is paramagnetic only in its singly ionized state EL2^+ . The EPR signal which has been identified with this defect was observed for the first time in Bridgman-grown GaAs: Cr [Wagner 1980]. The spectrum with the same parameters was later observed with a conventional EPR spectrometer working at 9 GHz (X-band) [Wörner 1981; Weber and Schneider 1982; Elliot 1984] and with MCDA-EPR at K-band frequencies (~ 24 GHz) [Meyer 1984]. It has been evidently shown that these spectra of the EL2 arise from the antisite defect with an As atom on a Ga site. This identification was confirmed by comparison, with appropriate scaling, of the hyperfine interaction parameter A with that for the phosphorus antisite P_{Ga} in GaP, where superhyperfine interaction with ligands is resolved allowing unambiguously the identification of the defect [Wagner 1980].

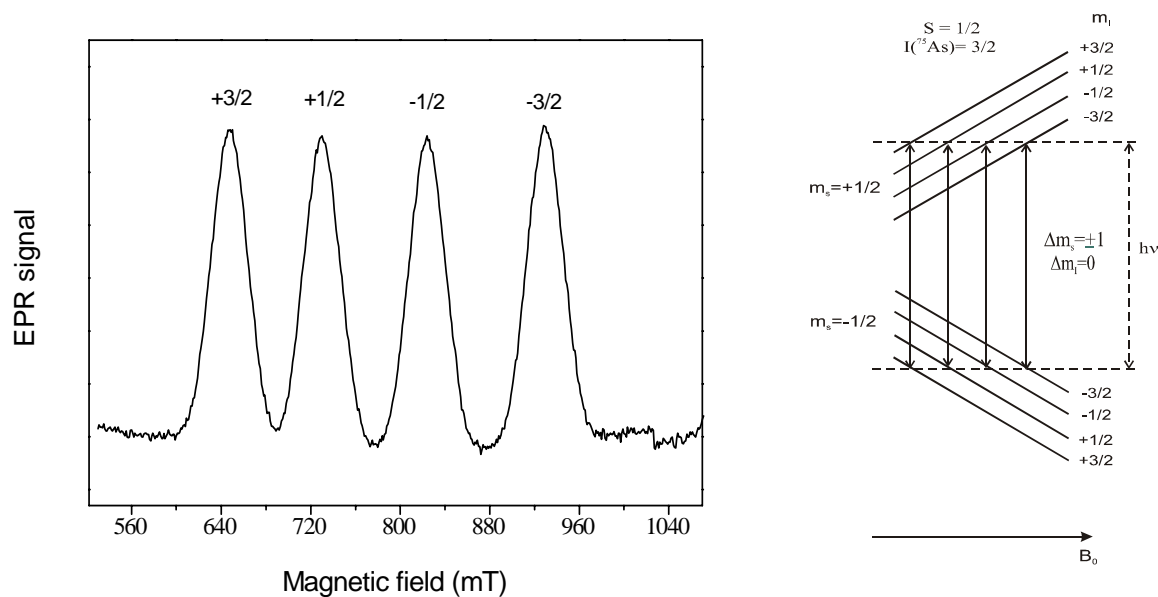


Fig. 3.3 K-band MCDA-EPR spectrum of the EL2⁺ defect and schematic representation of the correspondent EPR transitions for the $S = 1/2$, $I = 3/2$ system. The spectrum was measured in semi-insulating as-grown LEC GaAs at temperature of $T = 1.5$ K and microwave frequency $f = 24.8$ GHz. Photon energy was set to 0.92 eV. Microwave power less than $5\mu\text{W}$.

The K-band MCDA-EPR spectrum of the EL2⁺ is shown in figure 3.3. It can be described by the spin Hamiltonian

$$H = g\mu_B \vec{B}_0 \vec{S} + A \vec{I} \vec{S} \quad (3.1)$$

where the first term represents the electronic Zeeman effect and the second the hyperfine interaction. The EPR is characterized by an isotropic g -factor $g = 2.04$ and the central hyperfine coupling constant $A = 2656$ MHz, which is also within experimental error isotropic. The angular dependence of the MCDA-EPR measured at high fields correspondent to W-band microwave frequencies confirms the high isotropy of g -value and hf constant (see fig. 3.4). The hyperfine interaction is responsible for the four line pattern. It arises from the Fermi contact interaction of the unpaired electron spin $S = 1/2$

with the central ^{75}As nucleus (nuclear spin $I = 3/2$, 100 % natural abundance) and is proportional to the electron spin density at this nucleus.

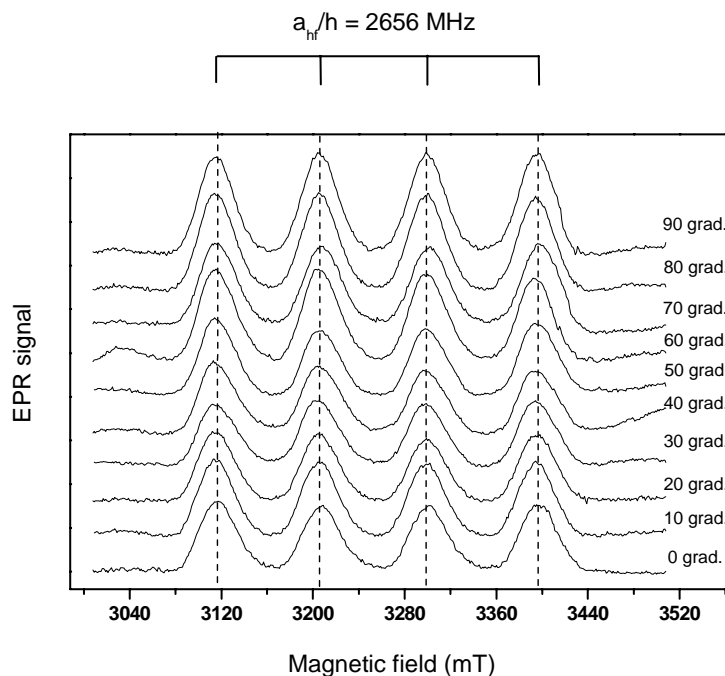


Fig. 3.4 Angular dependence of the MCDA-EPR line widths of the EL2 defect in semi-insulating GaAs measured in W-band for rotation of the magnetic field in the (011) plane. 0° corresponds to $B \parallel [110]$ and 90° to $B \parallel [001]$.

Unfortunately, the large EPR line widths of the different As-antisite related defects which can be created by different treatments and growth conditions of the GaAs does not allow to distinguish these defects taking into account only their EPR spectra which are almost identical. In this case their characteristic MCDA (especially the tagged by EPR and ENDOR MCDA) spectra are more sensitive.

Another possibility to identify the defect with the MCDA-EPR method is to measure its characteristic spin-lattice relaxation time (T_{1e}). With this method T_{1e} can be measured in a rather simple way. One drives the ground state polarization P from thermal equilibrium by applying a microwave pulse and monitors the recovery of the microwave-induced decrease of the MCDA as a function of time. T_{1e} as short as 10-100 μs may be measured with this method. The MCDA depends only on the longitudinal magnetization, and

therefore, only on T_{1e} [Spaeth 1992]. It is known that for the EL2 defect in semi-insulating GaAs the characteristic time of such a relaxation is near 4 seconds at fields corresponding to K-band microwave frequencies (600-900mT) and 1.5 K. The high field measurements of T_{1e} (3050-3400 mT) yield a value close to 2 seconds (see fig.3.5).

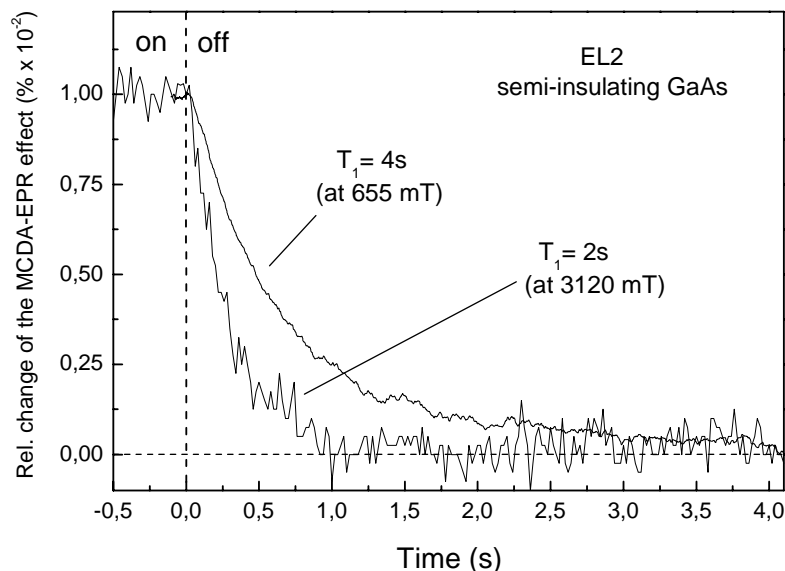


Fig. 3.5 Spin-lattice relaxation time T_{1e} of the EL2 defect in SI GaAs measured at different magnetic fields with the MCDA-EPR method (at 655 mT – K-band; at 3120 mT – W-band EPR spectra) at 1.5 K.

3.3 Advantage of high-field EPR and ENDOR of the EL2 defect

If a neighbour shell with N nuclei has a large superhyperfine (shf) interaction as in the case of the EL2 defect (~ 180 MHz for the first shell), there are additional splittings of the ENDOR lines which can not be described with the effective spin approximation and, therefore, complicate the analysis of the spectra. These splittings are caused by an indirect interaction of the nuclear spins via the electron spin. In this coupling mechanism the interaction of the electron spin with one neighbour nucleus modifies the electron spin

states, and these modified spin states have a noticeable effect on the interaction with a different neighbour nucleus. The shf interaction of the electron spin with a nuclear spin is therefore dependent on the spin quantizations of the other $N-1$ nuclei. This effect is called the “second order hf structure” or “the pseudo-dipolar nuclear coupling”. Due to this effect each line is split into at most $(2I+1)^{N-1}$ lines. This effect is large if two or more neighbour nuclei are magnetically equivalent, i.e. have the same principal values and direction cosines of the principal axes of the interaction tensors. This can be the case for all directions or only for some special magnetic field orientations of the magnetic field. For the determination of the defect model these line splittings are not desirable because it is difficult to determine whether the observed line splitting occurs due to this effect or to a low symmetry of the defect. Thus the analysis of the ENDOR spectra is complicated.

In an approximation without consideration of the quadrupole interaction the problem of several equivalent nuclear spins can be reduced to the problem of the interaction of electron spin with one nucleus having the total nuclear spin I_g . The total nuclear spin I_g results from the adding of the single nuclear spins. The ENDOR transitions are allowed only within of the possible I_g -multiplets [Seidel 1966]. In this case without the quadrupole interaction many transitions coincide. In perturbation theory of second order for the isotropic shf interaction the ENDOR frequencies are given with a ratio:

$$h\nu^\pm = a/2 \pm W_{split} (m_q + 1/2) \mp \mu_n g_I B_0 \quad (3.2)$$

with

$$W_{split} = \frac{a^2}{2\mu_B g_e B_0} \quad (3.3)$$

here W_{split} is the energy of the pseudo-nuclear coupling.

In the second order approximation the magnitude of the splitting is proportional to the square of the shf energy divided by the field-dependent electron Zeeman energy. A simple calculation of the pseudo-nuclear splitting for ENDOR lines with the isotropic hyperfine constant $a/h = 200$ MHz yields to $W_{split} \sim 1$ MHz if the line was measured at the field of $B_0 = 700$ mT corresponding to K-band while for a magnetic field of $B_0 = 3080$ mT (W-

band) $W_{split} \sim 0.2$ MHz. Clearly, to eliminate such undesirable splittings caused by the nuclear-nuclear interaction, ENDOR measurements must be performed at magnetic fields large enough to reduce W_{split} .

Another difficulty in the ENDOR analysis is caused by the fact that in systems with strong hf, shf and quadrupole interactions, which are characteristic for the EL2 defect, the nuclear spin states are strongly mixed such that normally forbidden transitions (e.g. $|\Delta m_I| > 1$) are allowed. These transitions can be predicted in the ENDOR simulations but they complicate the experimental spectra. The analysis of the problem in the case of the large shf interaction shows that interactions of the order of 200 MHz, typical for the first As shell, suffice to create singly forbidden ($\Delta m_S = 0$; $\Delta m_I = \pm 2$) transition probabilities large enough to observe them in the MCDA-ENDOR with high RF powers. According to time-dependent perturbation theory of second order their intensity must be smaller than the intensity of the allowed transitions by a factor $\sim (g\mu_B B_0/A)^2$. Therefore, with the increase of the magnetic field the forbidden transitions should vanish.

Figure 3.6 (a,b) shows the ENDOR spectra of the EL2 defect measured in K- and W-bands, respectively, for field orientation $B_0 \parallel [110] + 4^\circ$ in the (001) rotation plane. The lines in both spectra belong to the four ^{75}As nuclei of the first neighbour shell (see figures 3.8; 3.10). Their line widths are about 1 MHz. In low field spectra (K-band) lines of two m_S states occur while in high-field ENDOR(W-band) only the lines belonging to $m_S = -1/2$ were observed. The result that only “-“ frequencies (so-called “sum frequencies”) were detected at high fields was unexpected but helpful, since the simultaneous observation of the lines belonging to two m_S states does not give much new information and, therefore, is more often a nuisance than a help. The physical reason of such an effect lies in complicated dynamics and relaxation transitions of the MCDA-ENDOR where the level occupations of different m_S states are determined by many parameters, i.e. temperature of the measurement, strength of the static magnetic field, frequencies and strengths of the oscillating (microwave and RF) fields.

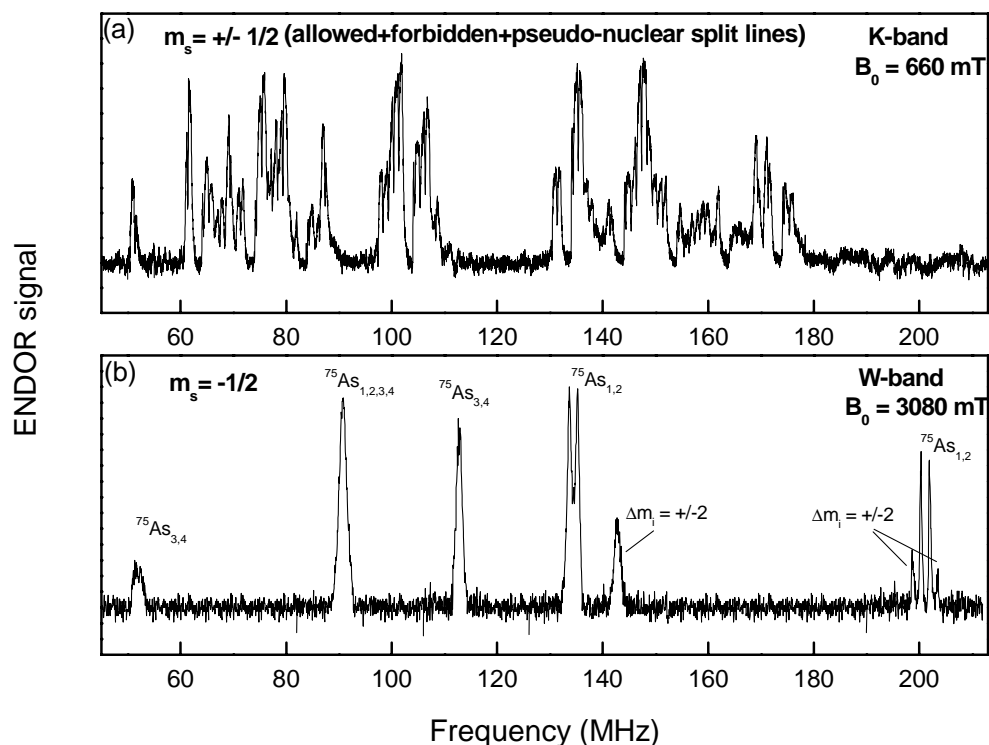


Fig. 3.6 MCDA-ENDOR spectra of the EL2 defect measured in K- and W-bands ((a) and (b), respectively) for $B_0 \parallel [110] + 4^\circ$ (4° in a (001) plane). The magnetic fields are 660 mT (K-band) and 3080 mT (W-band), the temperature was $T = 1.5$ K. The high field spectrum (W-band) does not show pseudo-nuclear couplings. For the low field (K-band) ENDOR there are strong additional splittings of the lines because of the pseudo-nuclear coupling between the 4 nearest ^{75}As neighbours.

When comparing both spectra one can notice a large difference between them. Because of the elimination of the pseudo-nuclear splitting and the observation of only “sum” frequency lines the spectra measured in W-band are much simpler and easier to identify. The analysis of such spectra is a relatively easy task and brings clear and reliable results. That does not hold for K-band spectra where the “second order” splitting, simultaneous observation of the lines belonging to both m_s states and the high probability of the forbidden transitions drastically complicate the spectrum making the analysis difficult. For some directions many ENDOR lines are not resolved in K-band spectra.

For the same reason when diminishing the higher order effects, which cause also forbidden transitions in the EPR spectra ($\Delta m_S = \pm 1$, $|\Delta m_I| > 0$), the advantages of the high field measurements hold also for the EPR spectra. The high field detection allows much simpler analysis of the experimental EPR spectra in comparison with those measured at low fields. It is important in the case when the EPR line width has to be simulated and analyzed in order to check the defect model derived from ENDOR. Such simulation for low field EPR (X- or K-band) must be performed with the exact diagonalisation of the appropriate spin-Hamiltonian to take into account all possible transitions with their transition probabilities. That requires the treatment of prohibitive large spin matrices. For an As-antisite in GaAs a matrix of the dimension 2048x2048 is obtained for the central nucleus with its four nearest As neighbours ($S=1/2$, $I=3/2$, $N=5$). The complete diagonalisation of such a matrix is possible in principle, however, the time needed for this using a PC amounts to several weeks. That prevents satisfactory simulations [Wirbeleit and Niklas 1997].

Figure 3.7 shows the typical four-line hf-split MCDA-EPR spectra of the EL2 defect in SI GaAs measured for $B_0 \parallel [001]$ in K-band (a) and W-band (b), respectively. The spectra were monitored with the magnetic circular dichroism of the absorption (MCDA) at 1.5 K in the MCDA band centered at 0.94 eV. The observed hf splitting occurs due to the central ^{75}As nucleus of the antisite ($I = 3/2$, 100 % natural abundance) and is described by an isotropic hf constant of (2656 ± 30) MHz in agreement with the previously determined one from K-band. However, the four hf lines measured in W-band are equidistant (93 mT separation) in contrast to the K-band spectra where the hf line separation increases towards higher magnetic field.

The off-diagonal terms in the spin-Hamiltonian, which cause that non-equidistance of the hyperfine lines as well as appearance of the forbidden EPR transitions, vary as $(g\mu_B B_0)^{-1}$ and thus are strongly reduced at high (W-band) magnetic fields. The equidistance of the hf-split lines indicates that the Zeeman interaction is much stronger than the hf interaction of the central ^{75}As nucleus (and shf interaction with ligands). Therefore, the high-field EPR spectra can be described by first order perturbation calculations of the spin Hamiltonian, thus allowing a much simpler analysis compared to X- or K-band.

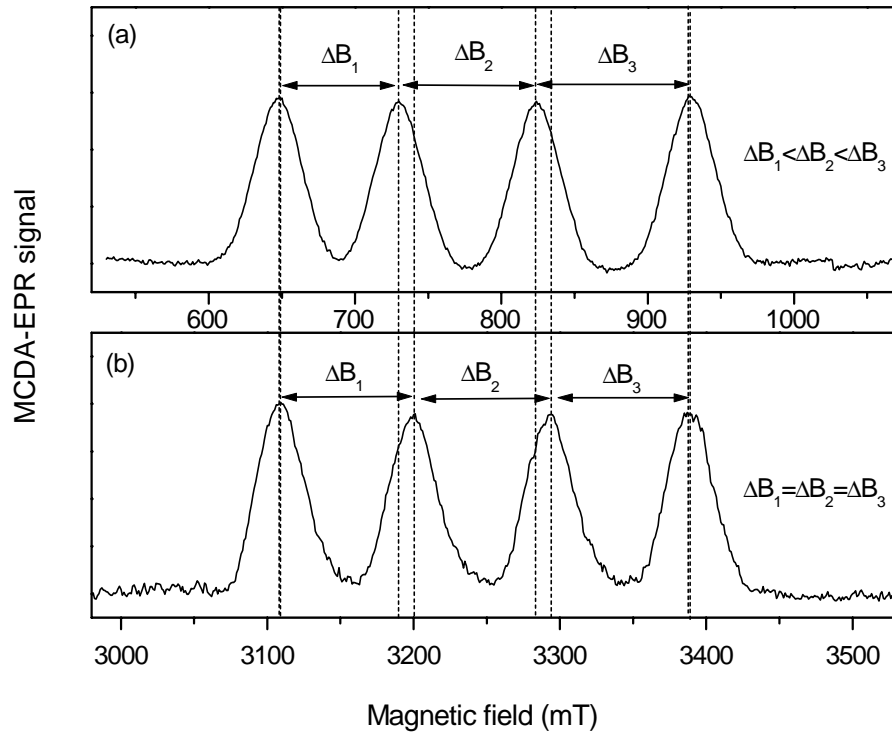


Fig. 3.7 MCDA-EPR spectra of the EL2 defect in SI GaAs measured at $T=1.5$ K in (a) K-band (24.8 GHz) and (b) W-band (93 GHz) for $B_0 \parallel [001]$. The hyperfine split lines are equidistant ($\Delta B_1 = \Delta B_2 = \Delta B_3 = 93$ mT) in the W-band spectra while measuring the EPR in K-band one observes the strong influence of the hyperfine interaction reflected in the non-equidistance of the hf lines.

In the MCDA-ENDOR experiments however, forbidden transitions ($\Delta m_s = \pm 0$, $|\Delta m_l| > 1$) still appear in W-band MCDA-ENDOR spectra with relative large intensities. This effect has probably a technical reason. For the detection of ENDOR with the Fabry-Pérot cavity relatively large samples (in comparison with the short wavelength of the W-band microwave field) were used. That is preferable for the MCDA detection of the EPR/ENDOR signals because of the larger optical density of the samples and higher S/N ratio of the spectra. However, with such detection the external magnetic field B_0 and the oscillating microwave B_1 and RF B_2 fields are not always in exact orthogonal configuration. This must cause the high probability of the forbidden transitions. This

effect is not pronounced if a cylindrical cavity is used, where much smaller samples are under investigation and the mentioned orthogonality can be fulfilled more easily. Unfortunately, the attempts to detect MCDA-ENDOR with the W-band (TE_{011}) cylindrical cavity were not successful. Only EPR spectra could be measured with it.

3.4 W-band MCDA-ENDOR of the EL2 defect in GaAs

3.4.1 The first neighbour shell of the As antisite

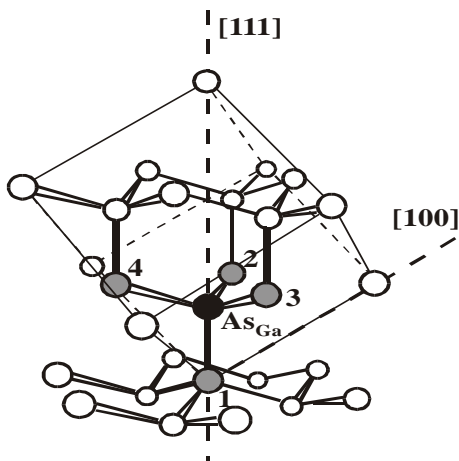


Fig. 3.8 As-antisite defect and its nearest neighbours (four ^{75}As nuclei).

As the first step in the ENDOR spectra analysis the chemical nature of the nuclei (lines) must be identified. For this purpose one has to investigate the frequency shift of the ENDOR lines varying the external magnetic field. With the approximation of the first order perturbation theory for a system with

$S=1/2$ in case when $\mu_n g_I B_0 < \frac{1}{2} W_{shf}$ the change of the line position with the magnetic field is:

$$\Delta f = \pm g_I \mu_n \Delta B_0 / h \quad (3.4)$$

It is seen that the ENDOR frequency shifts with the variation of the external magnetic field B_0 proportionally to the nuclear g -factor g_I . This ratio often allows the determination of the nuclear g -value and therefore an identification of the chemical nature of the ENDOR lines. Thus for ^{75}As nucleus with $g_I = 0.959647$ the shift should be near

0.73 MHz per 100 mT while for two Ga isotopes (^{69}Ga with $g_I = 1.34439$ and ^{71}Ga with $g_I = 1.70818$) we obtain shifts of 1.025 MHz and 1.3 MHz per 100 mT, correspondingly. In general, the shift of the MCDA-ENDOR lines is not a straight line through the total magnetic field range but consists of the line portions for each m_I -state of the central nucleus, which are displaced from each other.

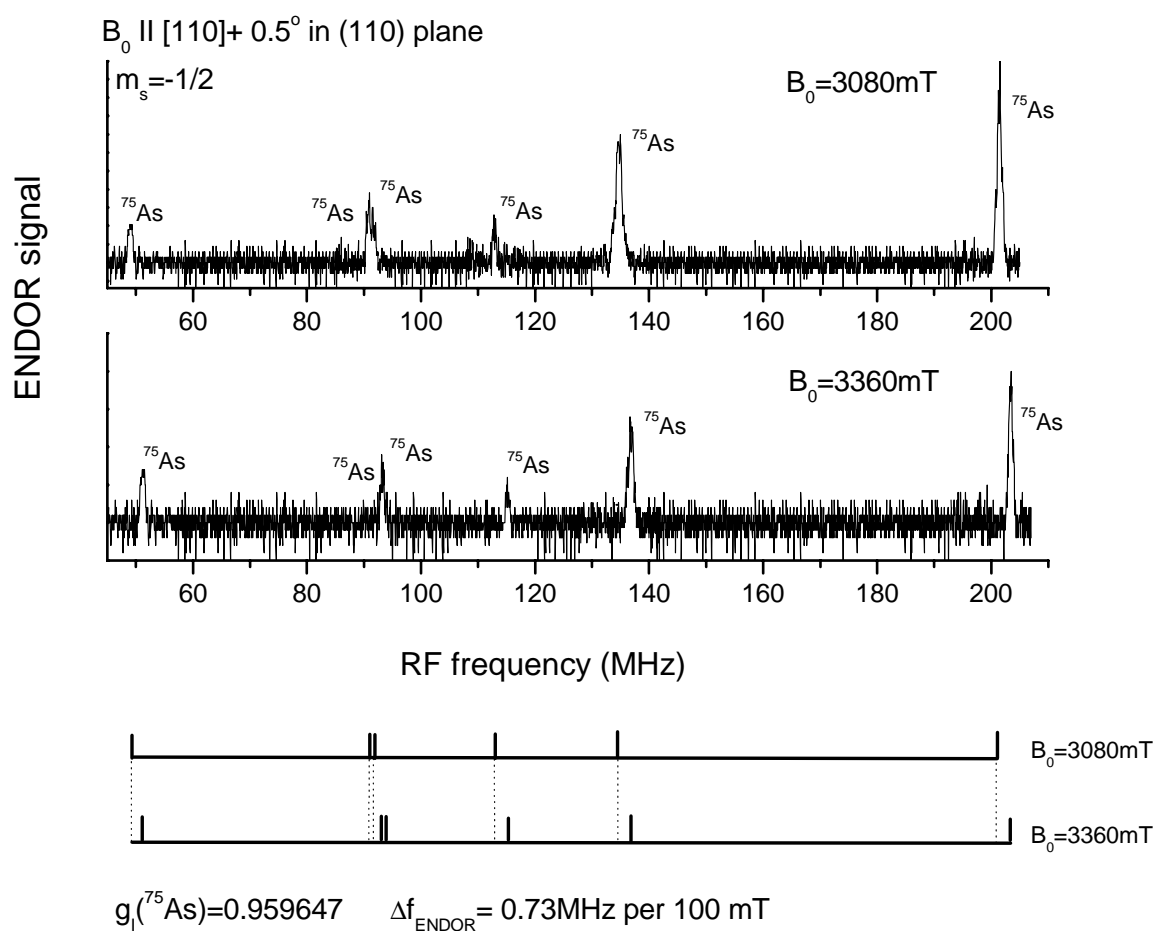


Fig. 3.9 Example for the identification of interacting nuclei due to the magnetic field shift of their ENDOR lines. The observed shift of $\sim 0.73\text{MHz}$ per 100mT (equal for all lines) yields a nuclear g -factor of 0.96 which represents a ^{75}As nucleus. The estimated constants of the interactions (a/h order of 150MHz) correspond to expected superhyperfine interactions with the nearest ^{75}As ligands (see fig.3.8). All lines shift to higher frequencies with the increase of the magnetic field, therefore they belong to $m_S = -1/2$ state.

Since the resonance conditions for the EPR transition must be fulfilled to measure MCDA-ENDOR, the magnetic field must be varied within the width of the EPR lines. Because of their large width, these magnetic-field-shift experiments can be performed in a broad field range (3060-3360 mT). Such measurements of the ENDOR for different fields show that all lines detected with the W-band ENDOR in the frequency range 40 MHz to 220 MHz belong to ^{75}As nuclei, which make up the first neighbour shell ($d=2.44 \text{ \AA}$) of the As antisite (see figures 3.8, 3.9).

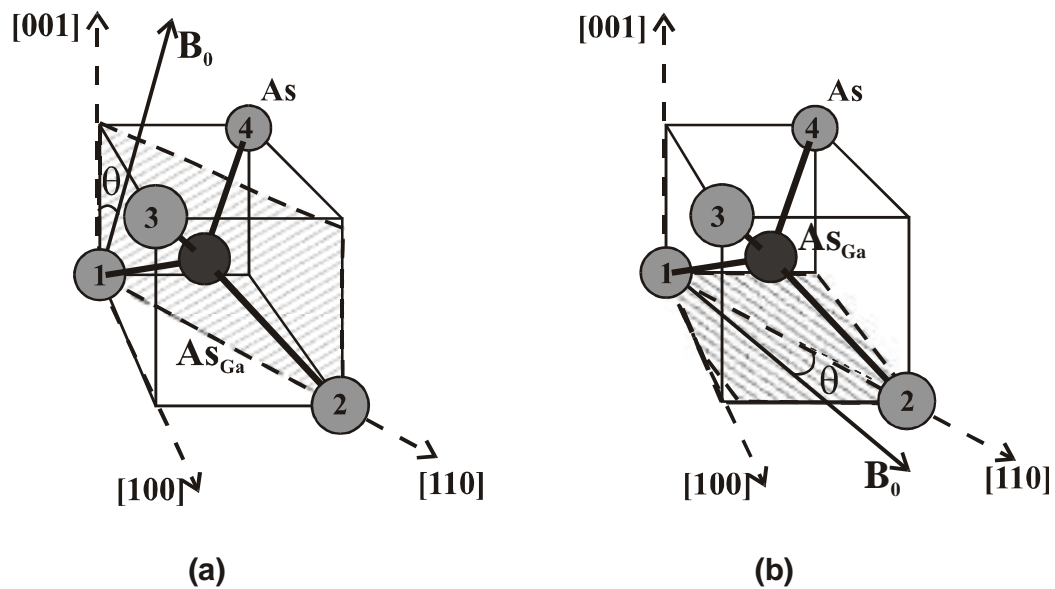


Fig. 3.10 Model of the As antisite defect with its four tetrahedrally (T_d) coordinated ^{75}As neighbours and the crystal orientations with respect to the magnetic field. The neighbour nuclei are numbered (1-4) and the numbers were held in the analysis. Two rotation planes (110) and (001) (figures (a) and (b) respectively) are shown. The rotation angle 0° corresponds to: $B_0 \parallel [001]$ direction in the (110) rotation plane and $B_0 \parallel [110]$ in the (001) rotation plane.

The assignment of the lines can be attempted with the estimation of the interaction parameters and their orientations for the ligand nuclei. It is often useful to consider the simple solution of the eigenvalue problem in the first order perturbation theory. In that

approximation one has for the ENDOR frequencies with the selection rules of allowed transitions $\Delta m_S = 0$ and $\Delta m_I = \pm 1$: [Seidel 1966]

$$\nu_{ENDOR} = \frac{1}{h} \left| -\mu_n g_I B_0 + m_S W_{shf} + m_q W_q \right| \quad (3.5)$$

with

$$W_{shf} = a + b(3 \cos^2 \theta - 1) + b' \sin^2 \theta \cos(2\delta) \quad (3.6)$$

$$W_q = 3q(3 \cos^2 \theta' - 1) + q' \sin^2 \theta' \cos(2\delta') \quad (3.7)$$

$$m_q = \frac{m_I + m_I'}{2} \quad (3.8)$$

where m_q is the arithmetic average of the two magnetic nuclear spin quantum numbers of the levels between which the ENDOR transition occurs. W_{shf} is the energy of the shf interaction with ligand nuclei and is given in terms of the isotropic shf constant a , the anisotropic shf interaction constants b and b' . b' is related to the deviation of the shf tensor from axial symmetry. For the quadrupole interaction the parameters q and q' are used. The angles θ and θ' are the angles between the direction of the static magnetic field B_0 and the z-axis of the ligand superhyperfine (shf) and quadrupole tensors, respectively, while δ and δ' are the angles between the rotation plane of the magnetic field and the x-axis of the corresponding tensor principal axis system.

From equation (3.5) one can see that for the system of the electron spin ($S=1/2$) and the nuclear spin $I=3/2$, what corresponds to the interaction of the unpaired electron with one neighbour nucleus, 3 ENDOR lines for each m_S ($m_S = \pm 1/2$) state would be expected. Here the quadrupole interaction splits the single shf-line into three lines with the quadrupole quantum numbers $m_q = -1, 0, 1$. If the number of the interacting nuclei with the same nuclear spin extends to 4, one expects already 12 lines for each m_S state (in total 24 lines). This is the case when all 4 nuclei are non-equivalent. This happens when the tensor orientations with respect to the magnetic field or their principal values are different.

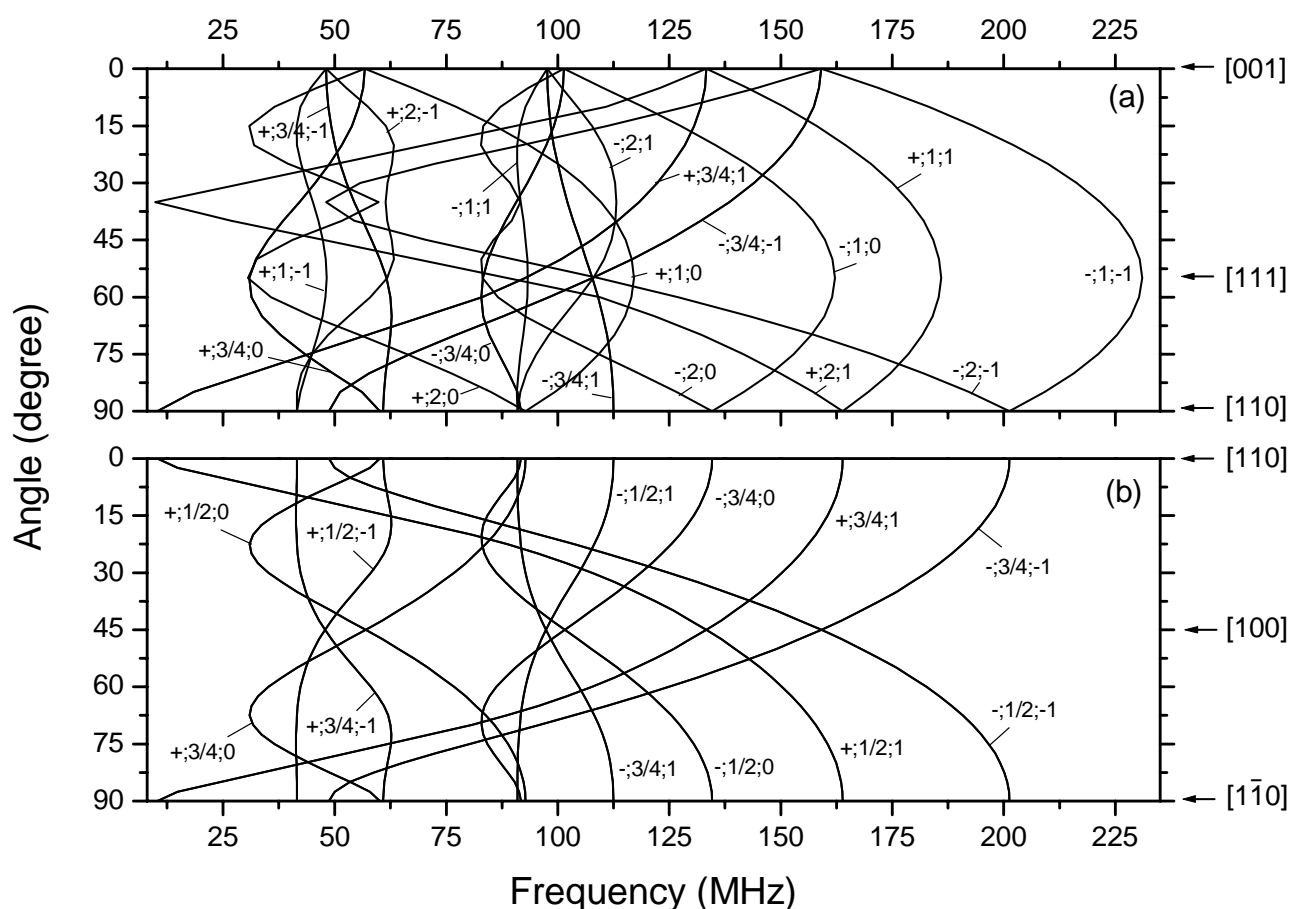


Fig. 3.11 Simulations of the ENDOR angular dependence for the first ^{75}As neighbour shell of the EL2 defect rotating the external magnetic field B_0 ($B_0=3080\text{mT}$) in planes (a)-(110) and (b)-(001). The simulations were made with the full diagonalisation of the spin-Hamiltonian using the program “Visual ENDOR” (Version 2.60, V.Grachev). The constants of the interaction tensors are: $a/h=170.5\text{MHz}$; $b/h=54.3\text{MHz}$; $q/h=11.5\text{MHz}$; $\theta_b=0$; $\theta_q=0$. In the simulations the high (T_d) symmetry of the defect was assumed.

For a precise determination of the symmetry and the interaction parameters of the As ligands, in particular the non-isotropic parts b and q , the ENDOR spectra must be measured as a function of the crystal orientation with respect to the static magnetic field B_0 . To understand the experimental ENDOR spectra one fits the measured ENDOR angular dependencies with the simulated ones, which were made with the assumption of a possible defect model. The simulations must be performed with the full diagonalisation of

the appropriate spin-Hamiltonian. Then the simulated angular dependencies are compared with the measured ones. An agreement is achieved only for the correct defect model.

Now we discuss, what kind of ENDOR spectra and angular dependencies are expected for the nearest neighbours if the isolated As-antisite model for the EL2 defect is assumed. Here all 4 nearest Arsenic nuclei belong to one “shell”. It means that they have the same distance from the antisite and can be transformed into each other by symmetry operations of the crystal. The interaction tensors \hat{A} and \hat{Q} (see eqn.1.13-1.16; 1.18) are symmetric second rank tensors. Thus, there exist at most six independent interaction parameters for each tensor. In the principal axis system there are three principal values and three Euler angles Θ, Ψ and Φ to describe the orientation of the principal axis system in the crystal. Each nucleus has its own principal axis system for its interaction tensors. The tensor orientation in the crystal is often determined by symmetry. If the defect center and the respective nucleus are in a mirror plane of the defect, then two principal axes must be in the mirror plane. If the connecting line between the neighbouring nucleus and the center is a threefold or higher symmetry axis, then the tensor is axially symmetric with its axis in the symmetry axis. For the nearest neighbours of the isolated As antisite one expects that the parameters b' and q' are zero and that there is no free Euler angle, since the $\langle 111 \rangle$ directions are threefold symmetry axes.

For the EL2 defect the angular dependencies of the high-field W-band ENDOR spectra in frequency range from 40 to 300 MHz (with forbidden transitions) for the two rotation planes (110) and (001) were measured and analyzed. In Figure 3.10(a, b) the corresponding rotation planes are shown for the tetrahedrally coordinated (isolated) defect model. The neighbour ^{75}As nuclei are numbered and these numbers were held in the analysis. It seen that in the high symmetry configuration the nuclei 3,4 are magnetically equivalent when rotating the crystal in the (110) plane (Fig.3.10 (a)). In the (001) rotation plane (Fig.3.10(b)) there are two pairs of the equivalent nuclei (1,2 and 3,4). Therefore, their ENDOR lines must coincide.

The expected angular dependencies of the ENDOR lines of the four nearest ^{75}As neighbours of the isolated As antisite (T_d symmetry) for two rotation planes (110) and (001) are illustrated in figure 3.11 (a) and (b), respectively. The simulations were

performed with the full diagonalization of the spin-Hamiltonian using the program “Visual ENDOR” (Version 2.60, V.Grachev, 1999). The interaction parameters taken for the simulation are $a/h=170.5$ MHz, $b/h=54.3$ MHz, $q/h=11.5$ MHz with θ_b and $\theta_q=0$. The marks near lines in the figure describe the spin state m_S ($m_S = +1/2$ or $-1/2$), the position of the nucleus (nuclei 1-4 in figure 3.10), and the quadrupole quantum numbers m_q ($m_q = -1; 0; 1$). The curvature of the angular dependence is determined by the large quadrupole interaction. The anisotropic interaction vanishes for $B_0 \parallel [100]$. The central nucleus of the defect was not included assuming that at high magnetic fields ($B_0 = 3080$ mT) the quantization axis of the electron spin is not noticeably modified by the isotropic hyperfine interaction of the central nucleus. Here we see clearly the advantage of the high-field ENDOR where the interaction constants for the ligands can be determined more precisely. The lines of the two m_S states are shown in the figure 3.11. In the fitting of the measured spectra only “sum frequencies” ($m_S = -1/2$) were taken into account because only those lines were observed experimentally. This fact simplified the ENDOR spectra analysis.

For the non-disturbed isolated As antisite, when all 4 nuclei are in the high symmetrical tetrahedral (T_d) configuration and the electron spin density is equally distributed, their interaction constants are equal. The tensors are directed along $\langle 111 \rangle$ towards the center of the defect. In this case, as it was mentioned above, there are orientations which make the interacting nuclei magnetically equivalent, therefore their ENDOR frequencies must coincide. The number of the expected ENDOR lines decreases. For example (see Fig. 3.11), for each orientation of B_0 in a (001) plane different from $\langle 100 \rangle$ one expects in total 12 ENDOR lines for $m_S = \pm 1/2$. Here the 1,2 nuclei and 3,4 nuclei remain pair wise equivalent. If the rotation is in the (110) plane from $[001]=0^\circ$ towards $[110]=90^\circ$ in total 18 lines must arise for all angles different from 0 and 90 (here nuclei 3,4 are equivalent). If the field is oriented parallel to $\langle 100 \rangle$ the tensors of all 4 nuclei are equally oriented with respect to B_0 , therefore one observes only 6 ENDOR lines (3 for each m_S).

In figure 3.12 the angular dependence of the MCDA-ENDOR lines (dots) measured on LEC GaAs:V setting the external magnetic field $B_0 = 3080$ mT upon rotating the crystal in (001) plane from $[110]=0^\circ$ towards $[1\bar{1}0] = 90^\circ$ is shown. The dots represent the experimental ENDOR line positions. The solid lines describe the simulated ENDOR angular dependence, for the high symmetrical (T_d) As antisite with the interaction parameters $a/h = 170.8$ MHz, $b/h = 54.6$ MHz, $q/h = 11.5$ MHz, $\theta_b = 0$, $\theta_q = 0$. The simulated lines for $m_S = -1/2$ are shown. Dashed lines are the simulated forbidden ENDOR transitions ($\Delta m_S = 0$; $|\Delta m_I| > 1$).

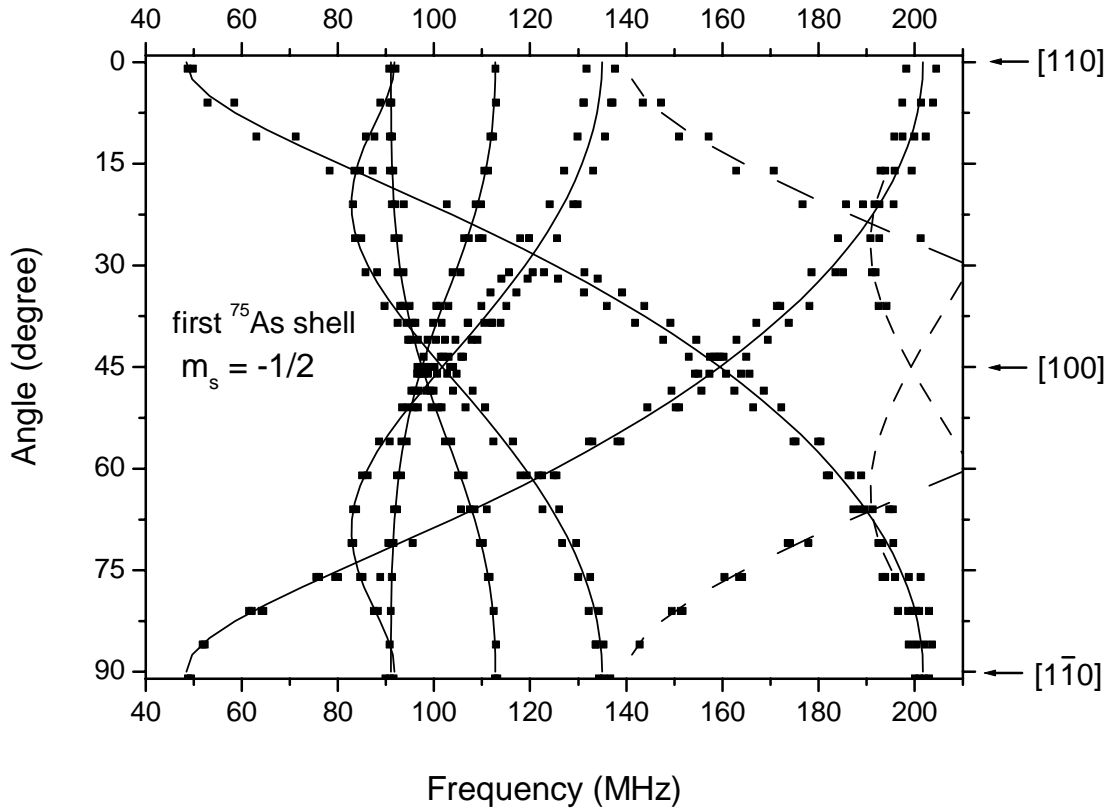


Fig. 3.12 The measured (dots) W-band ODENDOR angular dependence of the EL2 defect performed at $B_0 = 3080$ mT rotating the crystal in the (001) plane from $B_0 \parallel [110] = 0^\circ$ towards $B_0 \parallel [1\bar{1}0] = 90^\circ$. The lines (solid and dashed) represent the simulated spectra calculated with the assumption of T_d symmetry for the first ^{75}As neighbours. Solid lines show the simulated allowed transitions ($\Delta m_S = 0$, $\Delta m_I = \pm 1$) while the dashed lines are forbidden transitions ($\Delta m_S = 0$, $|\Delta m_I| > 1$). Only lines of $m_S = -1/2$ state are shown because only those lines were detected experimentally.

ENDOR lines in the frequency range from 49 to 210 MHz were detected. The shift of the lines with the magnetic field shows that all belong to ^{75}As nuclei. The experiment shows that lines due to forbidden transitions still appear in W-band ENDOR spectra. Their intensity is unexpectedly large. These transitions arising at higher frequencies can easily be identified with the full diagonalisation. Also by adding the frequencies of the allowed transitions which in sum make up the corresponding forbidden transitions and by taking into account the different quadrupole quantum numbers m_q for lines with $|\Delta m_l| > 1$ one can roughly identify these lines.

There is almost agreement between the calculated angular dependence and the experimental lines indicating that the superhyperfine tensors must have almost $\langle 111 \rangle$ symmetry as required in the T_d model. However there are many lines splittings not explained by the T_d symmetry. This can have two reasons:

- (1) The nearest neighbours are not precisely tetrahedrally coordinated. Then there could be up to four different shf and quadrupole tensors and one would have the superposition of up to four centre orientations.
- (2) The crystal was not exactly orientated in the (001) plane. Then nuclei 1 and 2 as well as 3 and 4 (see fig. 3.10) lose their equivalence.

The calculated ENDOR angular dependence of the tetrahedrally coordinated As antisite describes the experimentally observed angular dependence if one takes into account the deviation of the measured plane from the simulated one. That happens with the tilt of the crystal which, sometimes, is not noticeable with the naked eye. In figure 3.13 such a simulation ($m_S = -1/2$) for the (001) rotation plane is presented. With the small tilt of the rotation plane (tilt angles $\eta = 1.65^\circ$ and $\zeta = 1.1^\circ$) the measured and simulated lines can be fitted with the maximum deviation of less than 0.26 MHz. The angles η and ζ have here the following meaning: η is the angle between the Z axis of the principal system (X,Y,Z) and the Z' of the system (X',Y',Z') fixed to the host crystal which results with the rotation of the Z axis of the (X,Y,Z) towards its X axis around Y; ζ is the angle of the crystal rotation in the new (X'Y') plane (see for reference fig. 3.14).

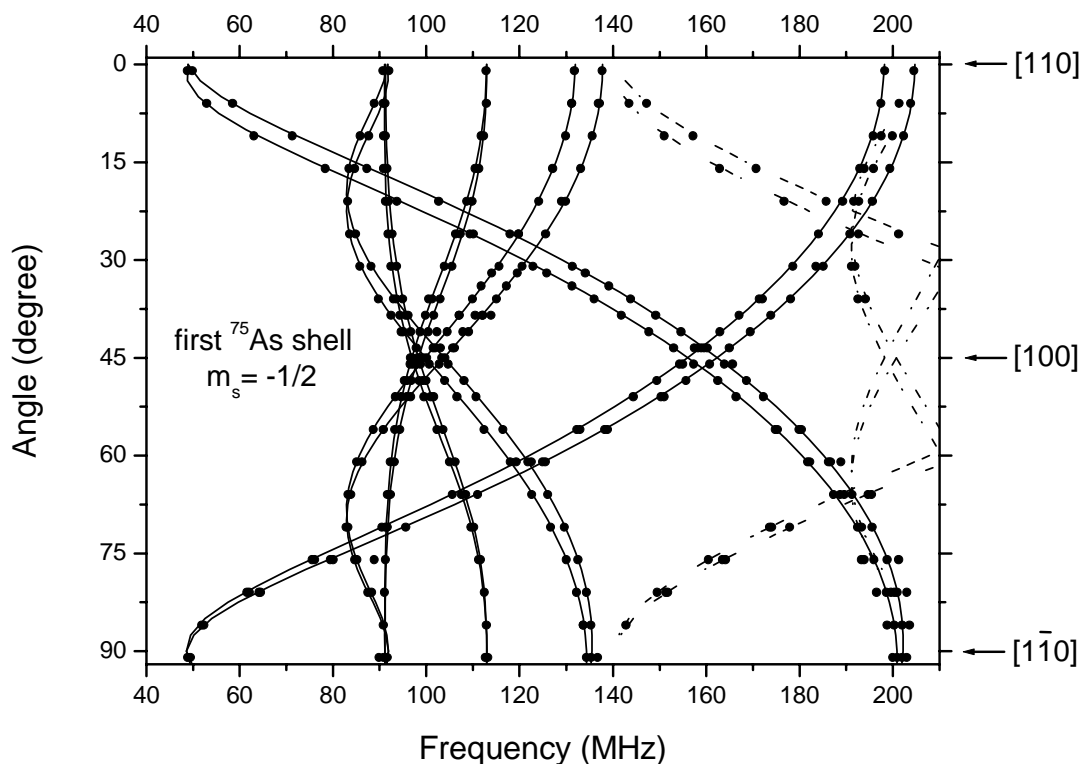


Fig. 3.13 The fitting of the experimental (dots) ODENDOR frequencies and the simulated ones (lines) assuming the tetrahedral symmetry of the first ^{75}As shell taking into account a tilt of the crystal (angles $\eta=1.65^\circ$ and $\zeta=1.1^\circ$ degree - see for ref. fig. 3.14) $B_0=3080$ mT. (001) rotation plane from $B_0 \parallel [110]=0^\circ$ towards $B_0 \parallel [1\bar{1}0]=90^\circ$. Solid lines show the allowed ENDOR transitions, the dashed lines are the forbidden ones. Electron spin state is $m_S=-1/2$.

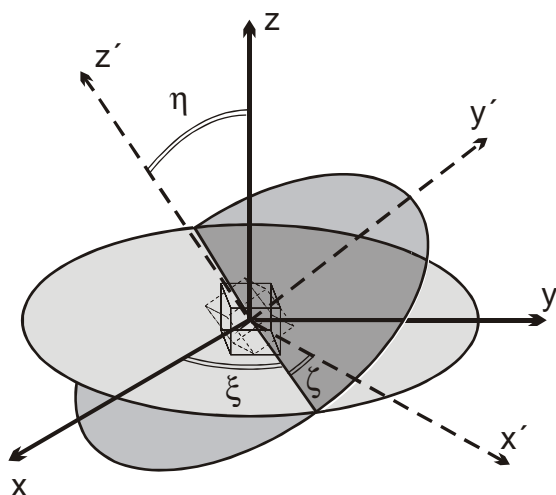


Fig. 3.14 Angle assignments in the ENDOR spectra simulations of the tilted crystal. (“Visual ENDOR” Version 2.60, V.Grachev)

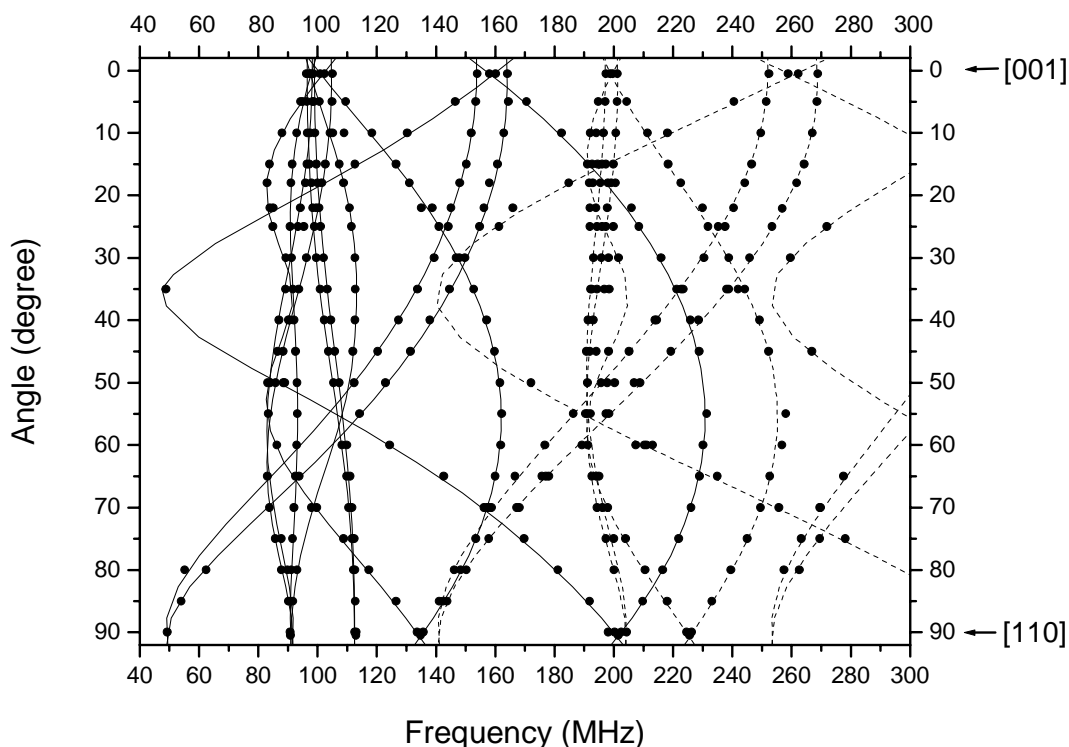


Fig. 3.15 The measured (dots) and simulated (solid and dashed lines) W-band ODENDOR angular dependence of the EL2 defect. The measurements were performed at $B_0 = 3080$ mT rotating the crystal in (110) plane from $B_0 \parallel [001] = 0^\circ$ towards $B_0 \parallel [110] = 90^\circ$. In the simulation the T_d symmetry of the four first ^{75}As neighbours was assumed but a small tilt (angles $\eta = 2.7^\circ$ and $\zeta = -0.7^\circ$ degree) of the tetrahedron was taken into account. Solid lines represent the simulated allowed ENDOR transitions ($\Delta m_S = 0$, $\Delta m_I = \pm 1$) while the dashed lines show the normally forbidden transitions ($\Delta m_S = 0$, $|\Delta m_I| > 1$).

Similar line splittings from the non-equivalence of the first neighbour nuclei are observed in the angular dependence pattern when rotating the crystal around the [110] direction from [001] = 0° towards [110] = 90° (see fig. 3.15). Here the ENDOR lines (allowed and forbidden) in the frequency range from 49 to 280 MHz of the four nearest ^{75}As nuclei were detected. As in the previous case, only “sum” frequencies ($m_S = -1/2$) could be measured. The experimental frequencies are marked by dots, the simulated ones for the high symmetrical As antisite model are presented as the solid (allowed) and dashed

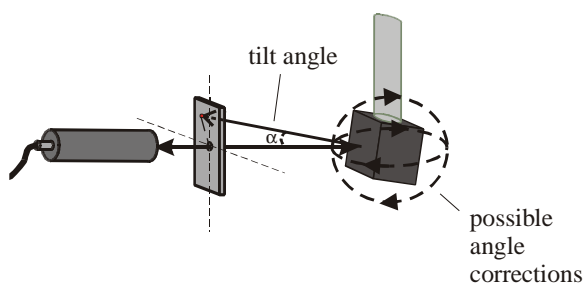
(forbidden) lines. The fully diagonalized simulations were performed with the same interaction parameters ($a/h=170.8$ MHz; $b/h=54.6$ MHz; $q/h=11.5$ MHz) as before. In the (110) rotation plane one expects 9 lines of allowed transitions for each m_S -state if the high symmetry (T_d) model of the EL2 defect is assumed. In the tetrahedral configuration the nuclei 1 and 2 (see fig.3.10(a)) must be magnetically equivalent and, therefore, their ENDOR lines must coincide. Experimentally this is not the case. One observes a splitting of the “equivalent” lines with the maximum value of 10.7 MHz for the [001] orientation (near 160 MHz, allowed transitions). This value is noticeably different from that observed for the same orientation while rotating the crystal in (001) plane (6.6 MHz). This fact confirms the surmise about the non-coincidence of the measured and theoretically simulated planes. The further fitting of the measured and simulated lines taking into account a tilt of the crystal which is different in this case ($\eta=2.7^\circ$ and $\zeta=-0.7^\circ$ degree) evidences the “experimental” reason of the observed non-equivalence. Therefore, in order to establish whether the T_d model is correct or not one has to establish an independent control of the crystal orientation.

3.4.2 Tilt of the crystal and its correction

In order to check whether the ENDOR line splittings of the first neighbour shell of the EL2 defect were really due to crystal misalignments additional safeguards were necessary. For that a further increase of the precision in the orientation control of the sample was important. In order to avoid the deviation of the measured and expected planes a more precise procedure of the sample preparation and orientation was performed. The sample was cut and polished on a special goniometer with X-ray control in order to minimize the deviation of the sample surfaces from the crystallographic planes. The maximum of the deviation of a sample prepared in such way was less than 0.4° . This enabled us to control the orientation of the crystallographic plane of the bulk GaAs with the reflected beam of the He-Ne laser with almost the same precision. As a next step the correction of the crystal tilt (which is caused mainly by the faulty attachment of the crystal to the holder with glue and is noticeable only with the laser control) should be possible (see fig.3.16). This correction must be made from the top of the cryostat during the experiment when the

crystal is already inserted into the microwave cavity. For that purpose the special sample holder (tilt-corrector), which was inserted with the sample into the working parts of the Fabry-Pérot resonator, was designed (see Section 2.4, Chapter 2).

uncorrected orientation:



exact orientation after the tilt elimination:

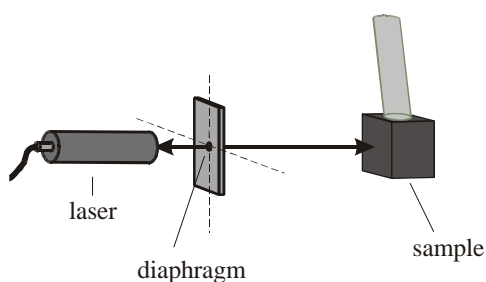


Fig. 3.16 Tilt control and correction. With the laser beam reflected from the surface of the crystal (prepared with the constant X-ray control to avoid the deviation of the surface from the crystallographic plane) and with the sample holder goniometer the proper orientation could be controlled and corrected with the high precision.

In figure 3.17 the measured ENDOR spectra before and after such correction for two main orientations $B_0 \parallel [100]$ and $B_0 \parallel [110]$ are shown.

It is evidently seen that with the correction of the measured plane the splitting of the ENDOR lines is eliminated. The lines of the equivalent nuclei coincide and their positions fit with the ENDOR line positions which were predicted theoretically for the tetrahedrally coordinated As ligands (see figures 3.17; 3.18).

More precise determination of the interaction parameters of the first four ^{75}As ligands, which was possible after the correction of the measured main orientations, yields the result: $a/h = 170.5 \pm 0.4$ MHz; $b/h = 54.3 \pm 0.4$ MHz; $q/h = 11.5 \pm 0.4$ MHz; $\theta_b = 0^\circ$ and $\theta_q = 0^\circ$. The determination was made with the assumption that all 4 nuclei are tetrahedrally coordinated and a small non-equivalence is not hidden in the measured ENDOR line-width.

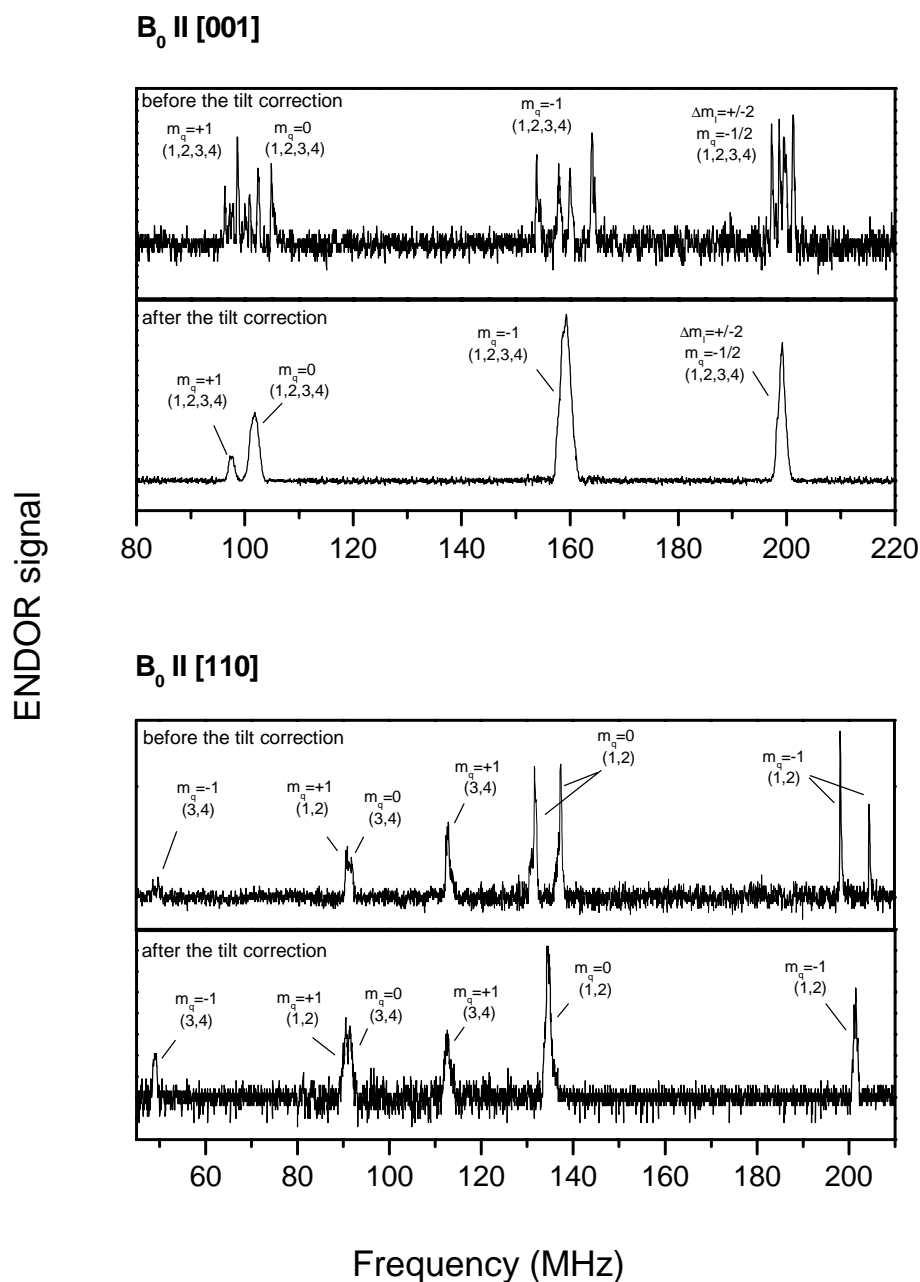


Fig. 3.17 W-band ($B_0 = 3080$ mT) MCDA-ENDOR spectra of the EL2 defect for two main orientations $B_0 \parallel [001]$ and $B_0 \parallel [110]$ measured before and after the crystal tilt correction. The quadrupole transition numbers m_q are marked as well as the numbers of the interacting nuclei (1-4 – see also fig. 3.10(a,b)). The electron spin state for all lines is $m_S = -1/2$.

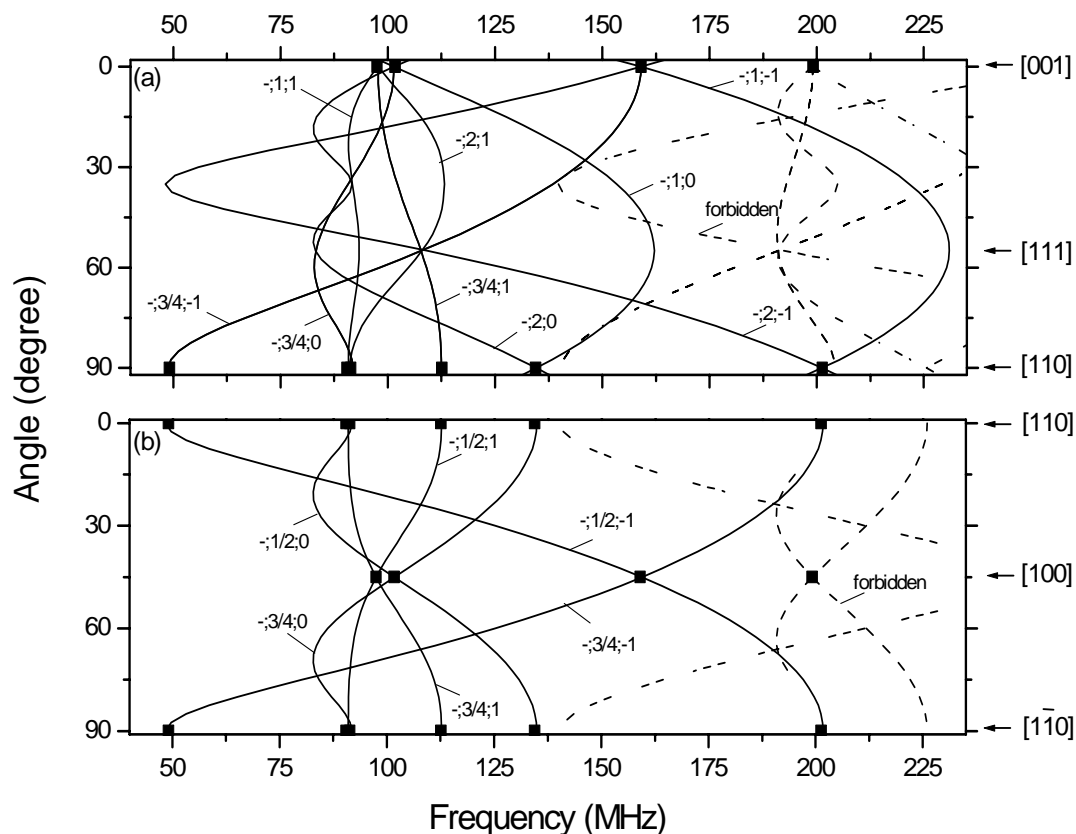


Fig. 3.18 The positions of the MCDA-ENDOR lines measured after the misalignment corrections for main crystallographic orientations (solid squares) and the simulated ENDOR angular dependencies ($m_S = -1/2$) for (110) and (001) rotation planes (lines – figures (a) and (b) respectively). In the simulations the high T_d symmetry of the nearest neighbours was assumed.

However, the experimental inhomogeneous ENDOR lines for $B_0 \parallel [001]$ remain still broader than one would expect in the case of an exact coincidence of the equivalent lines (see fig. 3.17). One of these lines measured at near 159.2 MHz is shown in figure 3.19. This inhomogeneous Gaussian-shape-like line consists of four “homogeneous” (with respect to the nearest neighbours) lines which result from the interaction with four Arsenic nuclei (ENDOR transitions with quadrupole quantum numbers $m_q = -1$, for ref. see fig.3.18). The typical ENDOR line width measured in W-band is about 0.6 MHz. In the picture, the large dashed line presents the expected Lorentz-shape-like line in the case of

an exact coincidence of four equivalent lines. The intensity of this line is recalculated with the assumption that the areas of the experimental line and the expected one are the same. The intensity of each homogeneous line which makes up the expected one is smaller by a factor of 4. In figure two of them (numbers 1 and 2) are separated in “extreme” case (the largest separation which is possible in the experimental line width). This distance between them, which is about 2MHz, is actually the unresolved difference in the ENDOR frequencies which can be hidden in the experimental line. The experimental error of the direction determination which lies within 0.5° degree can not account for the 2MHz unresolved frequency difference. Therefore, one can not exclude a small non-equivalence of the first ^{75}As nuclei. In the first order approximation, the 2MHz of the unresolved frequency difference correspond to about 4 MHz of the isotropic superhyperfine interaction constant ($\Delta a/h$), or $\theta = 4^\circ$ degree of deviation of tensor principal axis from the $\langle 111 \rangle$ symmetry.

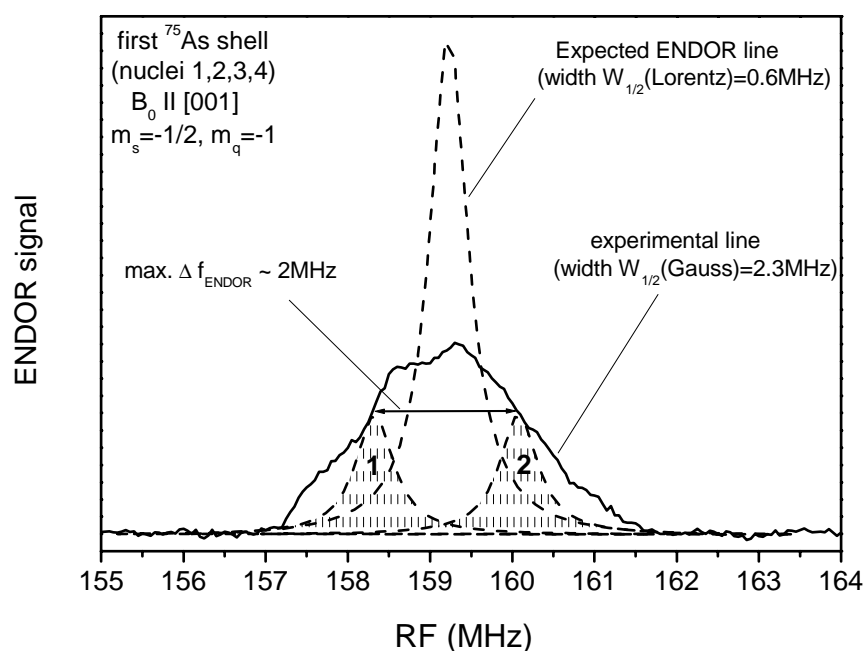


Fig. 3.19 The experimental inhomogeneous ENDOR line (solid) and the expected one (large dashed) which was simulated with the assumption of an exact coincidence of equivalent homogeneous lines. Two of the homogeneous lines (1,2) are also shown with the largest possible separation which is approximately 2MHz. This separation is frequency difference which can not be resolved because of the ENDOR line width.

From the above one can conclude that the first As neighbour shell of the EL2 defect shows almost undisturbed $\langle 111 \rangle$ symmetry to a high extent, but within the experimental error a small non-equivalence of the first neighbours ($<1.5\%$ in shf constants) is still possible. All additional line splittings observed in W-band were caused by small misalignments of the sample. In frame of the experimental error, the first neighbour shell of the EL2 defect is near identical to the isolated As_{Ga} defect observed after electron irradiation in SI GaAs at low temperatures [Krambrock 1992].

3.4.3 $\text{As}_{\text{Ga}}\text{-As}_i$ pair model: high field revision MCDA-ENDOR

The $\text{As}_{\text{Ga}}\text{-As}_i$ pair (C_{3v} symmetry) model was based mainly on the first MCDA-ENDOR experiments of the EL2 defect as a result of the observation of satellite lines between 90 and 130 MHz which were attributed to a different As interaction from that of the first 4 nearest ligands [Meyer 1988]. These lines, which showed very low intensity compared with that of the four nearest As neighbours were interpreted to originate from an additional As nucleus, As_i , situated in an interstitial position, nearly two bonds length away from the As_{Ga} antisite (4.88\AA) (see figure 3.20). The shf and quadrupole parameters of the As_i were determined to be $a/h = 215\text{ MHz}$, $b/h = 44\text{ MHz}$ and $q/h = 4.8\text{ MHz}$. However, these large constants were questioned later because they are in disagreement with simulations of the EL2 EPR line widths [Wirbeleit and Niklas 1997].

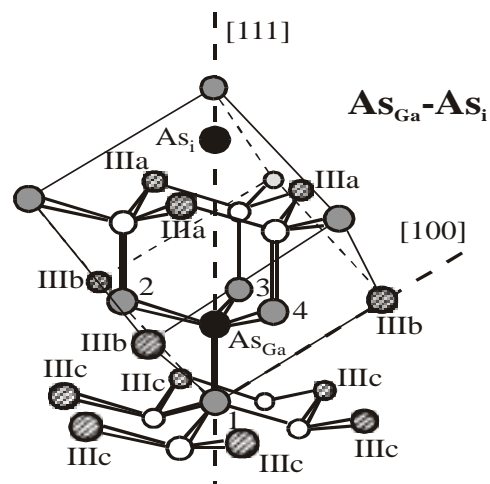


Fig. 3.20 The $\text{As}_{\text{Ga}}\text{-As}_i$ model of the EL2 defect.

The charge state of the As interstitial was claimed to be As^+ , As^- or As^{3-} with resulting electron spin zero. For the charge state As_i^0 both constituents of the pair would be paramagnetic and could have either a fine structure dipole-dipole interaction (estimated to be approx. 50mT) or due to exchange interaction be in a spin singlet or triplet state. This is not observed by EPR.

For the pair model a low binding energy between As_{Ga} and As_i was calculated which seems to be in disagreement with the high thermal stability of the EL2 defect, which is stable almost until 950°C. Rapid quenching from temperatures higher than 950°C destroys EL2, while slow cooling from 950°C allows its reformation. It should be noted that the EL2 concentration was not yet measured at elevated temperatures. Thus, at say 700°C or 800°C there may be a small concentration present as a result of a dynamical equilibrium between destruction and reformation, while at 950°C this concentration is Zero.

In the $As_{Ga} - As_i$ model the charged interstitial must influence the As neighbours in the first shell. The quadrupole interaction of the first ligands should be different. The q -values estimated for ligand 1 has to be near 1 MHz different from q of ligands 2-4 (see fig.3.20) and should give rise to additional lines in ENDOR spectra [Meyer 1988]. This was not observed with the highly resolved W-band MCDA-ENDOR. The high symmetry of the first neighbour shell does not allow the existence of the As_i situated so close to the center of the defect. Furthermore, the simulations of the expected As_i ENDOR angular dependence with the parameters claimed by Meyer et al. [Meyer 1987] yield an angular pattern which is not supported by the experiment. The example of such simulation for the (001) rotation plane is illustrated in figure 3.21 (solid lines).

From the W-band ODENDOR investigations we could not confirm the ODENDOR lines of the As interstitial in the EL2 defect as was assumed by Meyer [Meyer 1988]. Later, we will see that there are other arguments against the $As_{Ga} - As_i$ model such as the EPR line width (see Section 3.5). Now the question arises, whether the EL2 defect is the isolated As_{Ga} , the same as was observed after low temperature electron irradiation in SI GaAs, or is a low symmetry As_{Ga} -related defect. For that the low frequency ODENDOR lines of the EL2 defect have to be investigated.

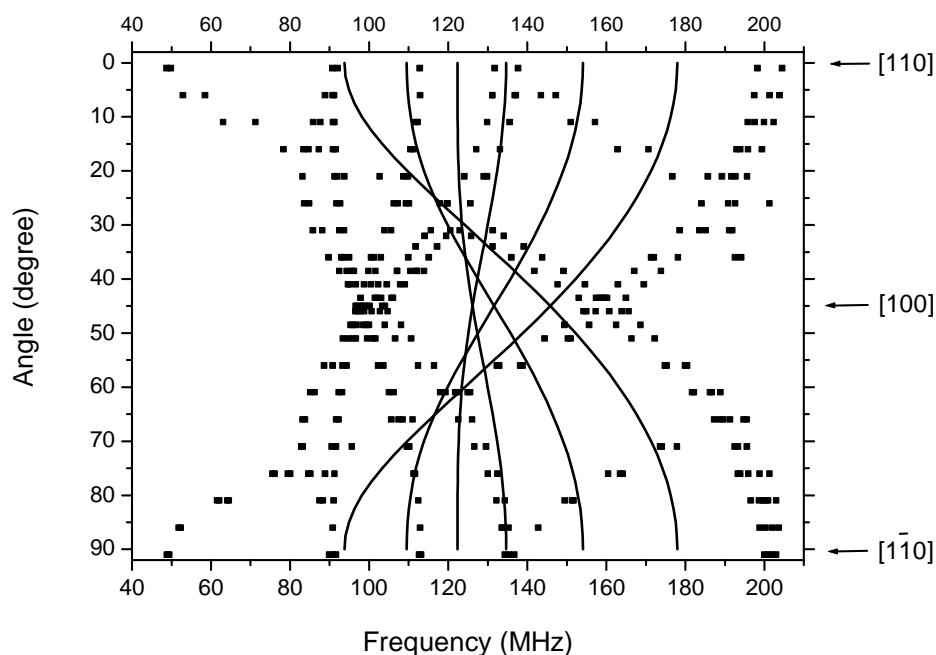


Fig. 3.21 Angular dependence of the W-band MCDA-ENDOR lines experimentally measured at $B_0=3080$ mT rotating the crystal in (001) plane from $B_0 \parallel [110]=0^\circ$ towards $B_0 \parallel [110]=90^\circ$ (dots) and simulated angular dependence of the As_i -related MCDA-ENDOR spectra (solid lines) in the same plane with the parameters $a/h = 215$ MHz, $b/h = 44$ MHz, $q/h = 4.8$ MHz taken from the reference [Meyer 1987].

3.4.4 The higher As shells of the EL2 defect

The MCDA-ENDOR spectra of the nearest As neighbours were not distinguishable from those of an isolated As_{Ga} , while the next ^{75}As shell detected with MCDA-ENDOR seemed to have a lower symmetry caused by a small distortion of the EL2 defect.

Figure 3.22(a) shows the W-band MCDA-ENDOR spectrum of the higher shell while setting the external magnetic field $B_0 \parallel [001]$. Two line groups were observed: one between 31 and 36 MHz and a second with lower intensity between 39 and 42 MHz. All lines shift to the higher frequencies when increasing the magnetic field ($m_s = -1/2$) and originate from the interaction with the ^{75}As nuclei.

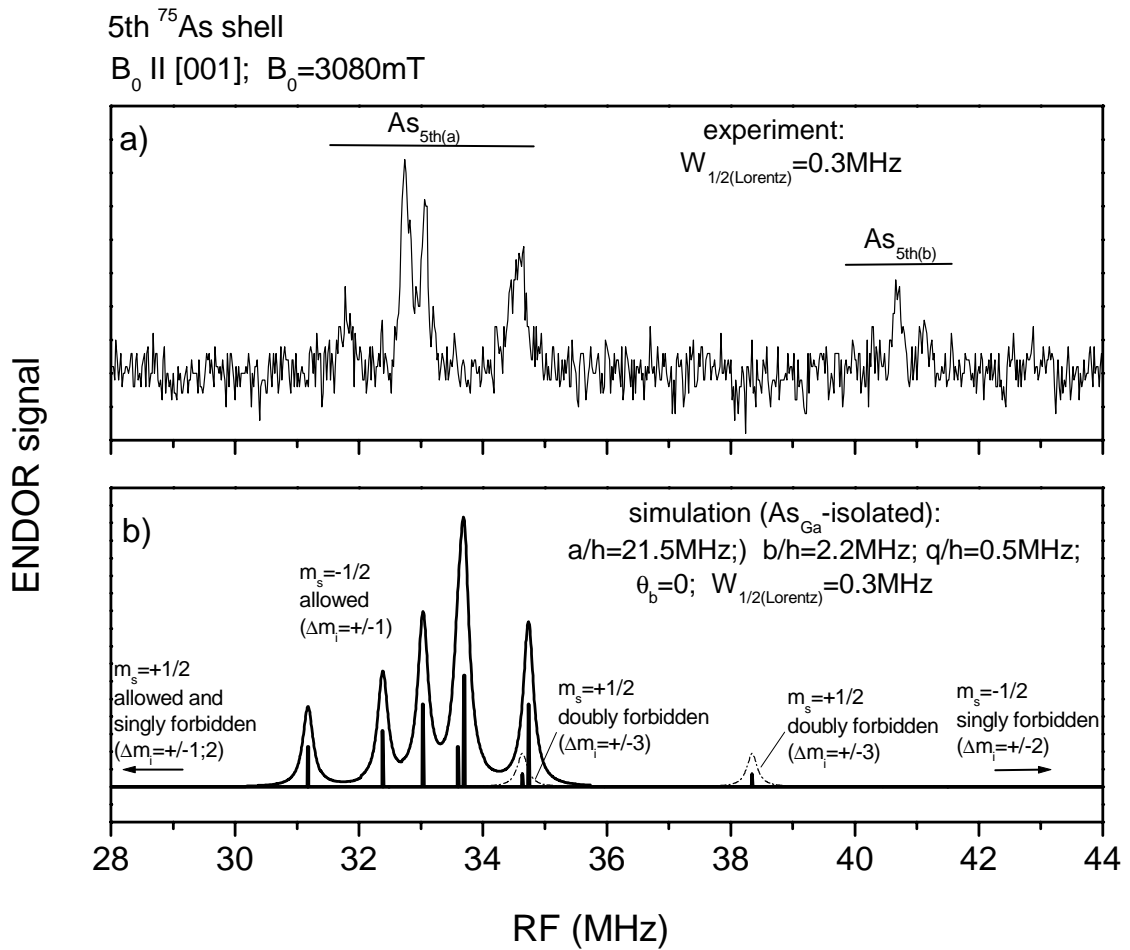


Fig. 3.22 a) MCDA-ENDOR spectrum of higher ^{75}As neighbour shell of the EL2 defect measured at $B_0 = 3080\text{mT}$ for the field orientation $B_0 \parallel [001]$; b) simulated ENDOR spectrum of the 5th (^{75}As) neighbour shell for the field orientation $B_0 \parallel [001]$ assuming the As_{Ga} -isolated defect with the shf parameters given in ref. [Krambrock 1992].

The question now arises how to explain these As interactions. In Table 3.1 the next neighbour shells of the As antisite defect with its symmetries, the numbers of nuclei and distances from the center are shown. As can be seen from the table the 3^d, 5th and 7th As

shell of the antisite have $\langle 110 \rangle$ symmetry. In a simple distance model the logical answer would be the next ($d = 4.67 \text{ \AA}$) ^{75}As shell after the nearest first shell, the 3^d neighbour shell with $\langle 110 \rangle$ symmetry.

Number of the neighbour shell	Nucleus	Symmetry	Number of the nuclei in the shell	Distance [\AA]
1	As	$\langle 111 \rangle$	4	2.44
2	Ga	$\langle 110 \rangle$	12	3.95
3	As	$\langle 110 \rangle$	12	4.67
4	Ga	$\langle 100 \rangle$	6	5.61
5	As	$\langle 110 \rangle$	12	6.13
6	Ga	$\langle 110 \rangle$	24	6.85
7a	As	$\langle 110 \rangle$	12	7.37
7b	As	$\langle 111 \rangle$	4	7.37

Table 3.1 Distances and symmetries of the neighbour shells of an As-antisite defect in GaAs

ligand	neighbour shell	$a/h_{\text{unrel.}}$ (MHz)	$a/h_{\text{rel.}}$ (MHz)	$b/h_{\text{unrel.}}$ (MHz)	$b/h_{\text{rel.}}$ (MHz)	$b'/h_{\text{rel.}}$ (MHz)
As_{Ga}^+	center	3098	2880	-	-	-
As(1,1,1)	1 st	189	173	44.7	46.6	-
Ga(2,2,0)	2 nd	5.52	3.99	1.42	0.99	0.63
As(1,1, $\bar{3}$)	3 ^d	0.47	0.05	0.2	-0.2	0.16
As(3,3,1)	5 th	24.5	22.3	3.54	4.15	0.08

Table 3.2 Calculated hf (shf) constants for the unrelaxed and for the relaxed isolated As_{Ga}^+ in GaAs (after [Overhof 2002])

However, the theoretical analysis of the spin density distribution on the sites of neighbours with LSDA-LMTO-ASA method [Overhof 2002] reveals the high spin density near As nuclei which are situated at the distances $d=6.13\text{\AA}$ corresponding to the 5th neighbour shell with the same $\langle 110 \rangle$ symmetry. On the sites of the mentioned 3^d neighbour shell, which was assumed in the analysis earlier by Meyer et al. [Meyer 1987], the total spin density was determined to be close to Zero (see table 3.2 and fig. 3.23).

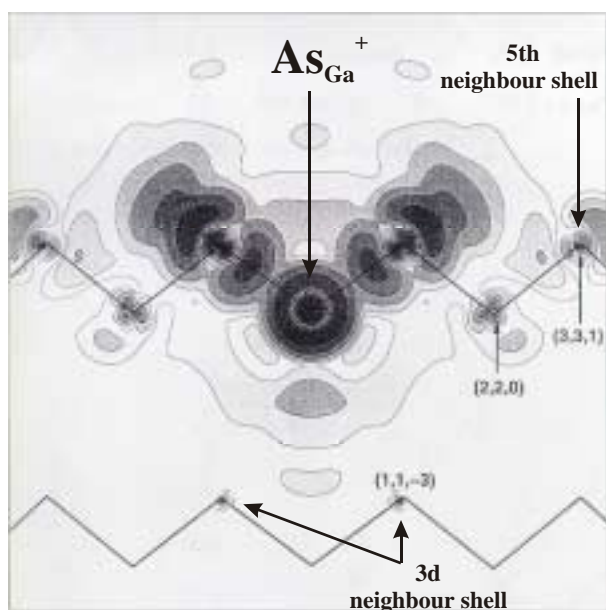


Fig. 3.23 Spin density distribution calculated in LSDA using a LMTO-ASA Green's function method for the As_{Ga}^+ defect in GaAs (after [Overhof 2002])

This result of the theoretical investigation gives a new view on the interpretation of the higher shell ENDOR spectra. In principle, with ENDOR only symmetry, principal

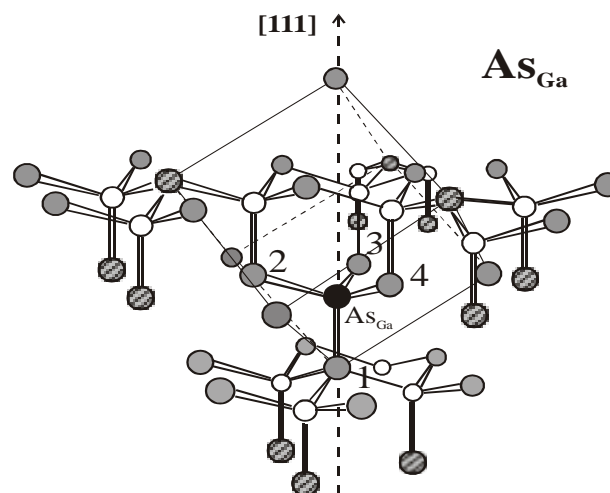
values and orientations of the shf and quadrupole tensors can be determined. Thus, the observed As interactions in low frequencies can also be attributed to the 5th As shell of the antisite. In view of this model the MCDA-ENDOR analysis was made assuming the interaction with the 12 ^{75}As nuclei of the 5th neighbour shell (see fig.3.24).

In the experiment 6 lines were observed in the frequency range from 30 to 42 MHz (see fig.3.22(a)). The same number of ENDOR lines one expects for each m_S -state simulating the ENDOR spectrum for $B_0 \parallel [001]$ assuming the high symmetry of the defect. But in this case (when only one set of the interaction parameters must be taken) the simulated line positions could not be fitted with the experimental ones assuming the interaction with 12 As nuclei of the 5th as well as of the 3^d neighbour shell. The attempts to explain the lines near 41MHz with the forbidden transitions were not successful either. The only explanation of such a result could be the splitting of the interacting shell into subshells of

equivalent nuclei, which is caused by a small distortion of the defect symmetry not observable in the first shell. In this case, the lines between 31 and 36 MHz would belong to the 5th_(a) subshell and the lines between 39 and 42 MHz to the 5th_(b) subshell. The interactions with Arsenic nuclei belonging to 5th_(a) subshell differ not much (see fig.3.22(a),(b)) from those which were determined previously from K-band MCDA-ENDOR measurements for the higher ⁷⁵As shell of the isolated As_{Ga} defect ($a/h=21.5\text{MHz}$, $b/h=2.2\text{MHz}$, $q/h=0.5\text{MHz}$ – see ref. [Krambrock 1992]). Unfortunately, the intensity of the lines does not allow to measure their angular dependencies to make more rigorous conclusions about the exact symmetry of the detected higher shell. Because of that the exact picture of the disturbance is not clear.

Fig. 3.24

The 5th neighbour shell of the As-antisite defect



● - ⁷⁵As nuclei of the 5th shell
(● - As; ○ - Ga)

It should be mentioned, that the small distortion of the EL2 defect reflected in the W-band MCDA-ENDOR on the higher interaction shells (subshells) was also observed in K-band MCDA-ENDOR spectra measured previously [Meyer 1988, Krambrock 1992]. The ENDOR lines belonging to the split subshell were detected near 30MHz setting the resonant field B_0 parallel to [100]. If to compare these spectra with the MCDA-ENDOR measured on the created by electron irradiation defect which was attributed to the isolated As-antisite, no lines appeared in this region for the isolated As_{Ga} [Krambrock 1992].

The support for the low symmetry of the EL2 one finds also comparing the MCDA of the both defects: isolated As_{Ga} and the EL2. For the isolated As_{Ga} a single derivative like MCDA as expected for a simple $A_1 \rightarrow T_2$ transition is characteristic while the complicated MCDA of the EL2 (see fig.3.2) reflects the splitting of the excited states which is caused by the symmetry lowering.

Ligand	Shell	$(a/h)_{\text{unrel.}}$ (MHz)	$(b/h)_{\text{unrel.}}$ (MHz)	$(b'/h)_{\text{unrel.}}$ (MHz)
$\text{As}_{\text{Ga}}^+(0,0,0)$	center	3056	0.15	0.11
As (1,1,1)	1st	190	44.8	0.22
As (1, $\bar{1}$, $\bar{1}$)		198	43	0.05
As (3,3,1)	5th (subshell (a))	31	3.5	0.06
As (3, $\bar{3}$, $\bar{1}$)	5th (subshell (b))	33	3.7	0.02

Table 3.3 The calculated hyperfine and superhyperfine constants for the unrelaxed ($\text{As}_{\text{Ga}}^+ - \text{V}_{\text{Ga}}^{3-}$) impurity in GaAs (after [Overhof 2002])

From the experiments it is clear that the cause of the symmetry lowering can not contribute significantly to the shf interactions, because otherwise it would have been detected with the ENDOR and in the EPR line width. A Ga-vacancy (V_{Ga}) without a nuclear spin is a most probable reason of such a disturbance. It should be diamagnetic (V_{Ga}^- or $\text{V}_{\text{Ga}}^{3-}$) otherwise dipole – dipole coupling would lead to the splitting of the EPR lines. This was supported with recent calculations of a second nearest neighbour pair, an $\text{As}_{\text{Ga}}^+ - \text{V}_{\text{Ga}}^{3-}$ pair defect, with the LSDA-LMTO-ASA method [Overhof 2002] which found a positive binding energy of about 0.3 eV for this defect pair (see fig.3.25). It is interesting to note that in such configuration of the paramagnetic defect (the EL2) the nonequivalence of the first ^{75}As neighbour nuclei is rather small (see table 3.3) and lies

not far from the experimental error of the unresolved ENDOR line width ($\Delta a/h \sim 4\text{MHz}$, see Section 3.4.2). The influence on the higher (5^{th}) neighbour shell is of the same order of magnitude ($\sim 2\text{MHz}$ difference in shf constants), but this difference makes up the larger part in comparison with the average shf values (a/h and b/h – see table 3.3) which are characteristic for the higher shell. This difference can be already noticeable. Thus, the $\text{As}_{\text{Ga}}^+ - \text{V}_{\text{Ga}}^{3-}$ model, in which the Ga vacancy causes the distortion of the 5^{th} As neighbour shell without noticeable influence on the first neighbour shell, could be an alternative model of the EL2 defect.

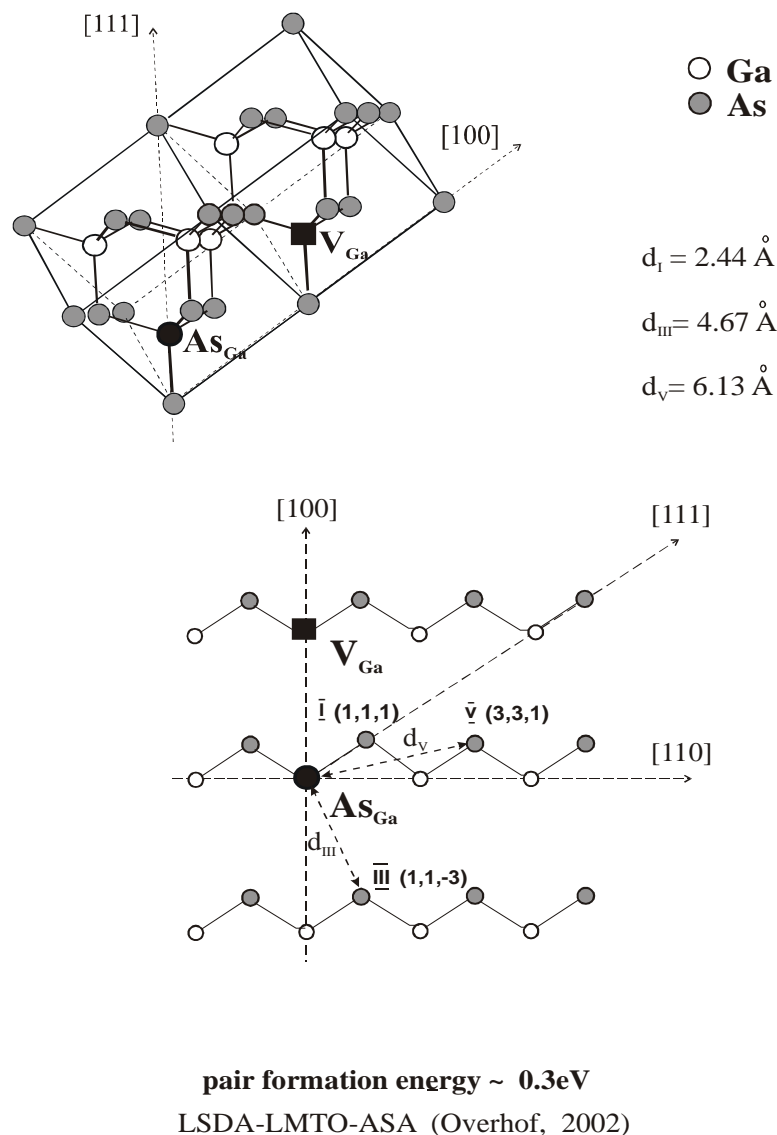


Fig. 3.25 The $(\text{As}_{\text{Ga}}^+ - \text{V}_{\text{Ga}}^{3-})$ model as proposed model for the EL2 defect [Overhof 2002].

3.5 MCDA-EPR: line width analysis of the EL2 defect

For the EL2 defect the large line widths of the EPR spectra (~35-38 mT) are characteristic. The reason is the huge number of shf lines which are superimposed in the inhomogeneously broadened EPR line. The width of each individual homogeneous line making up the total EPR spectrum is mostly of the order of 10^{-3} mT and this width is of the same value as an ENDOR line width. In the EL2 system with the electron spin $S=1/2$ and nuclear spin of the interacting nuclei $I=3/2$ for both electron Zeeman levels there are $N=(3n_1+1)(3n_2+1)\dots(3n_k+1)$ sublevels (here n_k are the numbers of the equivalent nuclei in the sense that their shf interaction is the same for a particular field orientation of B_0). Therefore, there are up to N EPR transitions which cause the loss of the shf resolution in case of the EL2 where the number of the interacting nuclei is large. For example, for B_0 oriented in $\langle 100 \rangle$ direction the EPR line consists of $N=4225$ lines due to shf interaction with 4 ^{75}As nuclei of the first neighbour shell which are all, at that orientation, equivalent and with 12 As nuclei of the next interacting shell which are supposed (in high symmetry) to be equivalent with n_k numbers 4 and 8.

The situation is more complicated in the case of the large superhyperfine and quadrupole interactions which cause significant off-diagonal elements in the spin Hamiltonian. Then the normally forbidden transitions ($\Delta m_S = \pm 1$, $|\Delta m_I| > 0$) are at least partially allowed. Taking into account these transitions is essential. The number of the lines dramatically increases. That causes an additional broadening of the EPR lines. All possible transitions have to be calculated with their transition probabilities. To analyse such an EPR line, what is necessary in order to check the defect model, for a system consistent of one electron ($S=1/2$) and 6 interacting nuclei with $I=3/2$ (the simplest case for $\text{As}_{\text{Ga}}\text{-As}_i$ model, the As_{Ga} , the four nearest As neighbours and the As_i) one must fully diagonalise the 8192 rank spin Hamiltonian matrix. If one assumes that each of the four hyperfine split lines does not noticeably depend on the spin state of the central As ($I=3/2$) the rank of the matrix can be reduced to 2048. But it is still a complicated mathematical problem to diagonalise such a matrix [Wirbeleit and Niklas 1997]. At high magnetic fields, where the electron Zeeman interaction becomes larger in comparison with the hf and quadrupole constants, the probability of the EPR forbidden transitions is less. Therefore, one expects the “clear” EPR spectra which can be analyzed in first order perturbation theory without taking into

account the higher order effects. The equidistance of the four hyperfine EPR lines in W-band spectra showed that this assumption is justified (see fig.3.7).

The W-band MCDA-EPR line width was analyzed in order to check the two competing models of the EL2: As_{Ga} -isolated or $\text{As}_{\text{Ga}}\text{-As}_i$ complex. Measuring the angular dependence of the K and W-band EPR it was noticed that the line width varies by about 2.5 mT. It is smallest for $B_0 \parallel [001]$ and largest for $B_0 \parallel [111]$, both in K- and in W-band spectra. The MCDA-EPR line widths in W-band are smaller by about 2 mT compared to K-band measurements. This result was expected because of reduced contributions of forbidden transitions in W-band. For example, those MCDA-EPR line widths measured very carefully with the lowest microwave power levels for $B_0 \parallel [001]$ are 38.0 ± 0.8 mT and 35.7 ± 0.8 mT, in K- and W-band, respectively.

It is important that the MCDA-EPR line width measured in K-band is in agreement with X-band conventional EPR measurements. The value of 33.0 mT has been determined for the peak-to-peak line width (W_{pp}) of the conventional X-band EPR spectrum for $B_0 \parallel [001]$ in [Dischler and Kaufmann 1988]. This width corresponds to 38.0 mT for $W_{1/2}$ of the K-band MCDA-EPR. Such result excludes a broadening of the line because of the saturation mechanism of the MCDA-detected EPR.

For the line width simulation the MCDA-ENDOR parameters of Ref. [Meyer 1987] have been used, i.e. $g = 2.04$, $a = 2656$ MHz (central ^{75}As nucleus), and the shf parameters: $a/h = 167.8$ MHz, $b/h = 53.9$ MHz (4 next nearest As neighbours); $a/h = 35.2$ MHz, $b/h = -1.3$ MHz (3 second nearest As neighbours); $a/h = 19.5$ MHz, $b/h = 3.2$ MHz (9 second nearest As neighbours). In order to examine the $\text{As}_{\text{Ga}}\text{-As}_i$ pair model the As interstitial was considered with its shf parameters $a/h = 215$ MHz and $b/h = 44$ MHz. Anisotropic shf interaction parameters b have been included in the calculations for orientations different from [001]. Later, when the W-band MCDA-ENDOR was measured and analyzed, the same simulations for two models were performed with the new shf parameters (see for reference table 3.5) of the nearest four As nuclei. The results were compared.

As was mentioned, in W-band in first order perturbation theory all nuclei can be treated independently. One needs only to know their shf interaction constants and their nuclear spin quantum numbers. The quadrupole interactions of the neighbouring nuclei can be neglected in first order. With the knowledge of the MCDA-ENDOR line width which is about 1 MHz all allowed EPR transitions can be summed up to give the total ODEPR spectrum in first order.

	$\Delta W_{1/2}$ for $B_0 \parallel [001]$, (mT)	$\Delta W_{1/2}$ for $B_0 \parallel [111]$, (mT)	$\Delta W_{1/2}$ for $B_0 \parallel [110]$, (mT)
Experiment: W-band EPR	35.7±0.8	37.4±0.8	36.8±0.8
Simulated: As _{Ga} – As _i complex	39.5	42.8	41.3
Simulated: Isolated As _{Ga}	33.7	39.1	36.0
Simulated: As _{Ga} – As _i complex (new parameters)	40.4	51.6	47.9
Simulated: Isolated As _{Ga} (new parameters)	34.7	38.9	37.7

Table 3.4 EPR line width of the experimental W-band EPR spectra and simulated ones (two different models: isolated As_{Ga} and As_{Ga}-As_i complex) for main crystallographic orientations.

Calculating the full half width ($W_{1/2}$) of the MCDA-EPR spectra for the isolated As_{Ga} model the values 33.7 mT, 39.1 mT and 36.0 mT were obtained for the [001], [111] and [110] orientations, respectively. Considering the interaction with an additional As interstitial in the As_{Ga}-As_i model we obtain 39.5 mT, 42.8 mT and 41.3 mT. The measured line widths in W-band are 35.7 mT, 37.4 mT and 36.8 mT, respectively, with an error of ±0.8 mT. The simulations performed with the parameters derived from W-band MCDA-ENDOR brought us to the following results: 34.7mT, 38.9 mT and 37.7 mT (isolated model); 40.4 mT, 51.6 mT and 47.9 mT (As_{Ga}-As_i model) for the [001], [111] and [110] orientations, respectively (the results are collected in the table 3.4).

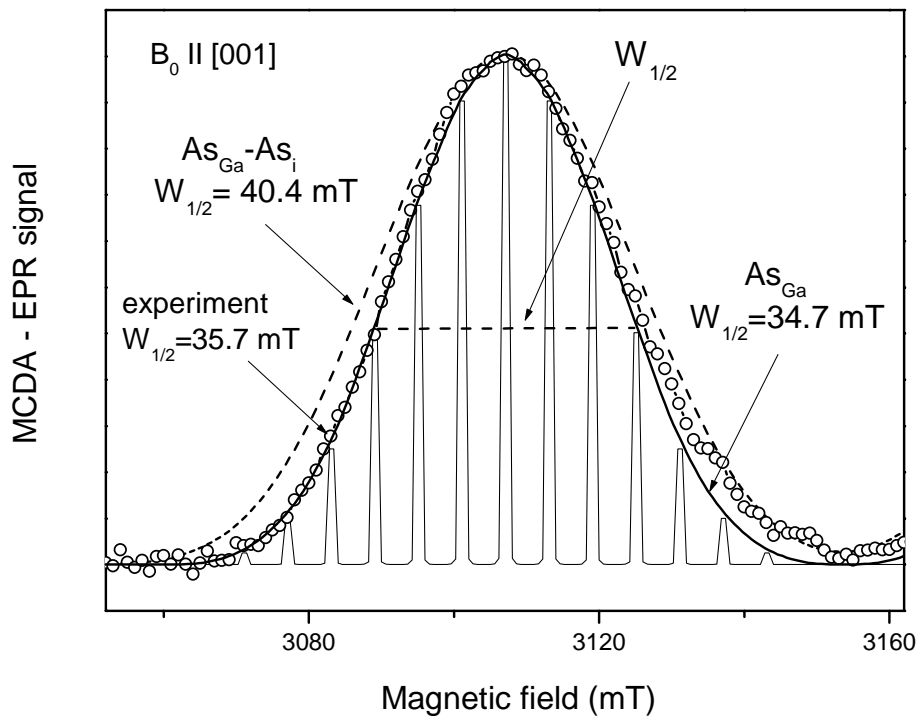


Fig. 3.26 First order simulation of the EPR line width ($W_{1/2}$) of the EL2 defect for $B_0 \parallel [100]$ assuming two different models: isolated As_{Ga} and $As_{Ga}-As_i$ complex (In the simulations of the illustrated lines the parameters derived from W-band MCDA-ENDOR were used).

Thus, when calculating the EPR spectra of the EL2 defect in first order perturbation theory with the old (of Ref. [Meyer et al. 1987]) as well as new (W-band) MCDA-ENDOR parameters and comparing the simulations with the W-band EPR experimental results we can exclude the $As_{Ga}-As_i$ complex as the model for the EL2 defect. An additional As_i with $a/h = 215$ MHz and $b/h = 44$ MHz leads to too large line widths in comparison with the experiment. The difference is especially noticeable in the case when new interaction parameters (which can be regarded as more exact) were taken for the simulations (see figures 3.26; 3.27).

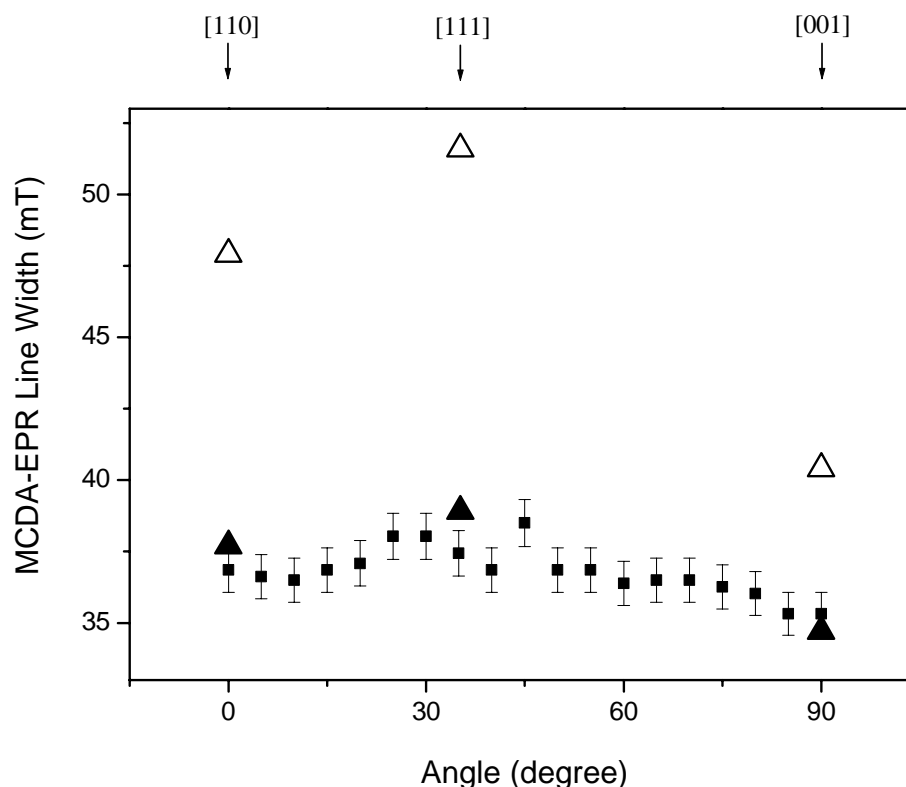


Fig. 3.27 Angular dependence of the W-band (94 GHz) EPR line width ($W_{1/2}$) of the EL2 defect measured rotating the crystal in (110) plane (squares with the bar) and simulated for three main orientations [110], [111] and [001] supposing the two different models: isolated As-antisite (solid triangles) and $As_{Ga}-As_i$ complex (open triangles). The simulations were made with the parameters derived from the W-band MCDA-ENDOR (see table 3.5)

The comparison of measured and simulated angular dependencies of the line width supports somehow the As-antisite model with T_d symmetry (see fig 3.27). However, the other experimental information such as the complex MCDA line shape of the EL2, the MCDA-ENDOR spectra of the higher ^{75}As neighbour shells and the observation of the isolated As_{Ga} defect (not stable at room temperature) with the characteristic simple MCDA [Krambrock and Spaeth 1992] do not support the high symmetry of the defect. One of the explanations of such a result could be that the cause for the symmetry lowering does not contribute the hyperfine interaction. The vacancy (for example V_{Ga}) without a nuclear spin is the most probable candidate for such a “disturber”.

3.6 Conclusions

The structure of the EL2 defect in semi-insulating GaAs with the high-frequency/high-field W-band MCDA-EPR and MCDA-ENDOR was investigated. It was possible at high fields to measure MCDA-EPR and MCDA-ENDOR spectra which are not strongly influenced by higher order effects. The experiment shows that at high fields corresponding to W-band measurements the pseudo-nuclear splittings of the MCDA-ENDOR lines are eliminated (they are below 0.2 MHz). That fact and the detection of the lines of only the $m_S = -1/2$ state enabled us to analyze the measured spectra more precisely and unambiguously. The expected disappearance of the lines caused by forbidden ENDOR transitions was not observed. Those lines still arise in W-band MCDA-ENDOR with unexpected large intensity. But they did not complicate the analysis of the spectra. Their appearance has probably a technical reason.

With the W-band MCDA-ENDOR two interacting ^{75}As neighbour shells were detected. The shell with the large interaction constants corresponds to the first shell of the four nearest ^{75}As nuclei ($d=2.44\text{\AA}$) with $\langle 111 \rangle$ symmetry. The angular dependencies of the first nearest neighbour shell in two rotation planes ((001) and (110)) show the high (T_d) symmetry of the four interacting ^{75}As nuclei with the interaction parameters: $a/h= 170.5 \pm 0.4$ MHz; $b/h= 54.3 \pm 0.4$ MHz; $q/h= 11.5 \pm 0.4$ MHz; $\theta_b=0^\circ$ degree and $\theta_q=0^\circ$ degree (see also the table 3.5). However, a small non-equivalence of the nearest nuclei can not be excluded as long as a perturbation has a weak influence on the ENDOR line positions, i.e. a weak distortion ($<1.5\%$) can be hidden in the ENDOR line width. The interaction parameters of the first As nearest neighbour shell of the EL2 defect are nearly identical to that of the isolated As antisite defect observed after low temperature electron irradiation of SI GaAs. For the EL2 defect no lines from an additional As nucleus which were attributed earlier to an As_i were detected. In the case of the EL2 defect the next detected As ligand shell with $\langle 110 \rangle$ symmetry shows a splitting into subshells. They were attributed to the 5th neighbour shell of the As antisite defect based on recent theoretical calculations of the $\text{As}_{\text{Ga}} - \text{V}_{\text{Ga}}$ pair defect. The MCDA-ENDOR spectra of the higher shell could not be fitted with the fully diagonalised simulations if a T_d symmetry of the EL2 defect was assumed. The only reason for the splitting of the ^{75}As shell with $\langle 110 \rangle$ symmetry into two subshells could be a distortion due to a 2nd partner in the defect further away.

	a/h , [MHz]	b/h , [MHz]	θ_b , [°degr.]	q/h , [MHz]	θ_q , [°degr.]
1 st (⁷⁵ As) shell of the EL2	170.5 ±0.4	54.3 ±0.4	0	11.5 ±0.4	0

Table 3.5: Superhyperfine and quadrupole interaction constants of the first ⁷⁵As neighbour shell of the EL2 defect determined from the W-band MCDA-ENDOR experiments.

This distortion can not be caused by an As_i nucleus as was claimed by Meyer [Meyer 1988] from the K-band MCDA-ENDOR. The W-band ENDOR investigation do not support the As_{Ga}-As_i model of the EL2 because no lines belonging to As_i were observed experimentally. Furthermore, almost T_d symmetry of the first ⁷⁵As shell excludes definitely such a configuration of the defect.

The investigation of the angular dependence of the W-band EPR line widths ($\Delta W_{1/2}$) excludes the As_{Ga}-As_i model as a model of the EL2 as well. The existence of the As_i in the defect structure would cause a large broadening of the EPR line width what is not observed experimentally. The simulations of the EPR line width for the As_{Ga}-As_i model can not explain the measured X,K and W-band EPR spectra. The behavior of the experimentally measured line widths while rotating the sample in (110) plane supports somehow the high symmetry of the EL2 defect. However, the observed similarity of the simulated (for T_d symmetry) angular dependence of the line widths and the experimental one is possible also in the case when the reason of symmetry lowering does not contribute the syperhyperfine interaction.

The main conclusion from the W-band MCDA-EPR/ENDOR investigation of the EL2 defect structure is :

The EL2 is not the $\text{As}_{\text{Ga}} - \text{As}_i$ pair defect but also different from the isolated As_{Ga} defect, observed after electron irradiation in SI GaAs at low temperature. The EL2 defect has lower symmetry, which is seen in MCDA spectrum as well as in MCDA-ENDOR of the higher neighbour shells. A surprising result of the W-band MCDA-ENDOR is that the first ^{75}As neighbour shell exhibits almost the high T_d symmetry of the four nearest interacting nuclei as in the case of the isolated As antisite defect [Krambrock and Spaeth 1992]. The EL2 defect and the isolated As-antisite are very similar if not identical with respect to their nearest neighbour interactions. On the other side, they are not identical, the EL2 must be a complex. A complex formation of the As antisite is not visible in the first neighbour shell but influences the higher interacting shells. The results of the W-band ENDOR and the EPR line width investigations display that the complex partner should not interact with the paramagnetic electron. V_{Ga} , for example, situated close to the 5th neighbour shell could cause such a distortion [Overhof 2002]. The $\text{As}_{\text{Ga}} - \text{V}_{\text{Ga}}$ pair model is an interesting alternative microscopic structure model for the EL2 defect, because it has stronger binding energy and its wavefunction is localized basically on the As_{Ga} and its first As neighbour shell as well as on the 5th shell. However, whether it is the only alternative, cannot be said at this moment. The first As neighbour shell has almost T_d symmetry, but there is a visible distortion in a higher As shell. This distortion causes the splitting of the EL2 excited state what is reflected in its highly sensitive to the defect structure MCDA spectrum.

Chapter 4

Arsenic-antisite-related defects in high resistive LT-MBE-GaAs and their relation to the EL2

4.1 Introduction

The first experiments regarding the low-temperature molecular beam epitaxy (MBE) grown GaAs (LT-GaAs) were published by Mutorani et al. in 1978 [Mutorani 1978]. They reported about the growth of GaAs by MBE at substrate temperatures lower than the usual 600°C. The investigators found in their experiments that undoped GaAs grown at 400°C becomes semi-insulating. However, only after ten years the large potential of the material was recognized after the appearance of the paper by Smith et al. [Smith 1988], where the first application of the material was presented. In this paper, LT-GaAs was used as an insulation layer to prevent the mutual influence of the devices during the operation in integrated circuits. The feature of such MBE-grown materials in the microelectronic technology provoked the great success of the material. Since then, the insulating properties (up to $10^7 \Omega/\text{cm}$) are exploited in electronic structures such as MESFETs or lasers and are very essential for integrated circuits technology. Besides the insulating behavior the importance of the low temperature material increased due to a really unique property: extremely short life times of the photo-generated carriers. The lifetimes of 100fs influenced the development of ultrafast photo switches and gated antennas for THz region taking the advantage of short lifetimes together with the high breakdown fields and the low dark currents of the material.

There are many further suggestions of LT-GaAs applications. Thin layers can be used to fabricate ex-situ non-alloyed ohmic contacts on p- and n- type GaAs. LT-GaAs buffer layers might be suitable for radiation protection of GaAs integrated circuits. The use of the semi-insulating LT-GaAs in photomixers for the generation of THz radiation seems to be promising also.

The success of this material lies in its large nonstoichiometry. Most of the features of the material arise from the presence of the native point defects in extremely high concentrations (10^{18} - 10^{20} cm^{-3}). But the mechanisms of their influence on the material properties are still not clear. Two competing models try to explain the semi-insulating properties of the annealed LT-GaAs: the point-defect model, which explains the high resistivity with Fermi level pinning by the non-compensated deep donors and the model of As clusters as buried Schottky barriers. In the second model the semi-insulating properties are believed to come from overlapping of depletion regions around the As precipitates which act as giant acceptors. Recently it was suggested that the Fermi level is dominated by the point defects in the as-grown and weakly annealed LT-GaAs and by the arsenic precipitates in the strongly annealed LT-GaAs. From the point of view of technical application the most relevant physical property of LT-GaAs is the extremely short photo-generated carrier life time. This short life time is often ascribed to the large concentration of the As_{Ga} -like defects which act as recombination centers. This may be true or not, but in any case it is not self evident.

In general, in As-rich LT-GaAs three native point defects (or complexes involving them) are favored: (1) As_{Ga} -like defect(s), Ga-vacancies (V_{Ga}) and As_i interstitials (As_i). Evidence was found for all of them but their identification is still questioned. The deep donors are arsenic-antisite (As_{Ga}) or related complexes, the acceptors are mainly Ga vacancies. The role of As_i is controversial. First principal calculations reveal a formation energy of the As_i in tetrahedral configuration that is several electron volts higher than that of As_{Ga} and V_{Ga} . Therefore, the concentration of As_i should be very low. However, more recent calculations predict a relatively low formation energy of the As_i in a split interstitial configuration (two arsenic atoms share one arsenic lattice site) which is in the order of that of the As_{Ga} and even lower than that of the V_{Ga} ([Landman 1997]). Thus, the concentration of the “split As_i ” is expected to be in the same order as the concentration of As_{Ga} and V_{Ga} . In the split interstitial configuration the As_i should act as an acceptor. The effects of arsenic (As) precipitates on the properties of the LT-GaAs are also discussed more and more often because of the large concentration of the clusters formed in material after annealing.

The dominant deep donor As_{Ga} in LT-GaAs is a part of the EL2 defect which was discussed in the previous chapter (see Chapter 3). It was mentioned there that one of the striking features of this defect is its metastable behavior at low temperatures and ability to be thermally recovered from the metastable state to the ground state by raising the temperature of the sample above the characteristic value ($T > 120-130$ K). A similar bleaching behavior was observed for As_{Ga} -related defects in LT-GaAs, although less effective, and together with the SI properties supported somehow the suggestion that the native defects in LT-GaAs are EL2-like defects [Kaminska 1992; Kowalski 1993]. However, the properties of the LT material are affected strongly by annealing. The concentration of the defects as well as their microscopic structure can be changed significantly. Annealing is often required in device processing and this fact creates the large interest in the investigation of the material change with thermal treatment. The question arises whether we deal with a “modified” EL2 because of the lattice strain in LT-GaAs or whether we have completely different As_{Ga} -related defects in LT-GaAs samples, as-grown and annealed to different temperatures. The answer to the question, how close the native defects in LT-GaAs relate to the EL2, was actually the main goal of the work presented in this chapter. The magneto-optical investigation of the native defects in as-grown LT-GaAs and material annealed to different temperatures gave some useful information to contribute to this problem.

In this chapter the results of the investigation performed with MCDA and MCDA-EPR techniques on substrate-free GaAs layers grown by MBE at low substrate temperature ($\sim 200^\circ\text{C}$) and annealed after growth at different temperatures are presented and discussed. The preparation of the samples with a lift-off technique enabled us to measure the material above the band gap of GaAs. Also for photon energies smaller than the band gap energy it was an advantage to avoid the influence of the GaAs substrate. Therefore the magneto-optical measurements were performed within a wide range of photon energies (0.7eV to 1.8eV). The MCDA-EPR measurements were performed in K(~ 24 GHz)- and W(~ 94 GHz) bands. Finally, the bleaching properties of As_{Ga} -related defects in LT-GaAs and of EL2 defects in SI bulk GaAs have been investigated for comparison.

4.2 Sample preparation

4.2.1 Growth and annealing

The low temperature GaAs is usually grown in the temperature range between 200°C and 250°C. The other growth parameters such as a beam equivalent pressure (BEP), regulating the ratio of the partial pressure of source materials, are normally left unchanged compared to the standard growth procedure. The growth rate – determined by the Ga-flux – amounts to 0.5-1µm/h. The thermal control of the substrate mounts in MBE machines is not suitable for this temperature range. Thus, it is difficult to compare the absolute growth temperatures used in different publications. Apparent contradictions can originate in different thermal sensors which can have absolute errors of $\pm 50^\circ\text{C}$.

The main feature of the low-temperature materials is an enormous amount of excess Arsenic of up to 1.5%. The reason is that the As partial pressure is chosen higher than the Ga pressure in the MBE chamber. That is necessary to avoid the creation of Ga_{As} antisite defects, which are more preferable under standard growth conditions because of the different sticking coefficients of As and Ga atoms. Due to the epitaxial growth process the atoms of the LT-GaAs layers assume the lattice constant of the substrate in the horizontal direction. The As-antisite defects introduce strain into the lattice due to the As-As bond having a larger bonding length than the replaced As-Ga bond. Up to a certain thickness the epitaxial layer grows in a monocrystalline manner exhibiting pseudomorphic tension. If the layer thickness exceeds a critical point, the epitaxial layer relaxes and stacking faults appear at the boundaries to compensate for the different lattice constants. There is no external pressure forcing the epitaxial layer to assume the lattice constants. This results in an increased lattice constant perpendicular to the sample surface.

The concentration of excess Arsenic – and thus the defect concentration – increases with decreasing growth temperature. That is why the substrate temperature during growth must be (to some constraints) low to obtain the highly nonstoichiometric material.

The low temperature GaAs samples used in this work were grown in MBE systems of the Institut für Technische Physik I (Erlangen, Germany) and the University of California (Santa Barbara, USA). The temperature of the GaAs substrate was near 200 °C with small

differences for different wafers. The thickness of the samples varies from 1 μm to 1.5 μm , but is equal for samples within the series (see table 4.1).

The properties of the LT-GaAs are also very sensitive to the post-growth annealing temperature. It is known that there is an immense drop of defect concentration with its increasing. The annealing of the LT-GaAs leads to a tremendous change of the transport mechanism, trapping time and absorption characteristics in the appropriate way. Thus, it is important to investigate the influence of this parameter on the properties of the material. Therefore, after growth the samples were annealed in N_2 atmosphere at different temperatures from as-grown up to 660 $^\circ\text{C}$ with minimal temperature step 50 $^\circ\text{C}$. To suppress the Arsenic evaporation from the film the surface of the sample during the annealing was laid face down onto a GaAs substrate.

4.2.2 Epitaxial lift-off technique

After annealing the samples were prepared with a lift-off technique where the MBE films were separated from the GaAs substrate and glued onto glass. This procedure was performed in Institut für Technische Physik I of University of Erlangen (Germany).

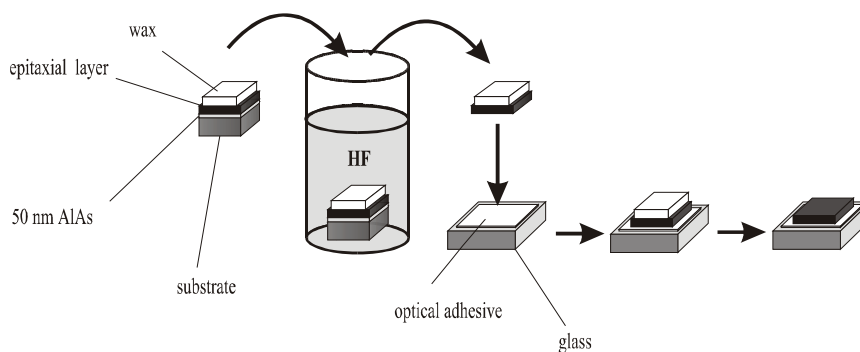


Fig. 4.1 Sequence of the epitaxial lift-off technique. (after Dankowski [Dankowski1998])

The epitaxial lift-off technique is an essential preparation method for our experiments. This technology is a highly selective wet etching process which enables the separation of the epitaxial layer from the substrate ([Yablonowitch 1987]). The fundamental requirement to perform the lifting off of the epitaxial layer is the presence of a 50nm-100nm “sacrificial” layer of AlAs between the epitaxial film and the substrate. In figure

4.1 the sequence of the procedure, which can be divided into several steps, is schematically shown:

- As a first step, the small piece of wax should be melted on the top of the structural sample. The wax protects the sample surface and stabilizes the lifted-off epitaxial layer;
- Then the wax-covered sample must be dipped into an HF-acid (hydrofluoric acid; HF:H₂O, ratio 1:9) to perform the etching of the sacrificial AlAs layer. The HF is extremely selective and etches AlAs while GaAs is almost resistant to this etch. When the AlAs layer is removed completely, the GaAs-layer is lifted off the substrate;
- Finally, the GaAs-layer must be taken out of the acid and glued onto glass substrate. The gluing is performed with an optical adhesive. The wax can easily be removed by Trichlor-ethane.

The lift-off technique is a unique tool to prepare the epitaxial layer for optical investigations. This is the essential way which allows the optical measurements above the band gap of the substrate material. Thus, the epitaxial lift off-technique is a key technology for the experiments and results presented in this Chapter. Furthermore, it is important that the samples are substrate free what eliminates the boundary substrate-film strain caused by the lattice mismatch of the LT-GaAs and GaAs substrate.

4.2.3 Overview over the samples

Wafer	MBE Machine	T_{growth}	As - source	Thickness	Temperatures of annealing	Duration of annealing	Preparation
TP104	Erlangen	220 °C	As ₄	1 μm	as-grown, 400 °C, 500 °C, 600 °C.	10 min	Lift-off
TP105	Erlangen	200 °C	As ₄	1 μm	as-grown, 300 °C, 400 °C, 500 °C, 600 °C.	10 min	Lift-off, coated
990706C	UCSB (Santa Barbara)	235 °C	As ₄	1 μm	as-grown, 300 °C, 350 °C, 400 °C, 450 °C, 460 °C, 500 °C, 510 °C, 550 °C, 560 °C	15 min	Lift-off
990708A	UCSB (Santa Barbara)	235 °C	As ₄	1 μm	550 °C, 610 °C, 660 °C.	15 min	Lift-off
980306A	UCSB (Santa Barbara)	225 °C	As ₄	1 μm	as-grown, 350 °C, 400 °C, 500 °C.	15 min	Lift-off
990706B	UCSB (Santa Barbara)	255 °C	As ₄	1 μm	as-grown, 500 °C	10 min	On GaAs substrate (MBE grown at 600 °C- Wafer 980306B)
TP276 (Al _{0.2} Ga _{0.8} As)	Erlangen	230 °C	As ₄	1.5 μm	as-grown, 500 °C, 600 °C	15 min	Lift-off, coated
TP677	Erlangen	180 °C	As ₄	1 μm	as-grown, 500 °C	15 min	Lif-off

Table 4.1 Overview over the Lift-off LT-GaAs samples investigated with MCDA and MCDA-EPR technique.

4.3 MCDA-EPR of MBE grown LT-GaAs

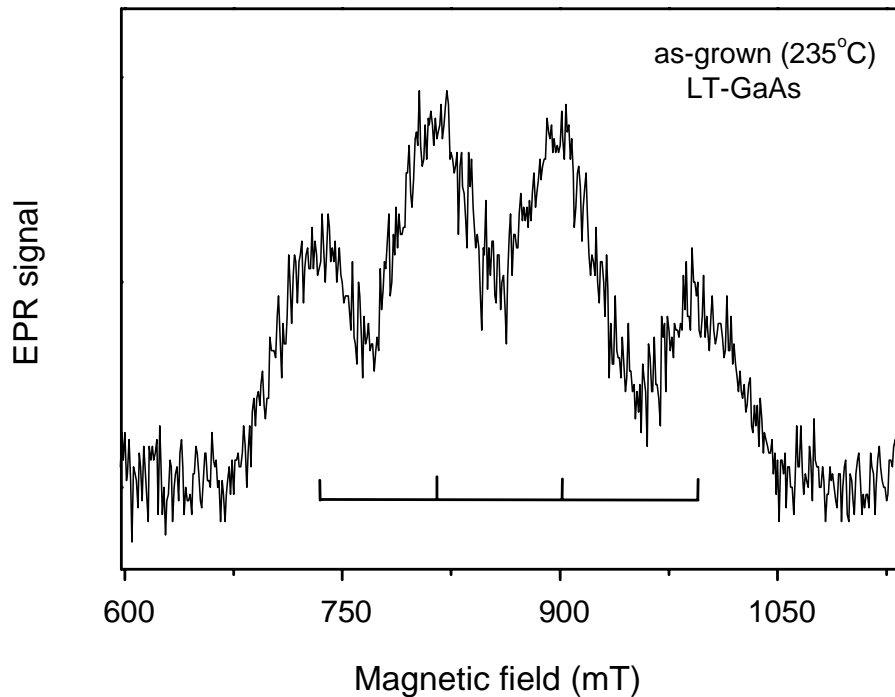


Fig. 4.2 MCDA-EPR spectrum of as-grown (235°C) LT-GaAs MBE film measured at a photon energy of 0.92eV. Microwave frequency was 24.8GHz (K-band), measurement temperature 1.5K. Microwave power delivered to the cavity \sim 5mW.

The typical MCDA-EPR spectrum of a 1 μ m thick as-grown LT-GaAs layer measured in K-band (24.8GHz) via the MCDA setting the photon energy to 0.93 eV is shown in figure 4.2. Because of the low thickness of the MBE layers (\sim 1 μ m) the signal to noise ratio of the MCDA-EPR spectra is relatively low (\sim 10:1). But the optical (MCDA) detection is the only possibility to observe the EPR effect in such thin layers. Conventional EPR-detection is not possible. Such spectra are detectable (with a slight difference in the intensities and the EPR parameters for different annealing temperatures) in all investigated series of samples via different MCDA bands (see fig.4.3). Exceptions are only the samples

annealed at 600°C and above. Heating to these temperatures leads to a disappearance of the MCDA-EPR in LT-GaAs.

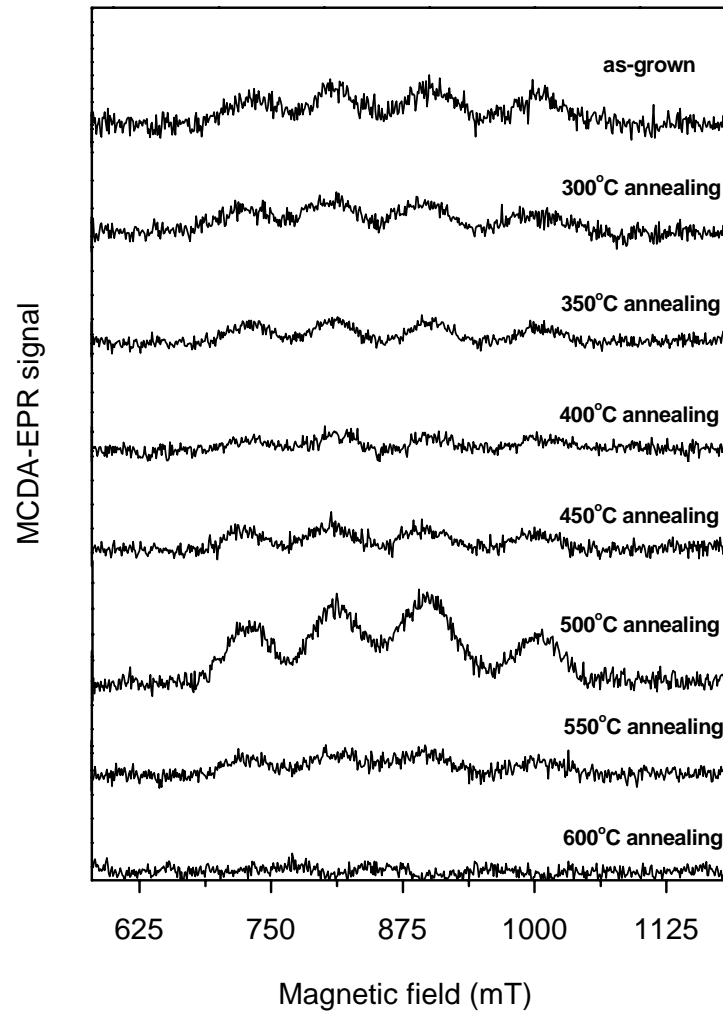


Fig. 4.3 The change of the LT-GaAs MCDA-EPR as a function of annealing at different temperatures. The spectra were measured setting the photon energy to 0.92eV and the microwave frequency at 24.8GHz. The measurement temperature was 1.5K.

The measured MCDA-EPR spectra can be analyzed with the appropriate spin Hamiltonian:

$$H = \mu_B \vec{B} \tilde{g} \vec{S} + \vec{S} \tilde{A} \vec{I} \quad (4.1)$$

where μ_B is the Bohr magneton, \vec{B} – the external magnetic field. \tilde{g} represents the Zeeman splitting tensor, and \tilde{A} denotes the hyperfine interaction tensor. The spectra show mainly the four line hyperfine (hf)-split spectra due to As_{Ga} -related defects (nuclear spin of ^{75}As is $I = 3/2$) [Krambrock 1992]. The spectra are isotropic (at least within the experimental error), therefore tensors \tilde{g} and \tilde{A} can be replaced by scalars in (4.1). Important to note are the large line widths ($W_{1/2}$) of about 40-60mT of each hf line consistent with conventional EPR measurements of such samples [Bardeleben 1992]. The hf lines are broader than those measured for the EL2 defects in SI bulk GaAs (~38 mT). The g -values of the spectra measured for as-grown and annealed samples are almost the same within of the experimental error, while the hf interaction with the central ^{75}As nucleus varies from 2595 MHz up to 2676 MHz (see table 4.2).

Annealing temperature	g -factor	Isotropic hf parameter a_{hf}/h (MHz)	$W_{1/2}$
as-grown	2.03±0.01	2595±45	49±6
300 C annealing	2.03±0.01	2568±47	50±5
350 C annealing	2.03±0.01	2598±12	48±5
400 C annealing	2.04±0.01	2582±30	47±4
450 C annealing	2.04±0.01	2676±56	56±5
500 C annealing	2.03±0.01	2665±28	58±3
510 C annealing	2.04±0.01	2630±12	57±3
550 C annealing	2.04±0.01	2660±70	56±5
600 C annealing	-	-	-
Semi-insulating bulk GaAs (EL2 ⁺)	2.039±0.002	2660±7	38.0±0.8

Table 4.2 EPR parameters of as-grown and annealed at different temperatures LT-GaAs (Wafer 990706C). Growth temperature 235°C.

The interaction with Ga nucleus ($I=3/2$) as well as with As ($I=3/2$) nucleus which is in interstitial configuration (As_i) can be ruled out. The large and isotropic hyperfine splitting of the measured spectra indicates that the defect state must be a level with a very localized

wave function which is characteristic for A_1 representation of the ground state. Neither for As_i nor for Ga_{As} theory predicts an A_1 ground state as a deep level in the band gap [Baraff and Schlüter 1985]. As for Ga_i , this defect is very unlikely in Arsenic-rich LT GaAs and the previously reported hf parameters of the Ga_i -related EPR are too small to explain the observed spectra ([Kennedy and Spencer 1986; Trombetta 1991; Wimbaur 1997]). Furthermore, the interaction with the two isotopes of Ga (^{69}Ga and ^{71}Ga with natural abundance of 60.1% and 39.9%, respectively, both of $I=3/2$) gives rise to two sets of a four line structure, the ratios in intensity and in splitting of which are determined by the ratio of natural abundance and nuclear magnetic moments, respectively. Since both Ga isotopes differ in their nuclear g -factors ($g_n(^{69}Ga)=1.34439$; $g_n(^{71}Ga)=1.70818$), different hyperfine splittings are expected in the MCDA-EPR spectrum. Interaction with different isotopes of Ga would result in a superposition of two different MCDA-EPR spectra with different hf splittings. Since the difference of the line positions of the Ga isotopes for the two external lines is greater than that for two inner ones, the outer lines must be broadened and have a smaller amplitude. The broadening of the outer lines was not observed experimentally.

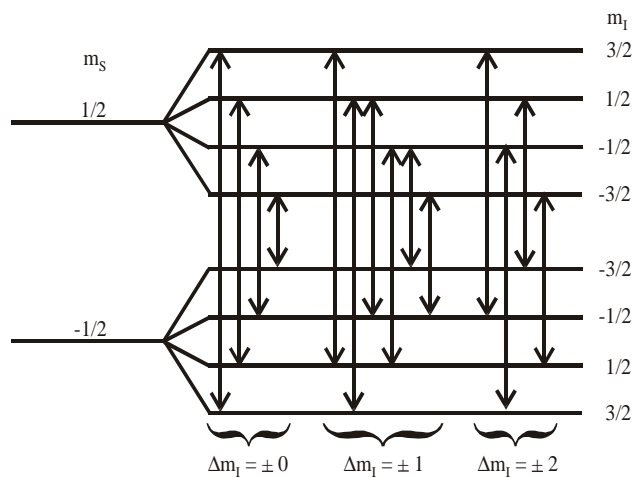


Fig. 4.4 Schematic representation of the allowed ($\Delta m_S = \pm 1, \Delta m_I = 0$; left), the “singly forbidden” ($\Delta m_S = \pm 1, \Delta m_I = \pm 1$; centre), and the “doubly forbidden” ($\Delta m_S = \pm 1, \Delta m_I = \pm 2$) EPR transitions in $S=1/2, I=3/2$ system.

The characteristic difference in intensity of the four hf lines (see fig.4.5(c)) disappears at low microwave power levels (~ 0.08 mW) where forbidden transitions are suppressed definitely [Koschnick 1999]. Since the appearance of forbidden transitions is possible even at rather low microwave power levels (~ 0.15 mW) in MCDA-detected EPR spectra because of saturation which is reached relatively easily, one can simulate the probable influence of possible EPR forbidden transitions (see fig.4.4) on the shape of the spectra.

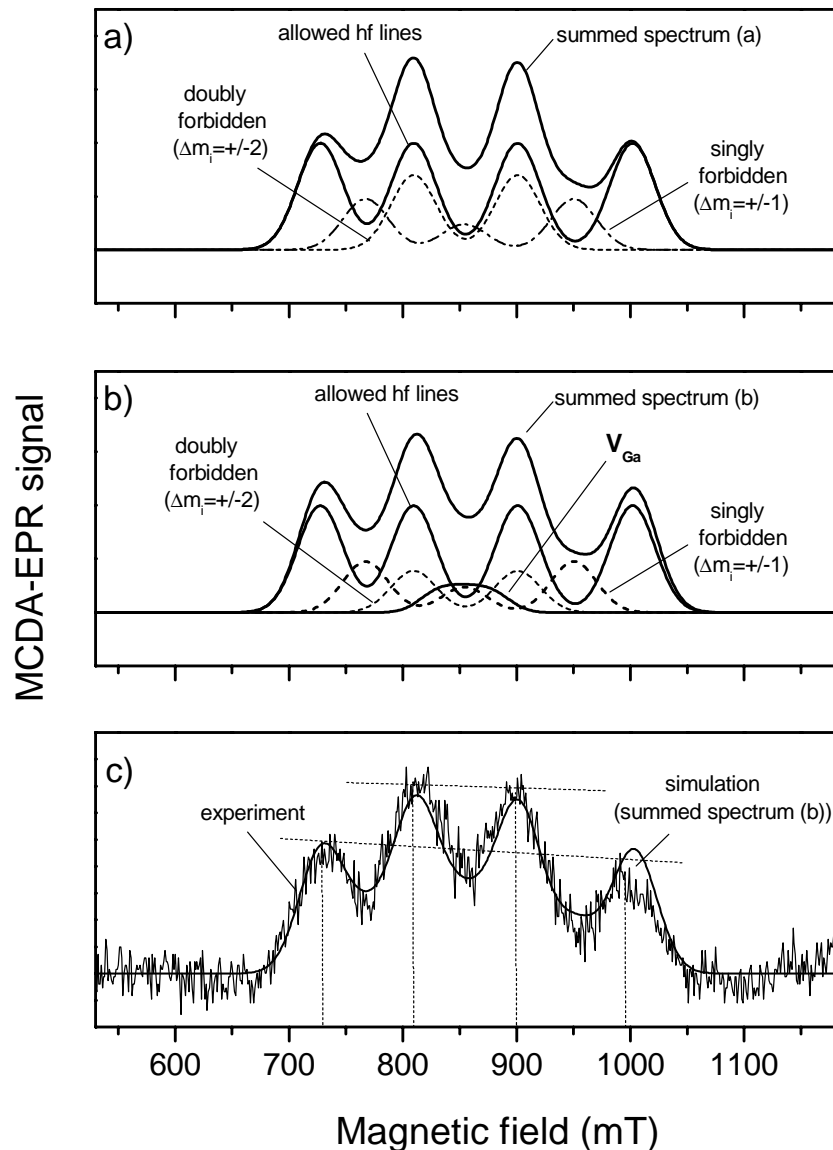


Fig.4.5 a) The simulated MCDA-EPR spectrum of the LT-GaAs (summed spectrum) as a result of a superposition of the allowed and forbidden hf split lines.
 b) The simulated MCDA-EPR spectrum (summed spectrum) as a result of a superposition of allowed and forbidden As_{Ga} -related hf split lines and V_{Ga} -related spectrum.
 c) Fitting of measured and simulated spectra.

It should be noted here that taking into account the non-equidistance of the hf lines caused by higher order terms in the spin Hamiltonian is essential in such simulations

(Breit-Rabi solution of the eigenvalue problem, see for ref. [Pake and Estle 1973], 5-3(p.146)). A good fitting of the simulated spectra with the experimental ones can be reached if all possible forbidden EPR transitions are assumed (see figures 4.4 and 4.5(a)). The only “snag” of such simulations is that the exact fitting with the measured spectra requires the intensity (probability) of the “doubly forbidden transitions” ($\Delta m_I = \pm 2$) to be larger than that of the “singly forbidden transitions”. The expectation of such a property is very low (see for ref.[Abragam and Bleaney 1986] p.p.181-186). Therefore, the superposition with the MCDA-EPR of another paramagnetic defect of a large line width and g factor of about 2.05 must be assumed. The analysis shows that the superimposed spectrum must have a line shape which is typical for different intrinsic acceptors observed earlier in bulk GaAs [Krambrock 1989]. Unfortunately, the spectrum could not be separated from the As_{Ga} -related spectrum neither when using different photon energies for the measurements nor from MCDA-EPR measurements in W-band. It should be noted that the new spectrum was detected both in the as-grown and the annealed samples. We attribute the new MCDA-EPR line to V_{Ga} -related defects for the following reasons:

- 1) V_{Ga} is a very probable defect in As rich highly nonstoichiometric LT GaAs;
- 2) Positron annihilation experiments detect a high concentration of V_{Ga} in the material [Gebauer 1997; Gebauer 2000];
- 3) V_{Ga} is a multiple acceptor with a T_2 ground state in the band gap of GaAs. Its anisotropy is not detectable probably because of the very broad EPR lines of the dominant As_{Ga} -related defect;
- 4) V_{Ga} -related defects with trigonal symmetry were detected and identified earlier in electron-irradiated GaAs [Jia 1992; Krambrock 1995]. The measured spectrum is compatible with the V_{Ga} (trigonal) for $B \parallel [100]$ with a g -value of about 2.05 and a shf interaction with one ^{75}As neighbour of about 540MHz

In addition to the V_{Ga} -related defect another MCDA-EPR spectrum was observed for samples annealed above $450^\circ C$ when exposing the material to light with a photon energy near 1.12 eV (dashed curve (unknown defect) in figure 4.6 (b), (c)). Now the shape of the

spectra is even more complicated with noticeably higher intensity of the second line (at 900 mT in K-band, see fig. 4.6 (b)).

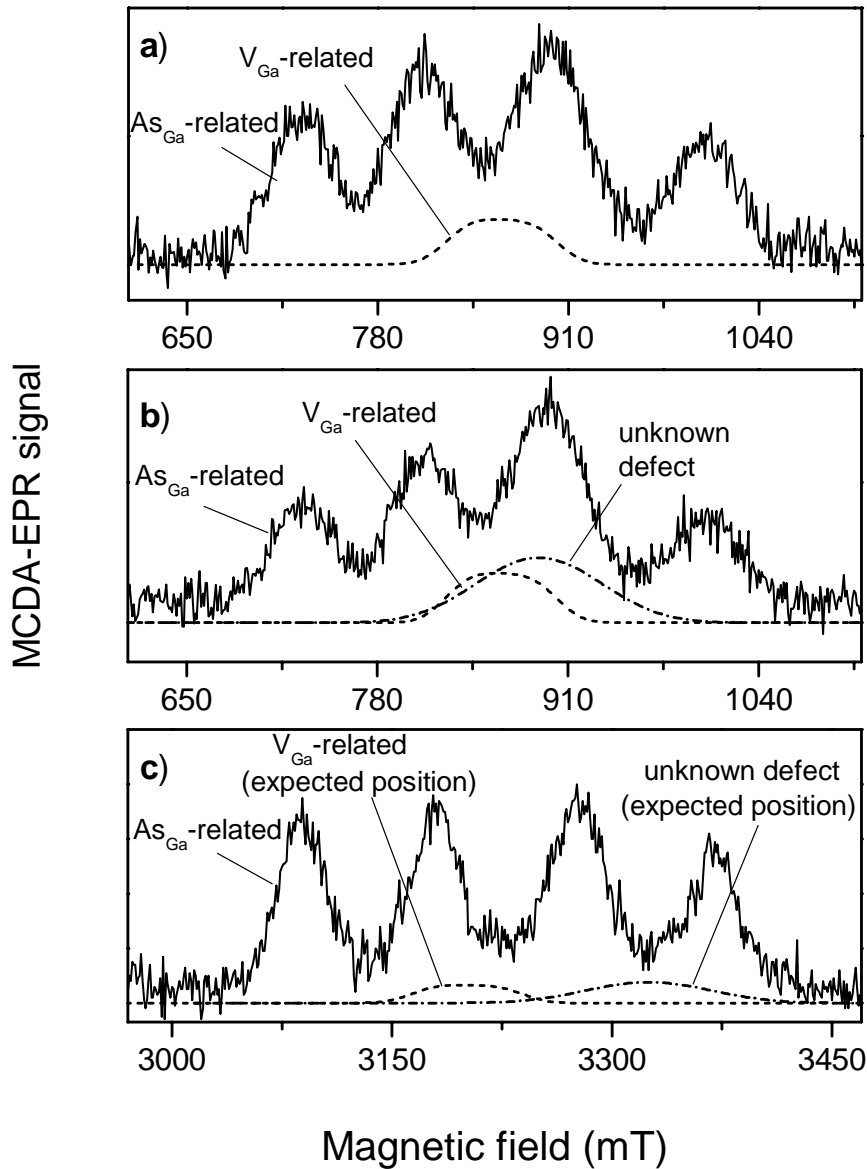
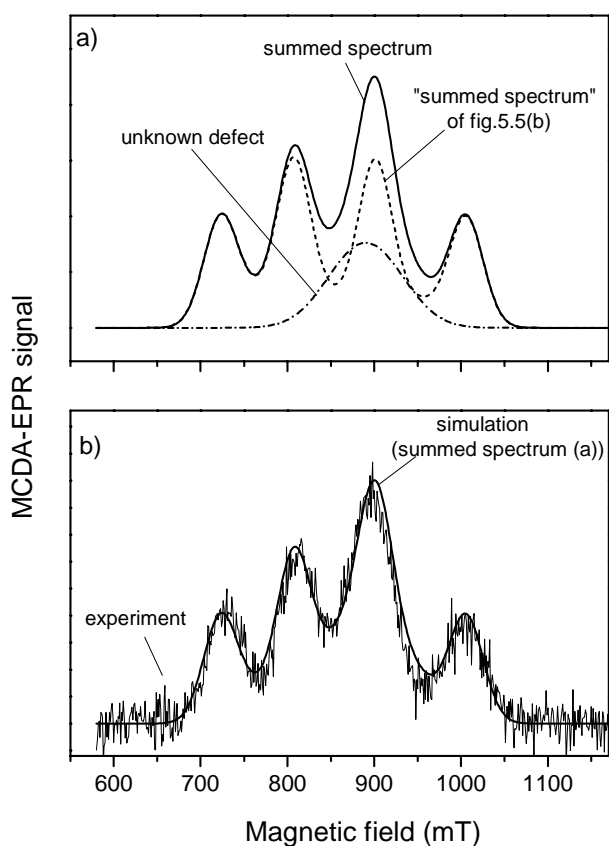


Fig. 4.6. MCDA-EPR spectra of LT-GaAs annealed at 500°C measured:

- a) at 24.8GHz with photon energy 0.92eV;
- b) at 24.8GHz with photon energy 1.12eV;
- c) at 92 GHz with photon energy 1.12eV.

Measurements temperature was 1.5K. μ W power \sim 5mW.

**Fig. 4.7**

a) The simulated MCDA-EPR spectrum (summed spectrum) as a result of a superposition of the As_{Ga}-related, V_{Ga}-related and unknown defect which was detected with photon energies near 1.12eV on LT-GaAs annealed at 500°C.

b) The simulated spectrum fits with the experimental one measured with photon energies 1.12eV at μ W-frequency 24.8GHz on LT-GaAs annealed at 500°C. Temperature of measurements 1.5K.

The fitting analysis (see fig.4.7) reveals that the second superimposed spectrum must have a g -factor of near 1.98 and line width near 70mT. Unfortunately, the large line widths and high intensity of the As_{Ga}-related spectra prevent the reliable identification of the defect. Neither the tagged MCDA technique nor high-frequency (92GHz) MCDA-EPR measurements (fig. 4.6 (c)) could separate the different spectra. Here one should take into account recent simulations of the native defects in LT-GaAs which predict that the formation energy of the As_i in a split interstitial configuration (two arsenic atoms share one As lattice site) is in the order of magnitude of that of the As_{Ga} and V_{Ga}. In such a configuration the As_i should act as an acceptor. This complex may become a deep level in the gap at high lattice strains [Landman 1997].

Within the precision of the MCDA-EPR measurements the g -value and splitting of the As_{Ga}-related EPR spectra in the as-grown layers are somewhat different from those of the annealed samples (see table 4.2). The slight difference in parameters could be an indication that we observe the EPR spectra of different As_{Ga}-related defects in as-grown

and annealed material. It should be noted that the MCDA-EPR hyperfine constant of the defect in as-grown material does not correspond to that of the EL2 defect in LEC-GaAs. Only after annealing the value is in agreement with the hf parameter ($a/h=2660\pm 7\text{MHz}$) of the prominent EL2 (see table 4.2).

4.4 MCDA and MCDA spectra “tagged” by EPR

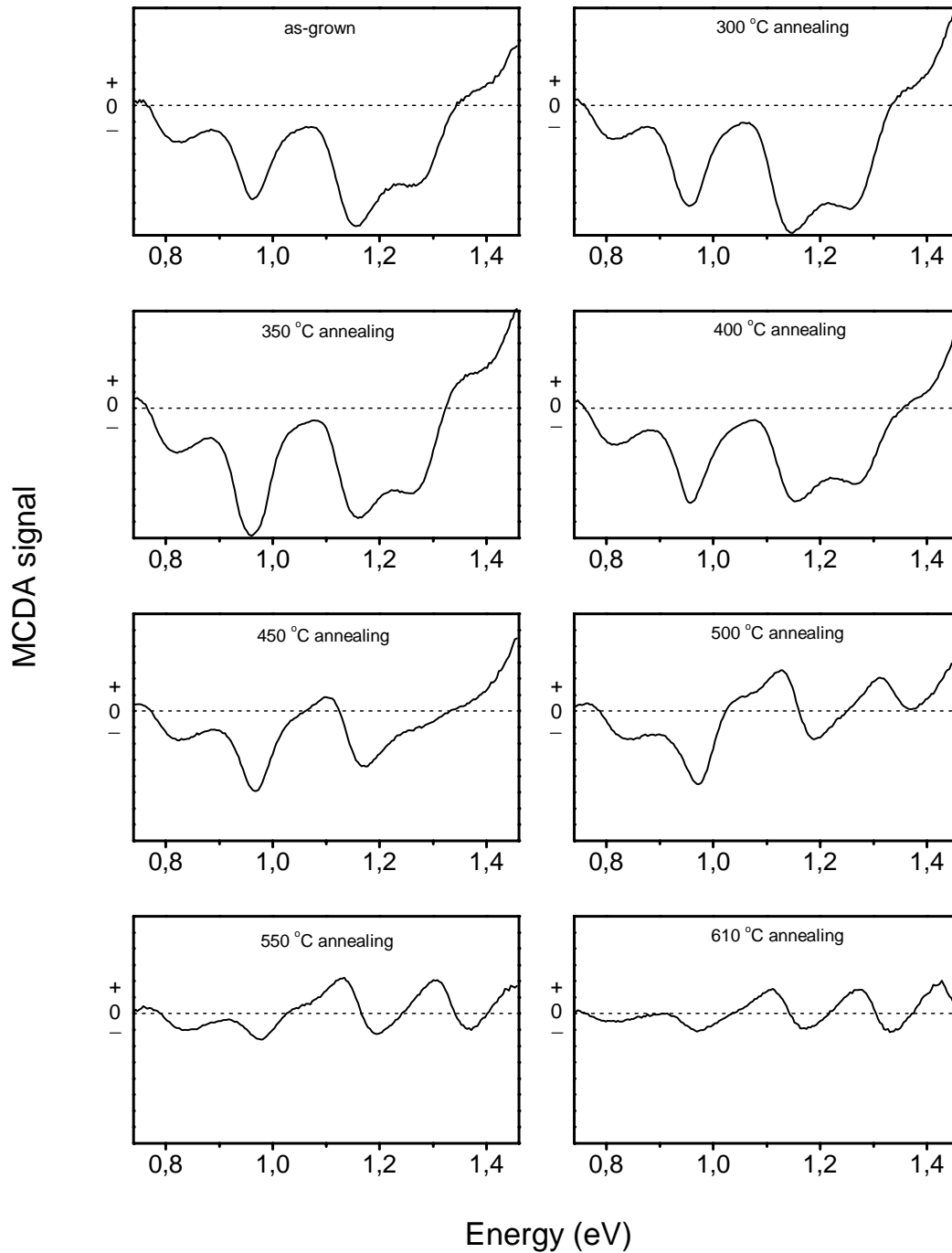


Fig. 4.8 MCDA spectra of as-grown LT-GaAs and LT-GaAs annealed at different temperatures. The strong optical interference in thin MBE layers, which affects the MCDA spectra, is seen.

Due to optical interference in the thin lift-off layers, the measured MCDA spectra are difficult to interpret (see fig.4.8). The interference is strongly superimposed on the spectra. The only reliable conclusion which can be made from such spectra is that the concentration of the defects decreases with the increase of the annealing temperature. The tagged MCDA spectra are almost undistorted by optical interference. Therefore, with tagged MCDA more rigorous conclusions are possible.

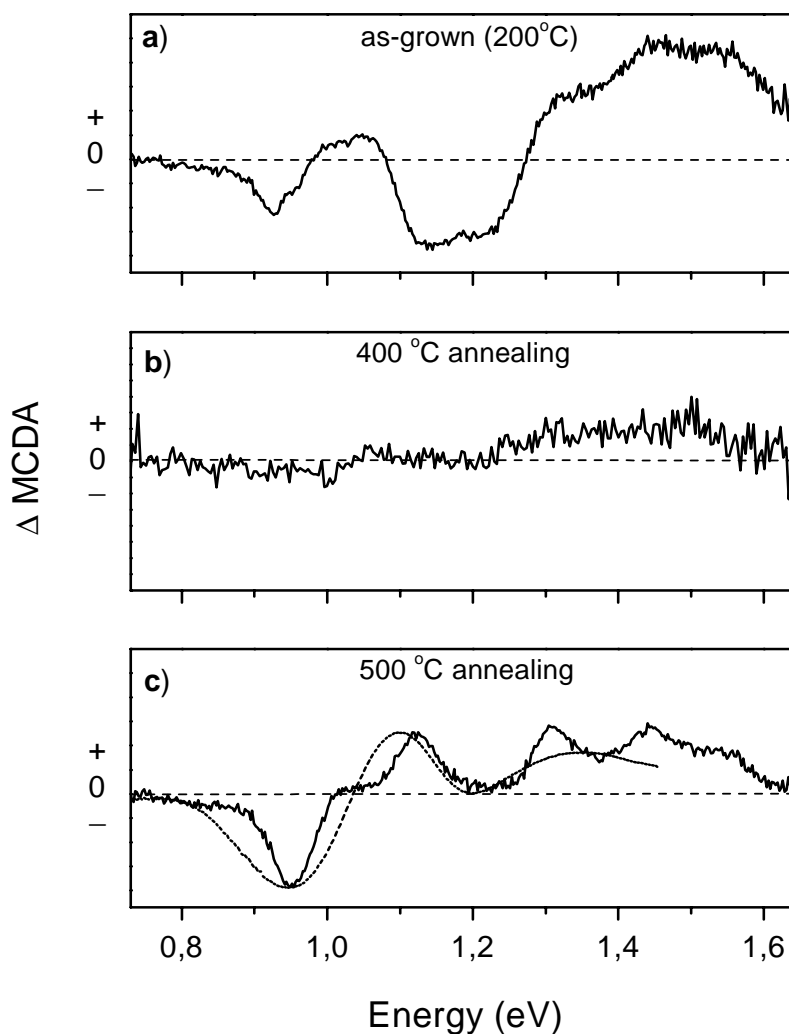


Fig. 4.9 Tagged MCDA spectra of AsGa-related defects in (a) as-grown (200°C); (b) annealed at 400°C Lt-GaAs; (c) annealed at 500°C Lt-GaAs. Measurement temperature 1.5K, microwave frequency 24.8GHz, resonance field B of 700mT. In (c) the MCDA of the EL2 defect in s.i. GaAs is shown as dashed line for comparison.

With the tagged MCDA technique by setting the EPR resonance conditions to a particular MCDA-EPR line and varying the optical wavelength one can correlate the EPR line of a certain defect with its optical properties [Spaeth 1992]. It was already said that the almost unnoticeable differences in the MCDA-EPR parameters of the As_{Ga} -related defects in as-grown and annealed material could reflect their microscopic differences. Rather strong evidence for that was obtained with the tagged MCDA measurements.

Fig.4.9 shows such excitation spectra for as-grown (a) and annealed (at 400°C and 500°C) samples, (b) and (c) respectively. Clearly, all the spectra are different. From earlier investigations of several different As_{Ga} -related defects in electron-irradiated GaAs it is known that most of them have nearly indistinguishable MCDA-EPR spectra, but different tagged MCDA spectra which serve as their fingerprints [Koschnick 1999]. MCDA-detected electron nuclear double resonance experiments confirmed evidently the difference in the microscopic structure of the defects [Spaeth 1994]. We conclude therefore that we deal with different As_{Ga} -related defects in as-grown and annealed LT-GaAs. Furthermore, one can notice the similarity of the MCDA spectrum of the annealed (500 °C) LT-GaAs sample and the MCDA spectrum of the EL2 defect (dashed line), which appears in SI bulk GaAs (see fig.4.9(c)). The critical annealing temperature lies near 400°C, where the tagged MCDA spectra nearly disappear (fig.4.9.(b)). This behaviour has been observed in different series of samples. It may indicate that the Fermi level position is shifted because of the recombination of defects or reconstruction of the microscopic structure of defects, which affect their electronic levels in the band gap.

That dramatic change of the defect properties is seen well in fig.4.10 where the MCDA-EPR spectra of LT-GaAs as-grown and annealed at different temperatures measured with photon energy of 1.12eV are shown. The interesting observation is that the MCDA-EPR measured in as-grown material decreases with the annealing temperature. At 350°C-400°C no MCDA-EPR signal is observable and at 450°C (and above) the new EPR spectra arise. This behaviour is an indication that we observe different defects in LT-GaAs as grown and annealed near 500°C.

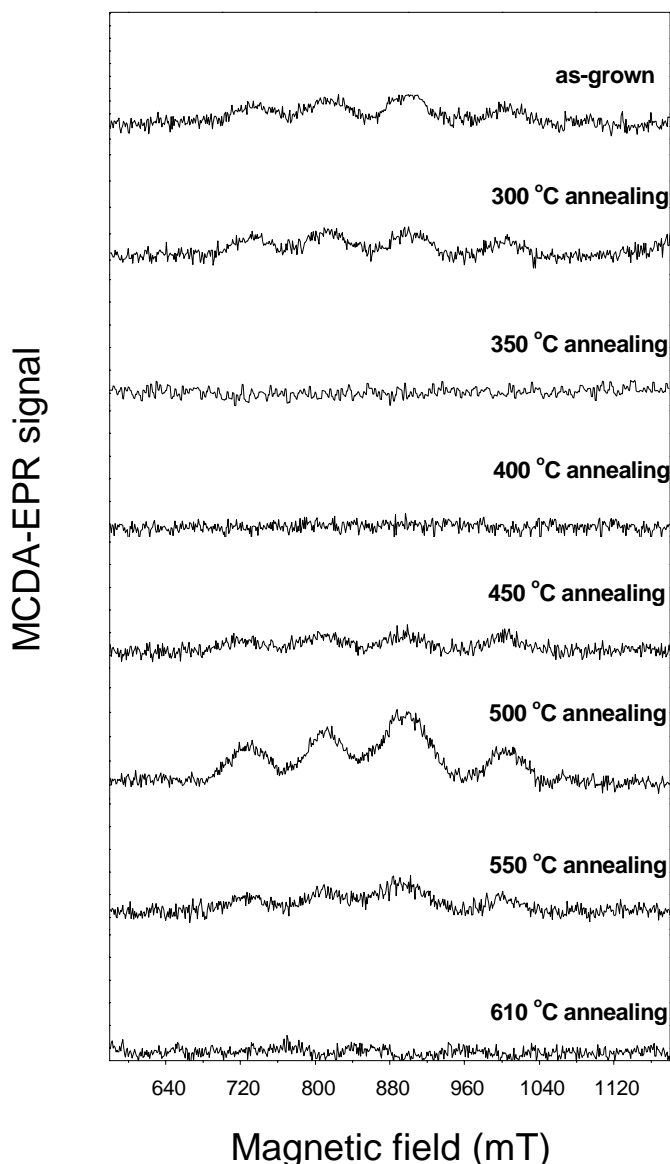


Fig. 4.10 MCDA-EPR spectra of LT-GaAs as-grown and annealed at different temperatures measured with photon energy 1.12 eV at a μ W-frequency of 24.8GHz. Temperature of measurements 1.5K. Microwave power near 5mW.

This suggestion is supported by measurements of the T_1 spin-lattice relaxation time (Fig.4.11). From such

measurements a difference between the As_{Ga} -related defects in as-grown and annealed material was found. T_1 of the defects in as-grown material was measured to be ~ 0.7 -1s at 1.5 K, while in samples annealed at 500 °C it is ~ 3.5 -4s (see fig.4.11 (a),(b)). The latter value is almost the same as that measured for EL2 defects in SI bulk GaAs (fig.4.11(c)). It is interesting to note that As_{Ga} -related defects in LT-GaAs (200°C) on substrate studied earlier showed T_1 times of < 100 ms [Krambrock 1992]. It seems that the lattice mismatch between substrate and layer induces additional strains which reduce the T_1 times similarly to observations in plastically deformed GaAs.

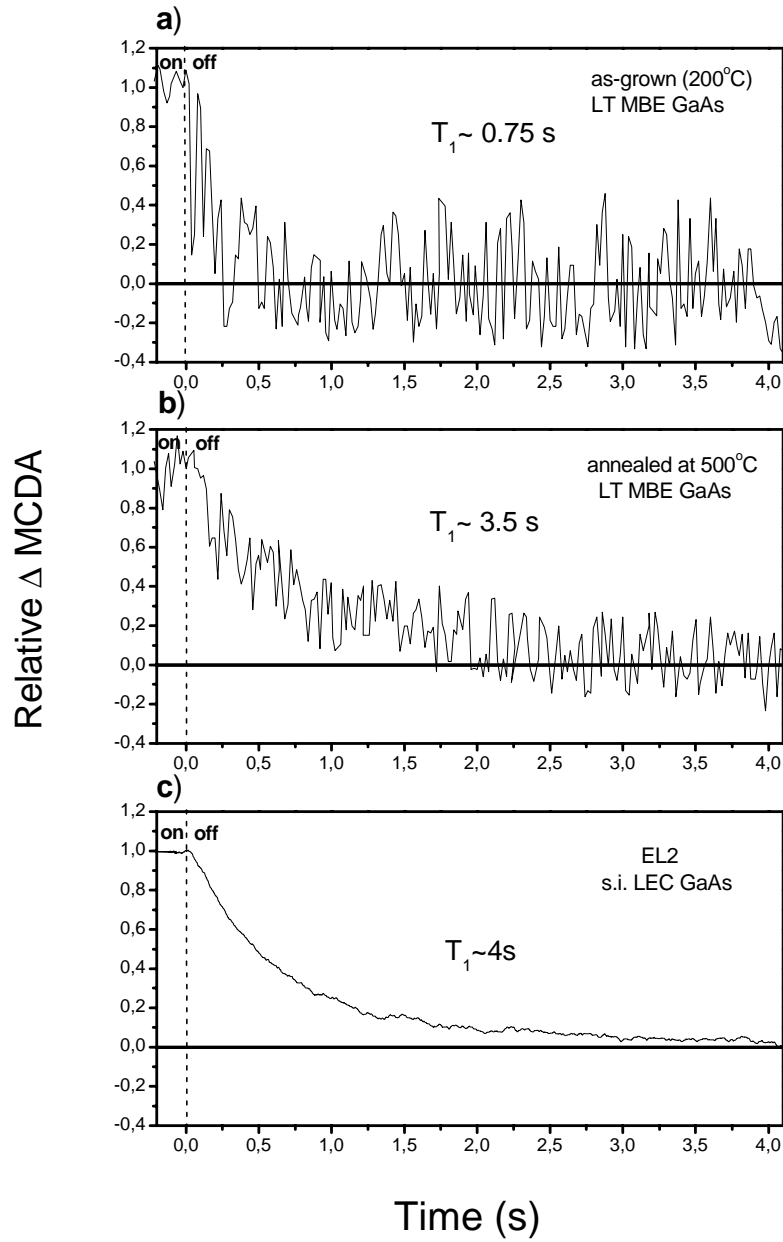


Fig. 4.11 Spin-lattice relaxation time (T_1) measured with MCDA technique for (a) as-grown (200°C) LT-GaAs, (b) LT-GaAs annealed at 500°C, and (c) the EL2⁺ defect in semi-insulating LEC GaAs. Temperature of measurements 1.5K. Magnetic field B_0 was 720mT and 680mT for LT-GaAs and for LEC GaAs, respectively (K-band).

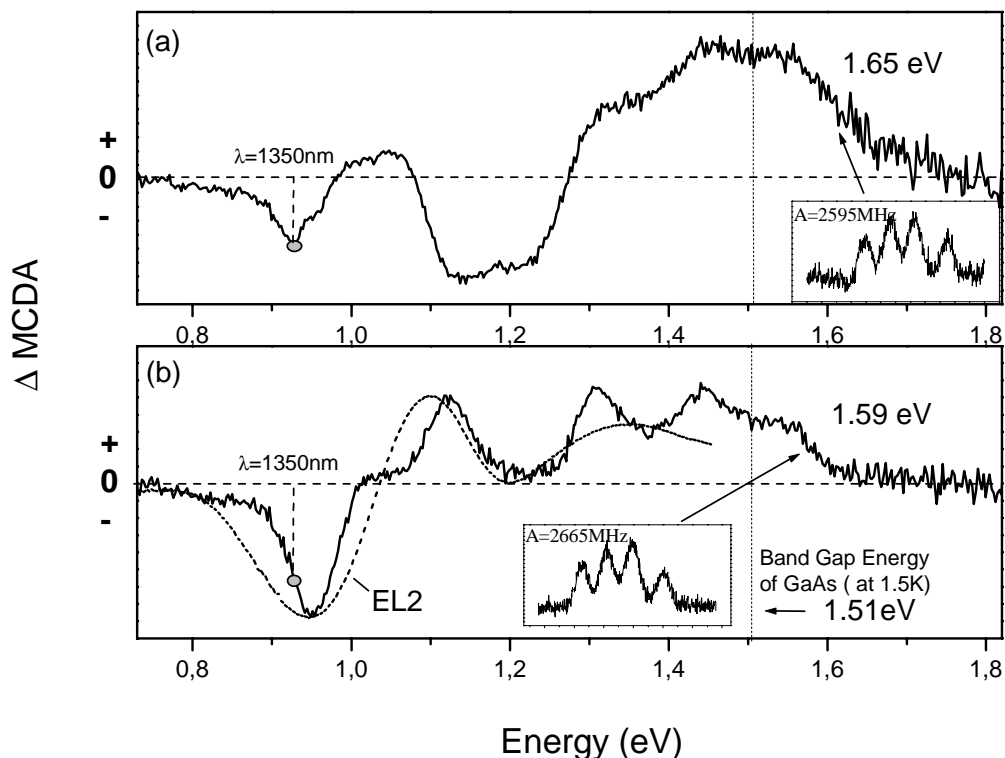


Fig. 4.12 Above band gap transitions of the native defects in LT-GaAs
 (a) tagged MCDA spectrum of as-grown(200°C) LT-GaAs
 (b) tagged MCDA spectrum of annealed at 500°C LT-GaAs. (Dashed line shows a typical tagged MCDA spectrum of the EL2 defect in SI GaAs).

Of particular interest are also the MCDA transitions at photon energies above the band gap of GaAs (fig.4.12(a),(b)). The preparation of the LT-GaAs films with the lift-off technique enabled us to perform MCDA and MCDA-EPR measurements without the influence of the GaAs substrate and very importantly, to measure above the band gap. For example, in as-grown LT-GaAs, a MCDA-EPR signal was detected using the photon energy of 1.65eV (730nm). For the isolated As_{Ga} defect the MCDA spectrum, which shows a single derivative-like shape, has been interpreted as belonging to a transition from the A_1 ground state to a localized excited T_2 state in the conduction band [Krambrock1992]. For the EL2 defect and also for the EL2-like defects in LT-GaAs more

transitions are observed, which are probably explained by a symmetry reduction which splits the excited state T_2 confirming previous MCDA-EPR/ENDOR results that EL2 is not the isolated As_{Ga} defect [Spaeth 1993].

4.5 Bleaching efficiency

For comparison between the EL2 defect in bulk GaAs and the As_{Ga} -related defects in annealed LT-GaAs the metastable properties have been studied under light illumination at low temperatures. It has been argued that the As_{Ga} -related defects in LT material are modified EL2 defects. This model was presented by Kaminska et al. ([Kaminska and Weber 1992]). They suggested that all defects in LT-GaAs (as-grown and annealed) are EL2-like and the difference is solely due to the lattice strain caused by the excess Arsenic.

There are some hints supporting the model of the As-antisite-like defect in LT-GaAs being identical to a strain modified EL2 defect:

- the EL2 can not be bleached under the condition when the high hydrostatic pressure is applied;
- the bleaching efficiency of the EL2 defect generated by plastic deformation is reduced;
- the lack of a zero-phonon line could be caused by a broadening of the transition energy due to local strain;
- MCDA measurements exhibit broadened lines. This effect could also be due to the local strain.

Chadi and Chang, Dabrowski and Sheffler ([Chadi and Chang 1988], [Dabrowski and Scheffler 1988]) explain the metastability of the EL2 as a slipping of an antisite Arsenic atom through the ring of the three adjacent Arsenic atoms on the regular places (through one of the walls of the surrounding tetraeder – see fig.4.13). This movement is related to the configuration coordinate shown in the figure. In its new equilibrium position the As is

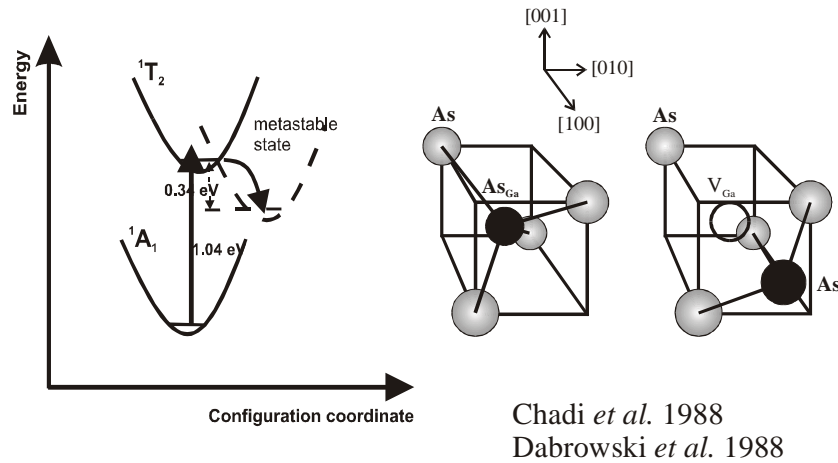


Fig. 4.13 Configuration coordinate diagram and mechanism of transition from the fundamental to the metastable state of the As_{Ga} defect according to ref. [Chadi and Chang 1988; Dabrowski and Scheffler 1988].

on the other side of the plane in a threefold bonding configuration. The driving force behind that movement is the Jahn-Teller-effect. In this model, following Kaminska et al. the spectral shift of the bleaching characteristics, which was reported to be approximately 0.2eV to higher energies ([Kowalski 1993]), can be explained by the local strain next to the antisite defect, therefore the Arsenic atom can be prevented moving towards the Arsenic ring and thus, more energy is necessary to rise the defect into the metastable state. The additional strain – caused by the methastable antisite defects – could be a reason for the reduced efficiency.

Inspecting the bleaching behavior of the native defects in as-grown and annealed LT GaAs we have observed rather complicated bleaching dynamics which depend strongly on annealing temperature. Our investigation confirms that the bleaching efficiency for the As_{Ga} -related defects in LT GaAs is shifted to higher photon energies. The shift in photon

energy depends on the annealing temperature and seems to be maximal for as-grown samples having the lowest bleaching efficiency. When exposing the samples to light which was usually used to bleach the EL2 defect ($h\nu < 1.2\text{eV}$) the opposite effect, namely enhancement of the MCDA-EPR spectra, was observed (see fig.4.14). This can be related to recharging from the diamagnetic (As_{Ga}^0) to the paramagnetic (As_{Ga}^+) charge states. The maximal enhancement was detected for as-grown LT-GaAs.

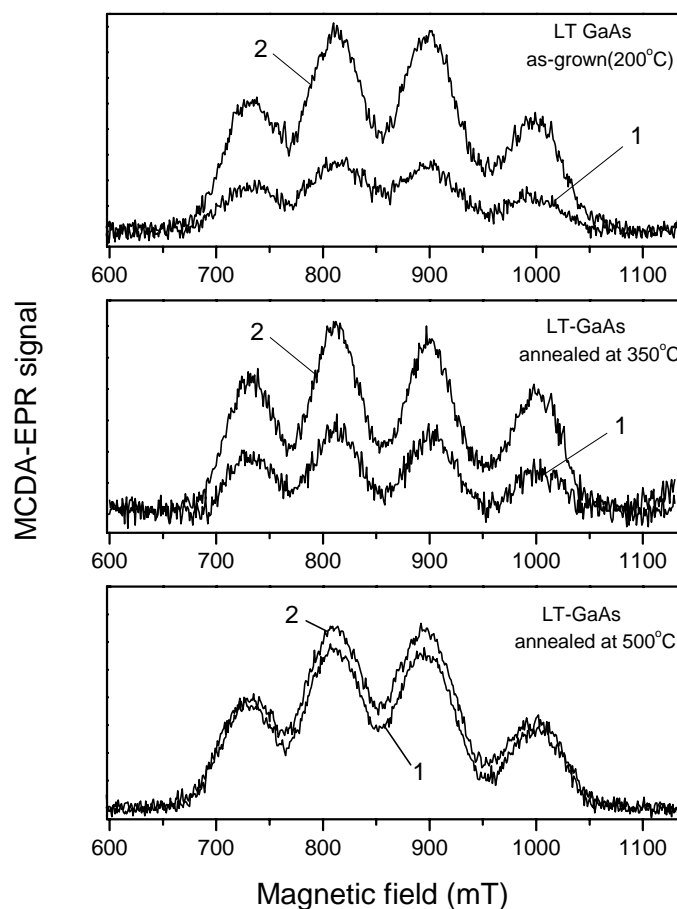


Fig. 4.14 EPR-MCDA spectra of as-grown and annealed LT-GaAs measured before (spectra (1)) and after 1h of illumination (spectra (2)) with photon energies below of 1.2eV. Spectra were measured with 0.92eV photon energy at μW -frequency 24.8GHz. Temperature of measurements 1.5K. μW -power 5mW.

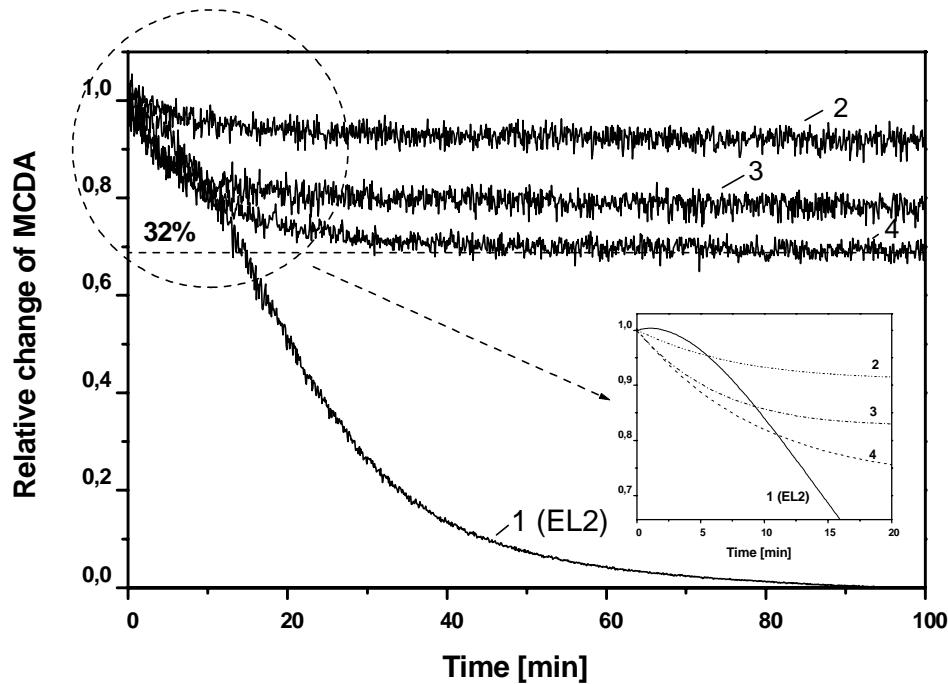


Fig. 4.15 Time transients of metastable transitions reflected in an intensity change of 0.92eV MCDA band when exposing the samples to white light measured in: (1) semi-insulating GaAs (the EL2 defect); (2) as-grown(200°C) LT-GaAs; (3) annealed at 350°C LT-GaAs; (4) annealed at 500°C LT-GaAs. Measurements were performed at 4.2K. Magnetic field B_0 was set at 3000mT. The total MCDA consists of a diamagnetic and a paramagnetic part.

While exposing the material to white light during 4h only ~32% of the total (diamagnetic and paramagnetic) MCDA of the defects in samples annealed at 500°C could be bleached (see fig.4.15). For as-grown material this value is even less (near 10%). This result indicates that in contrast with bulk semi-insulating GaAs crystal where the EL2 can be totally bleached a large part of the As_{Ga} -related defects in LT-GaAs are unquenchable. Obviously we deal with As_{Ga} -related defects in different local environments and structures. It is important to note the different behaviour of the transient MCDA time dependency of the EL2 defect in bulk GaAs and native defects in LT-GaAs, which must be due to different mechanisms involved in the quenching process in LT-GaAs and bulk SI GaAs.

4.6 Conclusions

Highly nonstoichiometric GaAs grown by MBE at low (180-230°C) substrate temperature (LT-GaAs) was investigated with the MCDA and MCDA-EPR technique. The MCDA-EPR spectra show mainly the four-line hyperfine spectra due to As_{Ga} -related defects (hf interaction with central ^{75}As nucleus, $I=3/2$). The spectra are isotropic with the rather large width of the EPR lines (40-60mT). A small difference in MCDA-EPR parameters for as-grown and annealed material was found. Further investigation with the “tagged” MCDA method revealed the different As_{Ga} -related defects in as-grown LT-GaAs and LT-GaAs annealed above 400°C. 350-400°C seems to be the critical annealing temperature.

In samples annealed near 500°C EL2-like defects were observed, whereas for annealing at 600°C and above the As_{Ga} -related MCDA-EPR spectra disappeared. Another MCDA-EPR spectrum is superimposed on the As_{Ga} -related spectra in as grown and annealed LT-GaAs. It was attributed to V_{Ga} -related defects, consistent with positron annihilation experiments. Furthermore, the EPR spectrum of a hitherto unknown defect was observed in samples annealed at 450°C and above. The large widths of the As_{Ga} -related hyperfine split EPR lines does not allow to identify the new defect reliably.

The lift-off sample preparation technique allowed the observation of the MCDA bands of the As_{Ga} -related defects with photon energies exceeding the band gap energy of GaAs. These transitions were attributed to localized excited states in the conduction band, which are indicative of a low symmetry of the defects where the T_2 excited state of the As_{Ga} is split. The EL2-like defects observed in LT-GaAs annealed at 500°C show nearly the same tagged MCDA spectra as those of EL2 defects in SI bulk GaAs and a maximum bleaching efficiency. Therefore, their structure should be similar. The large MCDA-EPR line widths of these defects are explained by local disorder and strain in the samples.

The bleaching efficiency of the As_{Ga} -related defects in LT-GaAs is reduced and shifted to higher photon energies in comparison with the EL2 defect in semi-insulating LEC GaAs. While exposing the material with light energies normally used for quenching of the EL2 defect (below 1.2eV) an enhancement of the MCDA-EPR was observed. The largest effect appears in as-grown material.

Summary

With the Magnetic Circular Dichroism of the optical Absorption (MCDA) and MCDA-detected Electron Paramagnetic Resonance (MCDA-EPR) and Electron Nuclear Double Resonance (MCDA-ENDOR) at K- and W- microwave frequency bands the EL2 defect in semi-insulating LEC GaAs and native defects in low temperature MBE-grown GaAs (LT-GaAs) have been investigated.

The results of former K-band MCDA-EPR/ENDOR measurements of the EL2 defect were difficult to interpret because of the higher order effects observed at low magnetic fields. Effects such as a pseudo-dipolar nuclear couplings and a high probability of forbidden transitions complicated the previously measured ENDOR spectra. Therefore they could not be analyzed satisfactorily. The high field/high frequency EPR/ENDOR is the only way to eliminate the undesirable influence of those second order effects. So far the structure of the EL2 defect has remained under debate. Most discussed were an isolated As_{Ga} antisite model with T_d symmetry and an $\text{As}_{\text{Ga}}\text{-As}_i$ (As-interstitial) pair model.

For high field MCDA-EPR and ENDOR measurements the development of light accessible high frequency microwave cavities was necessary. Two types of cavities (Fabry-Perot and cylindrical) were constructed which operate at W-band (95GHz) and pumped liquid He temperatures ($\sim 1.5\text{K}$). The design of the Fabry-Perot cavity (TEM_{00q}) for W-band was particularly successful for MCDA-ENDOR. The design of a cylindrical TE_{011} W-band microwave cavity was only successful for high field MCDA-EPR.

A high field (W-band) MCDA-EPR/ENDOR investigation of the EL2 defect was performed. It was possible at high fields ($\sim 3.0\text{-}3.6\text{ T}$) to eliminate the undesirable pseudo-dipolar nuclear couplings. Only ENDOR lines due to $m_S = -1/2$ state were observed. Forbidden ENDOR transitions ($\Delta m_S = 0; \Delta m_I > \pm 1$) still arise in W-band spectra with an unexpected large intensity, but they did not complicate the analysis of the spectra. Also in the high field MCDA-EPR measurements the forbidden transitions ($\Delta m_S = \pm 1; \Delta m_I > 0$) are

strongly reduced, which yielded a first order ^{75}As hyperfine pattern and lower EPR line widths compared to K-band.

With W-band MCDA-ENDOR two interacting ^{75}As shells were detected: the nearest neighbour shell and an ^{75}As shell which corresponds probably to a 5th neighbour shell. The angular dependencies of the first ^{75}As neighbour shell show within the range of experimental error almost T_d symmetry. The experimental error lies approximately in an unresolved ENDOR line width for $B_0 \parallel [001]$ of 2.2MHz, in which a small non-equivalence of the nearest neighbour nuclei can be still hidden. The non-equivalence can be at most about 1.5% of the superhyperfine constants. The higher (5th) neighbour shell detected with W-band ENDOR is split into two subshells indicating a pair defect inspite of the high symmetry of the nearest neighbours. The higher shell ENDOR spectra could not be simulated assuming a high defect symmetry. That reflects lower than T_d symmetry of the EL2 defect. The cause of the symmetry lowering can not contribute significantly to the shf interactions, because otherwise it would have been detected with the ENDOR and in the EPR line width. A diamagnetic Ga-vacancy (V_{Ga}) is a probable candidate of such a disturbance. Therefore, an $\text{As}_{\text{Ga}}^+ - V_{\text{Ga}}^{3-}$ model can be suggested as a alternative model of the EL2 defect in agreement with recent calculations by Overhof [Overhof 2002]. The $\text{As}_{\text{Ga}} - \text{As}_i$ model can be excluded since it would lead to a too large EPR line width compared with the W-band measurements.

The experiments showed that even a very small tilt of the crystal leads to additional splittings which could be wrongly interpreted. An additional and independent control of the crystal orientation proved necessary. Such a correction was achieved with a specially designed sample-holder allowing a sample rotation in two perpendicular planes at least within a few degrees.

The magneto-optical investigations of native mainly As_{Ga} -related defects similar to the EL2 defect in as-grown (200°C) and annealed LT-GaAs show that the defect properties are greatly influenced by the annealing temperature. The samples were prepared with a lift-off technique and only about 1 μm thick allowing light passing through at photon energies beyond the gap energy of 1.5eV. By measuring the tagged MCDA spectra of the defects in as-grown and annealed material the different optical properties of the defects

were observed. The MCDA spectra “tagged” by EPR serve as fingerprints of the defects. Therefore, it was possible to decide that the defects in as-grown and annealed material are different, even if their EPR parameters differ only very little or not within the experimental error. The experimental error of the determination of the EPR parameters is relatively large because of large line widths of the As_{Ga} -related spectra and a low signal-to-noise ratio. The tagged MCDA spectra of the defects in LT-GaAs annealed at 500°C exhibit a shape characteristic for the EL2 defect. Therefore the structure of the As_{Ga} -related defects in such samples and the prominent EL2 should be the same or at least similar. In addition to the As_{Ga} -related spectra, a superimposed MCDA-EPR spectrum was observed which was attributed to the V_{Ga} -related defect in as-grown and annealed LT-GaAs. In samples annealed above 400°C a third spectrum arises if MCDA-EPR spectra are measured at photon energies near 1.12eV. Its reliable identification was not possible.

The bleaching efficiency of the defects in LT-GaAs is reduced. It is shifted to higher photon energies compared with the EL2 defect. When exposing the samples to white light the maximum of bleaching was reached in samples annealed at 500°C (32%). The lowest bleaching efficiency was observed for as-grown LT-GaAs samples. While exposing the LT-GaAs with light of spectral energy normally used for bleaching of the EL2 ($h\nu < 1.2\text{eV}$) an enhancement of the MCDA-EPR spectra was observed. This effect is related to a recharging from the diamagnetic to the paramagnetic charge state of the defects.

References

- [Abragam and Bleaney 1986] A. Abragam and B. Bleaney “Electron Paramagnetic Resonance of Transition Ions”, Dover Publications, Inc., New York (1986)
- [A. van Duijn-Arnold 1999] A.. van Duijn-Arnold, J.Mol, R.Verberk, J.Schmidt, E.N.Mochov, and P.G.Baranov, *Phys.Rev.B* **60**, (1999)
- [Baldacchini and Mollenauer 1972] G. Baldacchini and L. F. Mollenauer, *Appl. Optics* **11**(11), 2676 (1972)
- [Baj and Dreszer 1989] M.Baj and P.Dreszer, *Phys.Rev.B* **39**, p.10470 (1989)
- [Baraff and Schlüter 1985] G. A. Baraff and M. Schlüter, *Phys. Rev. Lett.* **55**, 1327 and 2340 (1985)
- [Baraff 1992] G. A. Baraff, *Acta Physica Polonica A* **82**, 599(1992)
- [Bardeleben 1989] H.J. von Bardeleben, *Phys.Rev.B* **40**, p.12546(1989)
- [Bardeleben and Bourgoïn 1985] H. J. von Bardeleben and J. C. Bourgoïn, *J. Appl. Phys.* **58**, 1041 (1985)
- [Bardeleben 1985] H. J. von Bardeleben, D. Stiévenard and J. C. Bourgoïn, *Appl. Phys. Lett.* **47**, 970 (1985)
- [Bardeleben 1986] H. J. von Bardeleben, J. C. Bourgoïn and A. Miret, *Phys.Rev. B* **34**, 1360 (1986)
- [Bardeleben and Bourgoïn 1986] H. J. von Bardeleben and J. C. Bourgoïn, *Phys. Rev. B* **33**, 2890 (1986)
- [Bardeleben 1987a] H. J. von Bardeleben, A. Miret, and J. C. Bourgoïn, *Phys. C Solid State Phys.* **20**, 1353 (1987)
- [Bardeleben 1987b] H. J. von Bardeleben, N. T. Bagraev and J. C. Bourgoïn, *Appl. Phys. Lett.* **51**, 1451 (1987)
- [Bardeleben and Pajot 1988] H. J. von Bardeleben and B. Pajot, *Rev. Phys. Appl.* **23**, 727 (1988)
- [Bardeleben 1994] H. J. von Bardeleben, C. Delerue and D. Stiévenard, *Mat. Science Forum* **143-147**, 223 (1994)
- [Belford 1973] G. G. Belford, R. L. Belford and J. F. Burkhalter, *J. Magn. Reson.* **11**, 251 (1973)

- [Bourgoin 1988] J. C. Bourgoin, H. J. von Bardeleben and D. Stiévenard, *J.Appl. Phys.* **64**, R65 (1988)
- [Boyd and Gordon 1961] Boyd G.D. and Gordon G.P., *Bell.Syst.Tech.J.* March, 489 (1961)
- [Boyd and Kogelnik 1962] Boyd G.D. and Kogelnik H., *Bell.Syst.Tech.J.* July, 1347 (1962)
- [Breit and Rabi 1931] G. Breit and I. I. Rabi, *Phys. Rev.* **38**, 2082 (1931)
- [Burghaus 1985] O.Burghaus, M. Rohrer, T.Götzinger, M.Plato, and K.Möbius, *Meas.Sci.Techn.* **3**, 765(1992)
- [Chadi and Chang 1988] D. J. Chadi and K. J. Chang, *Phys. Rev. Lett.* **60(21)**, 2187 (1988)
- [Corbel 1988] C. Corbel, M. Stucky, P. Hautojärvi, K. Saarinen and P. Moser, *Phys. Rev. B* **38**, 8192 (1988)
- [Corbel 1990] C. Corbel, F. Pierre, P. Hautojärvi, K. Saarinen and P. Moser, *Phys. Rev. B* **41**, 10632 (1990)
- [Corbel 1992] C. Corbel, F. Pierre, K. Saarinen, P. Hautojärvi and P. Moser *Phys. Rev. B* **45**, 3386 (1992)
- [Culbertson 1987] J. C. Culbertson, U. Strom and S. A. Wolf, *Phys. Rev. B* **36**, 2962 (1987)
- [Dankowski 1998] S.Dankowski, PhD thesis, Friedrich-Alexander-Universität Erlangen Nürnberg, Erlangen (1998)
- [Dabrowski and Scheffler 1988] J.Dabrowski and M.Scheffler, *Phys. Rev. Lett.* **60(21)**, 2183(1988)
- [Dabrowski and Scheffler 1989] J.Dabrowski and M.Scheffler, *Phys. Rev. B* **40**, 10391 (1989)
- [Delerue 1987] C. Delerue, M. Lannoo, D. Stiévenard, H. J. von Bardeleben and J. C. Bourgoin, *Phys. Rev. Lett.* **59**, 2875 (1987)
- [Delerue 1991] C. Delerue, *Phys. Rev. B* **44**, 10525 (1991)
- [Dischler and Kaufmann 1988] B.Dishler and U.Kaufmann, *Phys. Rev. Appl.* **23** (1988) 779
- [Elliot 1984] K. Elliot, R. T. Chen, S. G. Greenbaum and R. J. Wagner, *Appl. Phys. Lett.* **44**, 907 (1984)

- [Feuchtwang 1962] T. E. Feuchtwang, *Phys. Rev.* **126**, 1616 and 1628 (1962)
- [Fischer 1987] D. W. Fischer, *Appl. Phys. Lett.* **50**, 1751 (1987)
- [Fox and Li 1961] Fox A.G. and Tingye Li, *Bell Syst.Tech.J* March, 453 (1961)
- [Gebauer 1997] J.Gebauer, R.Krause-Rehberg, S.Eichler, M.Luysberg, H.Sohn, and E.R.Weber, *Appl. Phys. Lett.* **71**, 638 (1997)
- [Gebauer 2000] J.Gebauer, F.Börner, R.Krause-Rehberg, T.E.M.Staab, W.Bauer-Kugelmann, G.Kögel, W.Triftshäuser, P.Specht, R.C.Lutz, E.R.Weber, M.Luysberg, *J. Appl. Phys.* **87**, 8368 (2000)
- [Goswami 1981] N. K. Goswami, R. C. Newman and J. E. Whitehouse, *Solid State Commun.* **40**, 473 (1981)
- [Grinberg 1976] Grinberg O.Ya., Dubinskii A.A. Shuvalov V.F., Oransky L.G., Kurochkin V.I., Lebedev Ya.S., Dokl. Akad. Nauk USSR **230**, 884(1976)
- [Görger 1988] A.Görger, B.K.Meyer, J.-M.Spaeth, A.M.Hennel, *Semicond.Sci.Technol.* **3**, 832 (1988)
- [Hausmann 1996] H. Hausmann, A. Pillukat and P. Ehrhart, *Phys. Rev. B* **54**, 8527 (1996)
- [Haindl 1985] Haindl E., Möbius K., Oloff B., *Z.Naturforsch. A* **40**, 169 (1985)
- [Hesse 1994] M. Hesse, F. K. Koschnick, K. Krambrock and J.-M. Spaeth, *Solid State Commun.* **92**, 207 (1994)
- [Hofmann 1990] D. M. Hofmann, B. K. Meyer, J.-M. Spaeth, M. Wattenbach, J. Krüger, C. Kieselowski-Kemmerich and H. Alexander, *J. Appl. Phys.* **68**, 3381 (1990)
- [Hofmann 1984] D.M.Hofmann, B.K.Meyer, F.Lohse, and J.-M.Spaeth, *Phys.Rev.Lett.* **53**, 1187(1984)
- [Jasperson and Schnatterly 1969] S. N. Jasperson and S. E. Schnatterly, *Rev. Sci. Instrum.* **40**, 761 (1969)
- [Jia 1992] Y. Q. Jia, H. J. von Bardeleben, D. Stiévenard and C. Delerue, *Phys. Rev. B* **45**, 1645 (1992)
- [Jia and von Bardeleben 1993] Y. Q. Jia and H. J. von Bardeleben, *Phys. Lett. A* **178**, 205 (1993)

- [Kaminska 1985] M. Kaminska, M. Skowronski and W. Kuszko, *Phys. Rev. Lett.* **55**, 2204 (1985)
- [Kaminska and Weber 1993] M. Kaminska and E. R. Weber in *Semiconductors and Semimetals* **38** "Imperfections in III/V Materials", ed. E. R. Weber, Academic Press, San Diego (1993)
- [Kaminska and Weber 1992] M.Kaminska, E.R.Weber, *Materials Science Forum* **83-87**, 1033 (1992)
- [Kalabukhova 1992] E.N.Kalabukhova, S.N.Lukin, B.D.Shanina in "Radiospectroscopy of Solid State", Naukova Dumka, Kiev (1992)
- [Kaufmann 1985] U. Kaufmann, *Phys. Rev. Lett.* **54**, 1332 (1985)
- [Kennedy 1981] T. A. Kennedy, B. J. Faraday and N. D. Wilsey, *Bull. Am.Phys. Soc.* **26**, 255 (1981)
- [Kennedy and Spencer 1986] T. A. Kennedy and M. G. Spencer, *Phys. Rev. Lett.* **57**, 2690 (1986)
- [Kennedy 1988] T. A. Kennedy, R. Magno and M. G. Spencer, *Phys. Rev. B* **37**, 6325 (1988)
- [Koschnick 1998] F. K. Koschnick, K.-H. Wietzke and J.-M. Spaeth, *Phys. Rev. B* **58**, 7707 (1998)
- [Koschnick and Spaeth 1999] F.K.Koschnick and J.-M.Spaeth, *Phys.Stat.Sol.(b)* **216**, 817 (1999)
- [Kogelnik and Li 1966] H.Kogelnik and T.Li, *Proceedings of the IEEE*, vol.54, no.10, 1312(1966)
- [Krambrock 1989] K. Krambrock, B. K. Meyer and J.-M. Spaeth, *Phys. Rev. B* **39**, 1973 (1989)
- [Krambrock 1992] K. Krambrock, PhD thesis, Universität-GH Paderborn (1992)
- [Krambrock 1992a] K. Krambrock, J.-M. Spaeth, C. Delerue, G. Allan and M. Lannoo, *Phys. Rev. B* **45**, 1481 (1992)
- [Krambrock 1992b] K. Krambrock, M. Linde, J.-M. Spaeth, D. C. Look, D. Bliss and W. Walukiewicz, *Semicond. Sci. Technol.* **7**, 1037 (1992)
- [Krambrock and Spaeth 1992] K. Krambrock and J.-M. Spaeth, *Phys. Rev. B* **45**, 1481(1985)

- [Krambrock and Spaeth 1993] K. Krambrock and J.-M. Spaeth, *Phys. Rev. B* **47**, 3187 (1993)
- [Krambrock 1994] K. Krambrock, F. K. Koschnick, M. Hesse and J.-M. Spaeth, "Semi-Insulating III-V Materials" **229**, ed. M. Godlewski, World Scientific Publishing (1994)
- [Krambrock and Spaeth 1995] K. Krambrock and J.-M. Spaeth, *Solid State Commun.* **93**, 285 (1995)
- [Krambrock 1997] K. Krambrock, M. V. B. Pinheiro, K.-H. Wietzke and J.-M. Spaeth, Proceedings of the International Conference on Defects in Semiconductors ICDS-19, Aveiro, Portugal (1997)
- [Krause 1990] R. Krause, K. Saarinen, P. Hautojärvi, A. Polity, G. Gärtner and C. Corbel, *Phys. Rev. Lett.* **65**, 3329 (1990)
- [Kurpiewski 1991] A. Kurpiewski, M. Palczewska, M. Kaminska, E. R. Weber, *Acta Phys. Pol.* (1991)
- [Landman 1997] J. I. Landman, C. G. Morgan, J. T. Schick, P. Papoulias, and A. Kumar, *Phys. Rev. B* **55**, 15581 (1997).
- [Lannoo 1991] M. Lannoo, *Semicond. Sci. Technol.* **6**, B16 (1991)
- [Lannoo and Bourgoin 1981] M. Lannoo and J. Bourgoin, "Point Defects in Semiconductors I", Springer-Verlag (1981)
- [Lüty and Mort 1964] F. Lüty and J. Mort, *Phys. Rev. Lett* **12**, 45 (1964)
- [Lukin 1974] Lukin S.N., Nemchenko E.D., Oranskii L.G., *Pribory i Technika Eksperimenta*, **17**(4), 116(1974); translated in *Instruments and Experimental Techniques*, **17**(4), 1073(1974)
- [Martin 1977] G.M. Martin, A. Mitonneau, A. Mircea, *Electron. Lett. (UK)* **13**, 191 (1977)
- [Martin 1981] G.M. Martin, *Appl. Phys. Lett. (USA)* **39**, 747(1981)
- [Manasreh and Fischer 1989] M. O. Manasreh and D. W. Fischer, *Phys. Stat. Sol. (b)* **154**, 11 (1989)
- [Manasreh 1990] M.O. Manasreh, D.C. Look, K.R. Evans, and C.E. Stutz, *Phys. Rev. B* **41**, 10272 (1990)
- [Meyer 1984] B. K. Meyer, J.-M. Spaeth, and M. Scheffler, *Phys. Rev. Lett.* **52**, 851(1984)

- [Meyer 1987] B. K. Meyer, D. M. Hofmann, J. R. Niklas and J.-M. Spaeth, *Phys. Rev. B* **36**, 1332 (1987)
- [Meyer 1988] B. K. Meyer, *Revue Phys.Appl.* **23**, 809 (1988)
- [Mollenauer and Pan 1972] L. F. Mollenauer and S. Pan, *Phys. Rev. B* **6**, No. 3, 772 (1972)
- [Mott 1932] N. F. Mott, Proceedings of the Royal Society London, Ser. A **135**, 429 (1932)
- [Mutorani 1978] T.Mutorani, T.Shimano, and S.Mitsui, *Journal of Crystal Growth* **45**, 302 (1978)
- [Nissen 1991] M. K. Nissen, A. Villemaire and M. L. W. Thewalt, *Phys.Rev. Lett.* **67**, 112 (1991)
- [Overhof 2002] Private communications (2002)
- [Pons and Bourgoïn 1985] D. Pons and J. Bourgoïn *J. Phys. C* **18**, 3839 (1985)
- [Poole 1983] C. P. Poole, Jr. "Electron Spin Resonance. A Comprehensive Treatise on Experimental Techniques", Wiley, New York (1983)
- [Poluektov 1988] Poluektov O.G., Grinberg O.Ya., Dubinskii A.A., Luk'yanenko L.V., Sidorov O.Yu., Lebedev Ya.S., *Russ. J.Phys.Chem.* **62**, 1067 (1988)
- [Saarinen 1995] K. Saarinen, A. P. Seitsonen, P. Hautojärvi and C. Corbel, *Phys. Rev. B* **52**, 10932 (1995)
- [Seidel 1966] H. Seidel, Habilitation thesis, Universität Stuttgart (1966)
- [Skowronski 1986] M. Skowronski, J. Lagowski, H. C. Gatos, *J. Appl. Phys.* **59**, 2451 (1986)
- [Skowronski 1987] M.Skowronski, *Mat.Sc.For.*, **104**, p.405 (1987)
- [Slichter 1980] C. P. Slichter "Principles of Magnetic Resonance", Springer-Verlag, Berlin, Heidelberg, New York (1980)
- [Spaeth 1990] J.-M. Spaeth, K. Krambrock and D. M. Hofmann, in "The Physics of Semiconductors" **1**, 441, ed. E. M. Anastassakis and J. D Joannopoulos, World Scientific, Singapore (1990)

- [Spaeth 1992] J.-M. Spaeth, J. R. Niklas and R. H. Bartram "Multiple Magnetic Resonance Spectroscopy for Structural Analysis of Point Defects in Solids", Springer, Heidelberg (1992)
- [Spaeth and Krambrock 1994] J.-M. Spaeth and K. Krambrock, in *Festkörperprobleme/Advances in Solid State Physics* **33**, p. 111, ed.R. Helbig, Vieweg, Braunschweig (1994)
- [Stevens 1952] K. W. H. Stevens, *Proc. Phys. Soc.* **65**, 209 (1952)
- [Stiévenard and Bourgoïn 1986] D. Stiévenard and J. C. Bourgoïn, *J. Appl. Phys.* **59**, 808 (1986)
- [Stiévenard 1990] D. Stiévenard, X. Boddaert, J. C. Bourgoïn and H. J. von Bardeleben, *Phys. Rev. B* **41**, 5271 (1990)
- [Schmalbein 1999] D.Schmalbein, G.G.Maresch, A.Kamrowski, and P.Höfer, *Appl.Magn.Reson.* **16**, 185(1999)
- [Smith 1988] F.W.Smith, A.R.Calawa, S.L.Chen, M.J.Manfra, and L.J.Mahoney, *IEEE Electronic Device Letters* **9**, 77 (1988)
- [Sun 1992] H.-J.Sun, G.D.Watkins, F.C.Rong, L.Fotiadis, and E.H.Poindexter, *Appl. Phys. Lett.* **60**, 718 (1992)
- [Tautz 2000] S.Tautz, PhD thesis, Friedrich-Alexander-Universität Erlangen Nürnberg, Erlangen (2000)
- [Tkach 1999] I.I.Tkach, F.K.Koschnick, J.-M.Spaeth, S.Tautz, and P.Kiesel, in *2nd Symposium On Non-Stoichiometric III-V Compounds*, vol.**10** of *Physik Mikrostrukturierter Halbleiter*, 53 (1999)
- [Tkach 2002a] I. Tkach, K. Krambrock, C. Steen, P. Kiesel and J.-M. Spaeth, *Physica B Physics of Condensed Matter*, **308-310**, 749 (2002)
- [Tkach 2002b] I. Tkach, K. Krambrock and J.-M. Spaeth, *Physica B Physics of Condensed Matter*, **308-310**, 753(2002)
- [Trautman and Baranowski 1992] P. Trautman and J. M. Baranowski, *Phys. Rev. Lett.* **69**, 664(1992)
- [Trombetta 1991] J.M.Trombetta, T.A.Kennedy, W.Tseng, and G.Gammon, *Phys.Rev.B* **43**, 2458 (1991)

- [Wimbaur 1997] T.Wimbaur, M.S.Brandt, M.W.Bauerl, M.Stutzmann, D.M.Hofmann, Y.Mochisuki, and M.Mizuta, *Mat.Sci.Forum* **258-263**, 1309 (1997)
- [Wagner 1980] R. J. Wagner, J. J. Krebs, G. H. Strauss and A. M. White, *Solid. State Commun.* **36**, 15 (1980)
- [Watkins and Corbett 1961] G. D. Watkins and J. W. Corbett, *Phys. Rev.* **121**, 1001 (1961)
- [Weber and Schneider 1982] E.R.Weber and J.Schneider, *Physica* **116B**, 398(1983)
- [Weber 1998] S.Greulich-Weber, F.Feege, K.N.Kalabukhova, S.N.Lukin, J.-M.Spaeth and F.J.Adrian, *Semicond.Sci.Technol.* **13**, 59(1998)
- [Wietzke 1997] K.-H. Wietzke, K. Krambrock and F. K. Koschnick, *Appl. Phys. Lett.* **71**, 2133 (1997)
- [Wietzke 1997] K.-H. Wietzke, PhD thesis, Universität-GH Paderborn (1997)
- [Wirbeleit and Niklas 1997a] F. Wirbeleit and J. R. Niklas, Proceedings of the International Conference on Defects in Semiconductors (ICDS-19), Aveiro, Portugal, (1997)
- [Wirbeleit and Niklas 1997] F. Wirbeleit and J. R. Niklas, *Materials Science Forum* **258-263**, 987(1997)
- [Wörner 1981] R.Wörner, U.Kaufman, and J.Schneider, *Appl.Phys.Lett.* **40**(2), 141(1982)
- [Yu 1992] K.M.Yu, M.Kaminska, and Z.Liliental-Weber, *J. Appl. Phys.* **72**, 2850 (1992)
- [Yablonowitch 1987] E.Yablonovitch, T.Gmitter, J.P.Harbison, R.Bhat, *Applied Physics Letters* **51**, 2222 (1987)
- [Zhang 1991] S.B.Zhang and J.E.Northrup, *Phys. Rev. Lett.* **67**, 2339 (1991)

DANKSAGUNG

Ich möchte meinen Dank folgenden Personen ausdrücken, mit deren Hilfe die vorliegende Arbeit gemacht wurde:

- Herrn Prof. Dr. J.-M. Spaeth für die freundliche Aufnahme in seine Arbeitsgruppe, für stete Unterstützung und Förderung, viele hilfreiche Hinweise und für guten Rat bei wichtigen Entscheidungen;
- Herrn Prof. H. Overhof für seine Berechnungen und Diskussionen;
- Herrn Dr. habil. F.-K. Koschnick für die Einführung in die magnetischen Resonanzmethoden, seine Hilfe bei experimentellen Problemen, Unterstützung und Motivation in ersten Phasen der Arbeit;
- Herrn Prof. Dr. K.Krambrock für Rat und Hilfe in vielen experimentellen und theoretischen Fragen, für die nützlichen Diskussionen und erfolgreiche Zusammenarbeit;
- Herrn Dr. habil. S. Schweizer für seine Hilfe bei der Analyse der Meßdaten aus ENDOR Untersuchungen;
- Frau Dr. E.N. Kalabukhova (Institut für Halbleiterphysik, Akademie der Wissenschaften der Ukraine, Kiew, Ukraine) für die Einführung in magnetische Resonanzspektroskopie und ihre Rat und Hilfe in theoretischen Fragen;
- Herrn Dr. S.N. Lukin (Institut für Halbleiterphysik, Akademie der Wissenschaften der Ukraine, Kiew, Ukraine) für die vielen hilfreichen Hinweise zur Entwicklung der neuen Techniken;
- Herrn Priv. Doz. Dr. S. Greulich-Weber für steten Rat und Hilfe bei der Lösung von vielen organisatorischen Fragen;
- Herrn F.Risse und den anderen Mitarbeitern von der mechanischen Werkstatt, deren Meisterschaft im Schaffen vom Resonator entscheidend war;
- Herrn Dr. F.Lohse und Herrn J.Pauli für die Bereitstellung mit Kältemitteln;

- Herrn Dr. Ch. Hoentzsch für das Rechnernetz;
- Herrn R. Winterberg für Hilfe im Kristallzuchtlabor;
- Herrn Dr. P. Kiesel, Herrn Dr. S. Tautz und Dipl. Phys. Ch. Steen (Universität Erlangen-Nürnberg) für die Vorbereitung der Proben;
- Herrn Dipl.Phys. M. Legodi (UAR) für die Bestrahlung der Proben;
- Allen meinen derzeitigen und ehemaligen Mitarbeitern, insbesondere Dr. Thomas Lingner, Dr. Uldis Rogulis, Dr. Bertram Langhanki, Dr. Karsten Michael, Cand. Phys. Franz Zollner, Dr. Isabel Grassa-Molina, Dipl. Phys. Jose Portoles, Dr. Stefan Assmann, Frau Anna Tacke, Herrn W. Hermisch für ein hervorragendes Arbeitsklima und für Rat und Hilfe bei der täglichen Arbeit;
- Deutsche Forschungsgemeinschaft (DFG) für die finanzielle Unterstützung.

Mein ganz besonderer Dank gilt meiner Frau Karolina und meinem Sohn Sergej für ihre Geduld, Verständnis, Unterstützung und für die günstige Atmosphäre in der Familie, in welcher diese Arbeit gemacht werden konnte.

